Dissertation

Development of a new analysis method in two-dimensional reciprocal space map and evaluation of surface atomic arrangement in three-dimensionally nano-fabricated materials using diffraction

Shohei Takemoto

September 18, 2018

Surface and Materials Science Laboratry

Graduate School of Materials Science

Nara Institute of Science and Technology

Contents

Abbreviation list

1D : One Dimensional

2D : Two Dimensional

3D : Three Dimensional

FEM : Finite Element Method

FET : Field-Effect Transistor

FWHM : Full Width at Half Maximum

GV : Gate Valve

LEED : Low Energy Electron Diffraction

ML : Mono Layer

RHEED : Reflection High Energy Electron Diffraction

RSM : Reciprocal Space Map

SPE : Solid Phase Epitaxy

STM : Scanning Tunneling Microscope

TEM : Transmission Electron Microscopy

UHV : Ultra-High Vacuum

W-H : Williamson-Hall

XPD : X-ray Photoelectron Diffraction

XRD : X-ray Diffraction

Chapter 1. Introduction

1.1 Historical background

The effects of diffraction of light were firstly observed and characterized by Francesco Maria Grimaldi. The results of Grimaldi's observations were published posthumously in 1665. Then James Gregory observed the diffraction patterns caused by a bird feather, which was effectively the first diffraction grating to be discovered. Here, I focused two types of diffraction which are well known to observe the diffraction pattern derived from the structure of sample. X-ray diffraction (XRD) and electron diffraction (ED), here ED indicates Reflection High Energy Electron Diffraction (RHEED), are caused by constructive interference of scattered waves, and the same fundamental laws (e.g., Bragg law, extinction rules) can be applied for the interpretation of the resulting diffraction patterns.

Reflection spots in reciprocal space obtained by diffraction measurements include crystalline information of strains and domain sizes in addition to phases, and have been analyzed with various methods. θ-2θ measurements in XRD yield these crystalline information from the reciprocal lattice points on the 00 rod, which passes through the origin in reciprocal space and is perpendicular to the crystalline planes. Peak-center 2θ angles, corresponding to linear combinations of reciprocal lattice vectors, lead to lattice constants which estimate averaged strain, and the broadening of a peak angle leads to a crystalline domain size expressed by a Laue function as known as Scherrer analysis [1–5]. When crystalline domains have an inhomogeneous strain distribution, the strain broadening in addition to a domain size is often evaluated by Williamson-Hall (W-H) analysis using multiple reflection spots [6–11]. Instead of these analyses which focus peak centers and peak broadenings, much more precise analyses

focusing peak shapes have been performed; that is, the fitting of the peak shapes with those from simple strain models. There are many reports about 1D fitting of estimating strain for quantum dots [12], nano wire [13, 14]. In 2D fitting, the analysis of reciprocal space map (RSM) have been performed to understand strains of films, wires dots grown on crystalline substrates [15, 16]. However, there is almost never paper to estimate the in-plane strain and domain size of inhomogeneous epitaxial film.

RHEED is useful method for determining the surface structure of the sample. Firstly, Wave nature was experimentally confirmed by Davisson and Germer in 1927 [17], and Thomson [18], Kikuchi [19], Rupp [20] in 1928 in the form of electron diffraction phenomena. Then In-situ characterization of epitaxial growth was observed by Ploog [21]. Ino reported experimantal results obtained in the studied of the Si(111)7×7, Si(111)$\sqrt{19} \times \sqrt{19}$ Ni and Si(111)5×1 Au structures in 1977 [22]. STM images are easy to directly understand the structure, but the interpretation of the images is not simple. So RHEED is one of the effective method of analyzing the surface structure even today. Recently, the development of a new type of RHEED observation with an energy filter to exclude inelastically scattered electrons [23] and Weissenberg RHEED which can observe three dimensinal RSM [24] was reported. Thus both method have been measured in different field by using their characteristics.

1.2 β-$FeSi_2$ (100) nano-carpet

The issue of global environments such as global warming, air pollution and exhaustion of resources becomes serious and draws big social interest. Among them, such environmental pollution and the issue of resources have been regarded as important in the field of the materials development. It was no exception in the field of semiconductor which enabled high function and technological advance of electronics equipments. Then, the development of alternative materials has been required instead of the compound semiconductor (GaAs, GaP, InP, and so on) which includes toxic substances or rare elements using as standard.

Iron silicide is expected as the alternative materials because it contains abundant chemical elements (Fe and Si) and is environmentally friendly. Though iron silicide has many types of phases, β-$FeSi_2$ is attracting our attention because of owing to band gap energy of $\sim$0.8 eV (infrared emission at $\sim$1.5 µm) [25, 26], β-$FeSi_2$ has a wide application in thermoelectric materials for high temperature, photodetector, solar cell and optoelectronic devices. Also β-$FeSi_2$ is a semiconductor with a high hole mobility [27, 28], so it could be used as a material in field effect transistors.

Figure 1.1 shows the phase diagram of Fe-Si alloy in bulk [29], however, it becomes very different in the situation of surface. Recently, H. Nakano, K. Hattori et al. made a schematic phase diagram about the surface of Fe-Si at 100$\sim$900 °C by using STM and LEED [30].

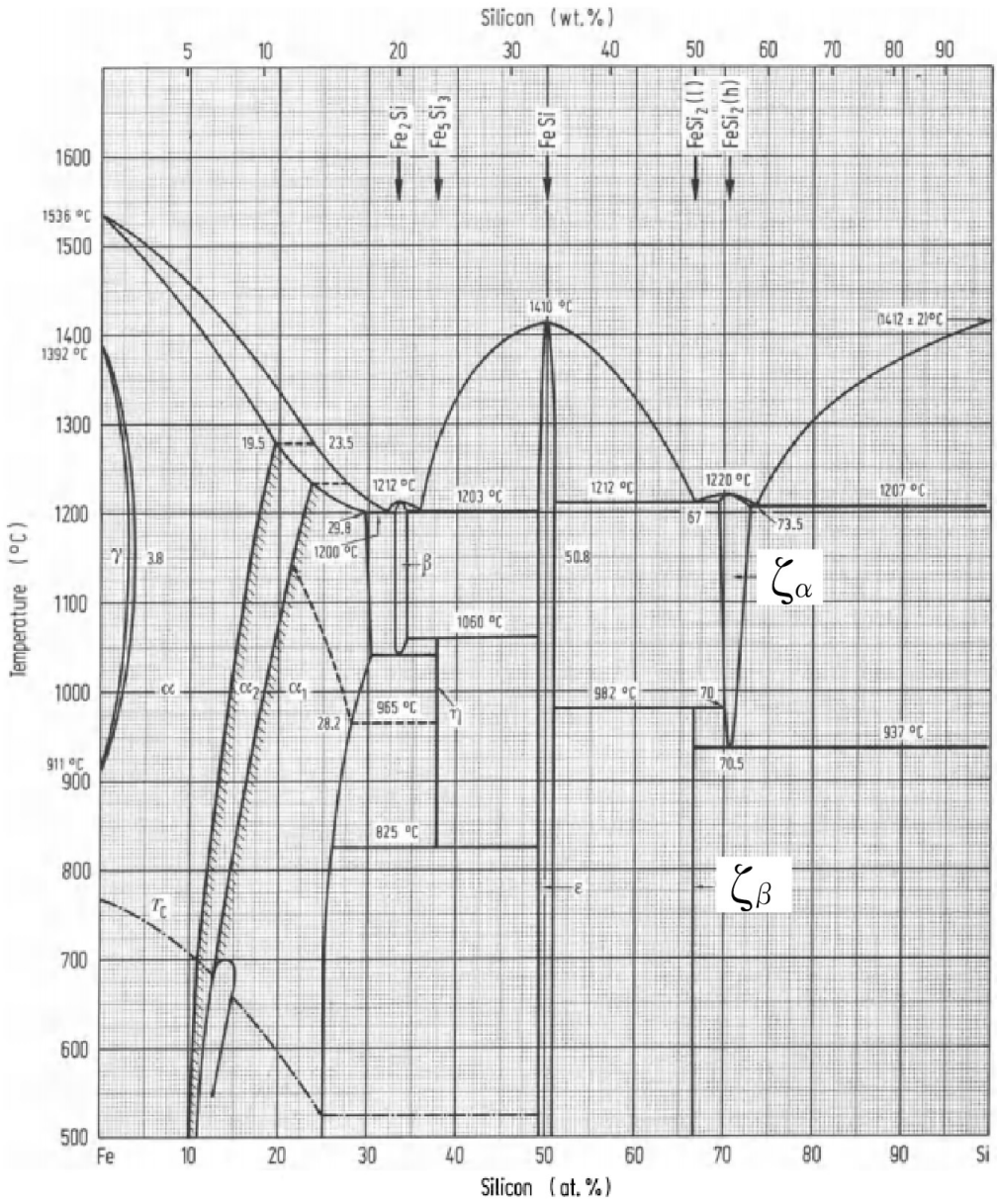

Fig. 1.1. Fe-Si binary phase diagram [29].

Someta [31] reproduced this experiment and confirmed the phase diagram. In his schematic phase diagram shown in Fig. 1.2, he found a new type of islands, 3D-c(2×2) islands, however, this structures are the same as 2D c(2×2) actually. O. Romanyuk, K. Hattori et al. [32] pointed that c(2×2) structures should be p(2×2) or c(2×2)-like structures, because β-$FeSi_2$ surface unit cell is two times larger than Si(001)1×1 unit cell and not rotated with respect to Si surface unit cell, that is, β-FeSi2(100)[010]||Si(001)$\langle 110 \rangle$. Not all the structures have been well known even by now.

The most interesting results in Someta ' s data [31] are nano-carpet shown in Fig. 1.3 (a) and (b). Being different from traditional nano-film having steps, the nano-carpet surface continuously connect on terraces and substrate steps in Fig. 1.3 (b). From the line profiles in Fig. 1.3 (c), the red line show connections between two nano-carpets, and the blue line show the steps. The area ratio of boundary-less calculated to be 84 % from Fig. 1.3 (a). Better quality of nano-carpet is possible by optimized SPE conditions. This type of morphology is predicted to lead to high mobility, because transporting electron is not scattered by domain and step boundaries. S. Hajjar et al., [33] found the similar morphology, but nano-carpet and clusters coexist in their STM images. And they thought the films were α-FeSi2 by XPD measurements.

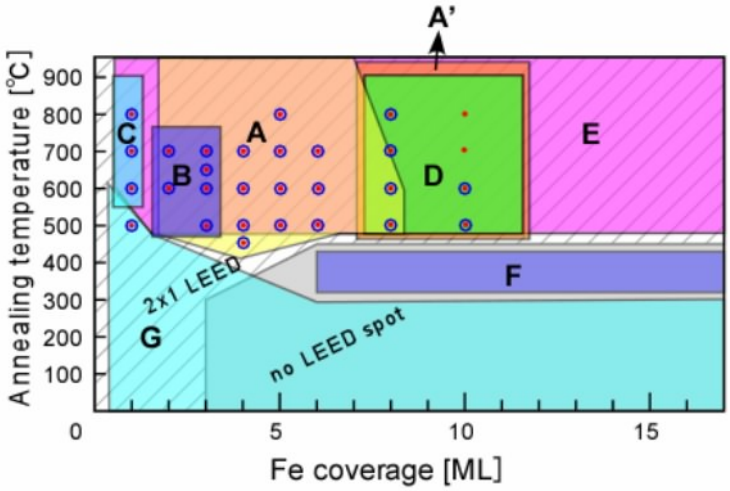

Fig. 1.2. Schematic phase diagram of iron silicides SPE-grown on Si(001)2×1 surfaces. (A) 2D c(2×2) islands, (A ') 3D c(2×2) islands (B) rectangle-like islands, (C) 3D elongated islands, (D) 3D layered islands, (E) 3D dome-like islands, (F) eddy and cracked structures, and (G) small clusters. [31].

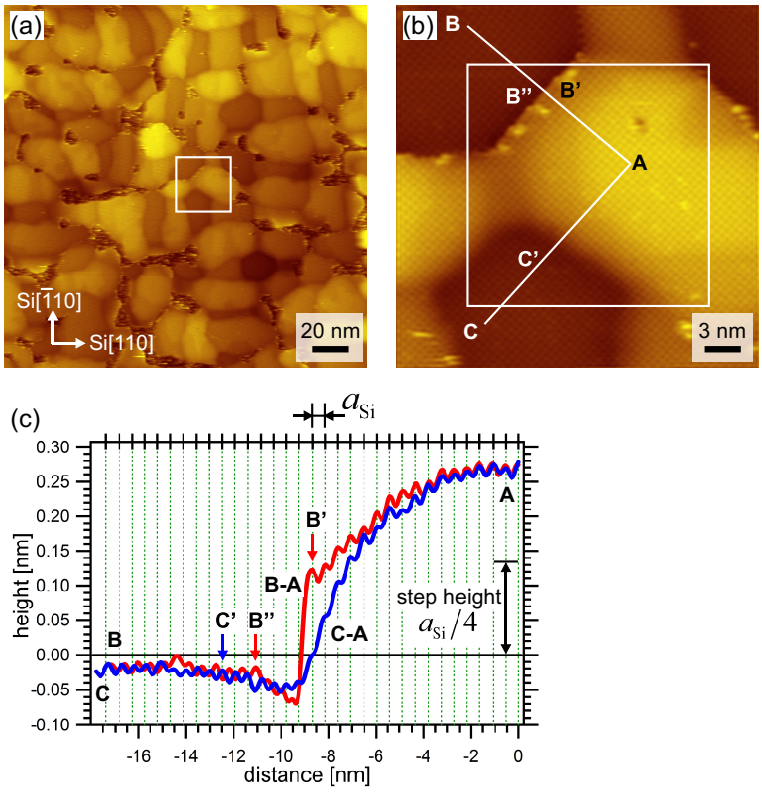

Fig. 1.3. (a) and (b) STM image of nano-carpet, Vs = -1.5 V. θ Fe = 4 ML, Ta = 450 °C. The area between nano-carpets is marked in (a). (b) is from another scan from the area in (a). (c) Line profiles are measured form the red and blue lines in (b). [31].

β-$FeSi_2$ belongs to base-centered orthorhombic and Cmca(64)-D2h18 space group. The lattice constant a, b and c are 9.863 Å, 7.791 Å and 7.833 Å, respectively. The bulk model is shown in Fig. 1.4. Forty-eight atoms (16 Fe and 32 Si atoms) are in every unit cell, and can be classified as Fe(I), Fe(II) and Si(I), Si(II) in crystallography. The in-plane unit lengths of β-$FeSi_2$ are $\sim$1.4 % longer in b direction and longer $\sim$2.0 % longer in c direction for Si substrate. So β-$FeSi_2$ nano-carpet is expected compressive strain from the lattice mismatch in in-plane direction.

Figure 1.5 shows the reciprocal lattice of β-$FeSi_2$ (100) and Si(001) substrate in the first quadrant of k_x-k_y plane, which corresponds to (100) plane of β-$FeSi_2$. The $\beta 0kl$ spots of β-$FeSi_2$ nano-carpet was extinct when k is an odd number or, k is zero and l is an odd number by systematic absence of reflection because β-$FeSi_2$ has $p2gg$ symmetry in (100) plane [32]. The size of circle also reflects the intensity of diffraction spot by systematic absence of reflection. Considering the double domain of Si substrate, $\beta 042$ spots on domain A and $\beta 024$ spots on domain B are measured very close position depended on the difference between b and c. In this paper, the symmetric property of reciprocal lattice spots of β-$FeSi_2$ is considered.

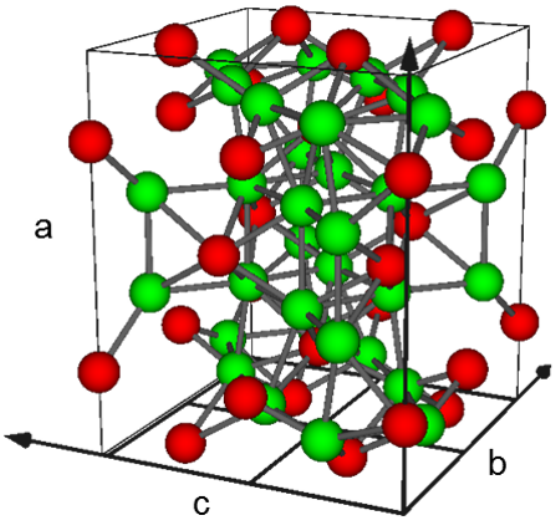

Fig. 1.4. the three dimensional structure of the unit cell of β-FeSi2 in bulk. Fe and Si are marked with red and green spheres, respectively.

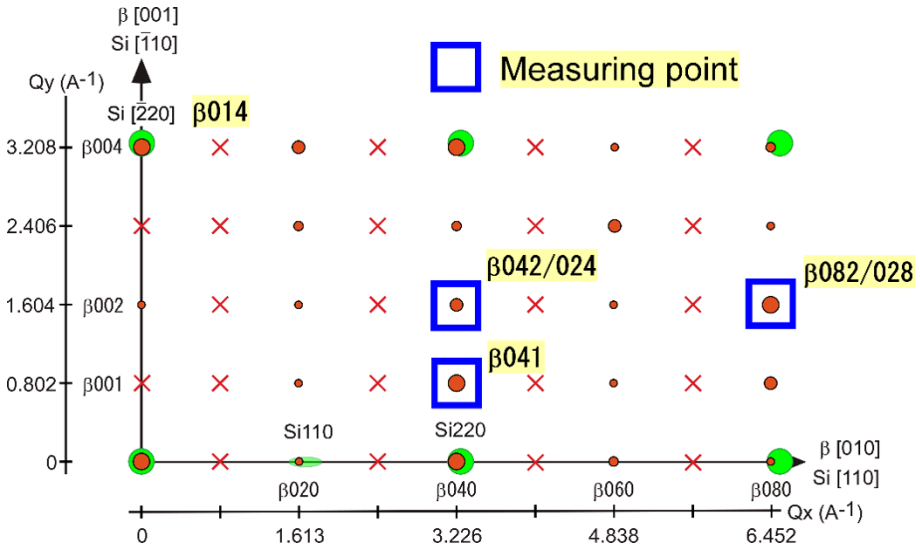

Fig. 1.5. The position of reciprocal lattice spots of β-$FeSi_2$ nano-film (orange circle) and Si(001) substrate (green circle). The scanning region was represented in blue squares.

1.3 3D fabricated surface

3D integrated circuits, which contain multiple layers of active devices, have the potential to dramatically enhance chip performance, functionality, and device packing density. 3D stacking techniques are inevitable for the continuous progress of scaling-down in Si device developments. Recent 3D-structured field-effect transistors (FETs) have surfaces with different orientations; for instance, a fin-type tri-gate structure has one top-surface and two side-surfaces [34–36]. The electric connection between metal wires on these surfaces—that is, the wiring interconnects at sharp edges of top- and side-surfaces—is one of the issues for developing 3D devices. In other words, 3D angular-shape interconnects of wires at nanoscale with high performance is one of the important elements for the circuit-wiring techniques. The technique should be improved based on the knowledge of designing topologies and estimating performances for interconnects of metal wires on differently oriented 3D-surfaces depending on surface roughness, impurity, crystalline grain boundary, etc.

So far, metal films grown on 2D planar-surfaces have been widely studied [37–39], and factors such as the roughness contributing to the conductivity degradation in the films have been revealed [40–43]. The first-step study for the conductivity performance in the 3D integrated circuits focused on the mobility on 2D side-surfaces perpendicular to the planner substrate-surfaces in 3D fabricated structures [44–53]. Mao *et al.* have reported the mobility degradation by the process-induced roughness on the side-surface of a Si nanowire, and concluded that the improvement of side-surface quality is mandatory [44]. Similar phenomena were seen in GaAs-nanowire FET [45]. The mobility degradation due to the roughness has been demonstrated in simulations [46–53]. Though the conductivity in metal wires on

isolated 2D planner- or side-surfaces has been well discussed, there are no reports for the metal conductivity interconnected between 3D surfaces with different orientations, probably owing to the difficulty of measuring the intrinsic conductivity in 3D angular-interconnects, which is mainly caused by the diffuse scattering at a rough surface [40–53]. Toward the next-step study for 3D stacked devices, metal electrodes grown on atomically-flat surfaces in 3D-structured substrates are required for the evaluation of the 3D interconnect resistivity by eliminating the extra factors, such as roughness.

Recently 3D Si structures with arbitrarily-orientated side-surfaces and their atomically well-ordered surfaces have been successfully produced [54–57]. RHEED and STM have proven the atomically-ordered vertical side-surfaces in 3D space in addition to general 2D planar surfaces.

1.4 Purpose of this study

In this paper, the purpose is development of a new analysis method in 2D RSM and evaluation of surface arrangement in 3D nano-fabricated materials using diffraction, in order to improve diffraction techniques to both fundamental and applied science. The development of the analysis method corresponds to fundamental approach to estimate in-plane strain from the spot shape broadening. I applied the general method which was reported to estimate strain and domain size so far. The new method can be evaluated from the comparison with the result of applying general methods. As practical approach of diffraction method, I performed RHEED observation of 3D nano-fabricated materials. So far, there were no reports indicating atomically-flat and reconstructed artificial side-surfaces of 3D nano-fabricated structures. Thus, this is the first demonstration proving the creation of the well-ordered side-surfaces by nano fabrication, using diffraction.

In chapter 2, I describe the development of a new analysis method to estimate in-plane strain which is introduced in inhomogeneous epitaxial film. The measurement spot was only three spots with in-plane XRD. The conventional analysis using spot center and spot width, such as Scherrer and W-H methods, led to less accuracy for domain size and strain. In contrast, in new 1D and 2D fitting analysis using spot shape, we can evaluate strain with a certain accuracy by comparison of the residual sum of squares between experiment and simulation. So far, there are some reports for 1D fitting and a report for 2D fitting with fixed models showing more plausible pictures; 2D fitting should be a future trend for diffraction analysis but not developed well. Then we propose a new analysis method, that is, a different approach to study inhomogeneous materials. The fitting accuracy, that is,

the residual decreasing, was drastically improved when multiple domain types were treated, compared with a single domain type. Moreover, inhomogeneous strain distribution model reduced the residual value. We believe that this analysis method should become a standard method to estimate strain distribution for various materials.

In chapter 3, I describe the observation of RHEED from atomically-ordered vertical and facet side-surfaces on the 3D patterned Si substrate to confirm the flat side-surface on 3D devise structure. The surface arrangement in 3D nano-fabricated structure can be confirmed by RHEED in vertical and facet side-surface samples. The simultaneous observation of RHEED from top- and side-surfaces was also succeeded. In additional trial experiment, I measured the electric resistance on 3D devise structure. I revealed the characterization the intrinsic conductivity of the 3D angular-interconnects of the Au wire at the facet edges by the comparison of resistance in the different waring samples.

I finally summarized the results obtained in the present works, and suggest some future subjects in Chapter 4. In this paper, I showed the development of a new analysis method of XRD and application of RHEED to measurement of the side-surface of 3D devise structure.

References

[1] P. Scherrer, Nachr. Ges. Wiss. Gttingen, **26**, 98 (1918).

[2] A. L. Patterson, Phys. Rev. **56**, 978 (1936).

[3] R. C. Garvie, J. Phys. Chem., **69**, 1238 (1965).

[4] J. I. Langford and A. J. C. Wilson, J. Appl. Cryst. **11**, 102 (1978).

[5] A. Monshi, M. R. Foroughi, and M. R. Monshi, World J. Nano Sci. Eng. 2 **2**, 154 (2012).

[6] A.R. Stokes and A.J.C. Wilson, Proc. Phys. Soc. **56**, 174 (1944).

[7] G. K. Williamson and W. H. Hall, Acta Metall. **1**, 22 (1953).

[8] G. K. Williamson and R. E. Smallman, Philos. Mag. **1**, 34 (1955).

[9] G. B. Mitra, Acta Cryst. **17**, 765 (1964).

[10] R. Yogamalar, R. Srinivasan, A. Vinu, K. Ariga, and A. C. Bose, Sol. State Commun **149**, 1919 (2009).

[11] A. K, Zak, W. H. A. Majid, M. E. Abrishami, and R. Yousefi, Sol. State Commun **13**, 251 (2011).

[12] V. Chamard, T. Schülli, M. Sztucki, T. H. Metzger, E. Sarigiannidou, J.-L Rouvière, M. Tolan, C. Adelmann, and B. Daudin, Phys. Rev. B **69**, 125327 (2004).

[13] T. Takeuchi, K. Tatsumura, T. Shimura, and I. Ohdomari, J. Appl. Phys. **106**, 073506 (2009).

[14] H. Stanchu, V. Kladko, A. V. Kuchuk, N. Safriuk, A. Belyaev, A. Wierzbicka, M. Sobanska, K. Klosek, and Z. R. Zytkiewicz, Nanoscale Research Lett. **10**, 51 (2015).

[15] J. Stangl, A. Daniel, V. Holy, T. Roch, G. Bauer, I. Kegel, T.H. Metzger, T. Wiebach, O.G. Schmidt, and K. Eberl, Appl. Phys. Lett. **79**, 1474 (2001).

[16] A. Durand, M. Kaufling, D. Le-Cunff, D. Rouchoin, and P. Gergaund, Mater. Sci. Semicond. Process. **70**, 99 (2017).

[17] C. J. Davisson and L. H. Germer, Phys. Rev. **30**, 705 (1927).

[18] C. P. Thomson, Proc. Roy. Soc. **A117**, 600 (1928).

[19] S. Kikuchi, Japan. J. Phys. **5**, 83 (1928).

[20] Rupp, Ann. d. Phys. **85**, 981 (1928).

[21] K. Ploog and A. Fischer, Appl. Phys. **13**, 111 (1977).

[22] S. Ino, Jpn. J. Appl. Phys. **16**, 6 (1977).

[23] Y. Horio, Y. Hashimoto, and A. Ichimiya, Appl. Surf. Sci. **100**, 292 (1996).

[24] T. Abukawa, T. Yamazaki, K. Yajima, and K. Yoshimura, Phys. Rev. Lett. **97**, 245502 (2006).

[25] K. Yamaguchi nd K. Mizushima, Phys. Rev. Lett. **86**, 26 (2001).

[26] D. Leong, M. Harry, K. J. Reeson, and K. P. Homewood, Nature **387**, 686 (1997).

[27] M. Suzuno, Y. Ugajin, S. Murase, T. Suematsu, M. Uchikoshi and M. Isshiki, J. Appl. Phys. **102**, 103706 (2007).

[28] K. Takakura, T. Suematsu, Y. Ikura, and F. Hasegawa, Jpn. J. Appl. Phys. **39**, L789 (2000).

[29] O. Kubaschewski (1982) Iron Binary Phase Diagrams, Berlin, Springer.

[30] H. Nakano, K. Maetani, K. Hattori, and H. Daimon, Surf. Sci. **601**, 5088 (2007).

[31] M. Someta, master theses. (2008).

[32] O. Romanyuk, M. Someta, K. hattori, and H. Daimon, Phys. Rev. B **90**, 155305 (2014).

[33] S. Hajjar, G. Garreau, S. Pelletier, P. Bertoncini, P. Wetzel, G. Gewinner, M. Imhoff, and C. Pirri, Surf. Sci. **532**, 940 (2003).

[34] D. Hisamoto, W.-C. Lee, J. Kedzierski, H. Takeuchi, K. Asano, C. Kuo, E. Anderson, T.-J. King, J. Bokor, and C. Hu, IEEE Trans. Electron Devices **47**, 2320 (2000).

[35] J.-P. Colinge, Solid-State Electron. **48**, 897 (2004).

[36] C. Auth, C. Allen, A. Blattner, D. Bergstrom, M. Brazier, M. Bost, M. Buehler, V. Chikarmane, T. Ghani, T. Glassman, R. Grover, W. Han, D. Hanken, M. Hattendorf, P. Hentges, R. Heussner, J. Hicks, D. Ingerly, P. Jain, S. Jaloviar, R. James, D. Jones, J. Jopling, S. Joshi, C. Kenyon, H. Liu, R. McFadden, B. Mcintyre, J. Neirynck, C. Parker, L. Pipes, I. Post, S. Pradhan, M. Prince, S. Ramey, T. Reynolds, J. Roesler, J. Sandford, J. Seiple, P. Smith, C. Thomas, D. Towner, T. Troeger, C. Weber, P. Yashar, K. Zawadzki, and K. Mistry, VLSI Symp. Tech Dig., 2012, p. 131.

[37] B. Feldman, R. Deng, and S. T. Dunham, J. Appl. Phys. **103**, 113715 (2008).

[38] E. Buitrago, M. F.-Bolaños, S. Rigante, C. F. Zilch, N. S. Schröter, A. M. Nightingale, and A. M. Ionescu, Sens. Actuators B **193**, 400 (2014).

[39] N. A. Lanzillo, O. D. Restrepo, P. S. Bhosale, E. C. Silva, C.-C. Yang, B. Y. Kim, T. Spooner, T. Standaert, C. Child, G. Bonilla, and K. V. R. M. Murali, Appl. Phys. Lett. **112**, 163107 (2018).

[40] K. C. Elsom and J. R. Sambles, J. Phys. F **11**, 647 (1981).

[41] E. Z. Luo, S. Heun, M. Kennedy, J. Wollschläger, and M. Henzler, Phys. Rev. B **49**, 4858 (1994).

[42] E. T. Krastev, L. D. Voice, and R. G. Tobin, J. Appl. Phys. **79**, 6865 (1996).

[43] J. S. Chawla, F. Gstrein, K. P. O'Brien, J. S. Clarke, and D. Gall, Phys. Rev. B **84**, 235423 (2011).

[44] K. Mao, T. Saraya, and T. Hiramoto, Jpn. J. Appl. Phys. **52**, 04CC11 (2013).

[45] S. C. Lee, A. Neumann, Y.-B. Jiang, K. Artyushkova, and S. R. J. Brueck, Nanotechnology **27**, 375707 (2016).

[46] S. M. Goodnick, D. K. Ferry, X. W. Wilmsen, Z. Liliental, D. Fathy, and O. L. Krivanek, Phys. Rev. B **32**, 8171 (1985).

[47] C.-Y. Mou and T.-M. Hong, Phys. Rev. B **61**, 12612 (2000).

[48] J. Wang, E. Polizzi, A. Ghosh, S. Datta, and M. Lundstrom, Appl. Phys. Lett. **87**, 043101 (2005).

[49] C. Buran, M. G. Pala, M. Bescond, M. Dubois, and M. Mouis, IEEE Trans. Electron Devices **56**, 2186 (2009).

[50] S. G. Kim, M. Luisier, A. Paul, T. B. Boykin, and G. Klimeck, IEEE Trans. Electron Devices **58**, 1371 (2011).

[51] H.-E. Jung and M. Shin, IEEE Trans. Electron Devices **60**, 1861 (2013).

[52] S. L. Tripathi and R. A. Mishra, J. Electron Devices **86**, 1537 (2013).

[53] H. Ryu, Nanoscale Res. Lett. **11**, 36 (2016).

[54] A. N. Hattori, K. Hattori, S. Takemoto, H. Daimon, and H. Tanaka, Surf. Sci. **644**, 86 (2016).

[55] A. N. Hattori, S. Takemoto, K. Hattori, H. Daimon, and H. Tanaka, Appl. Phys. Express **9**, 085501 (2016).

[56] H. Yang, A. N. Hattori, A. Ohata, S. Takemoto, K. Hattori, H. Daimon, and H. Tanaka, Jpn. J. Appl. Phys. **56**, 111301 (2017).

[57] S. Takemoto, A.N. Hattori, K. Hattori, H. Tanaka, and H. Daimon, Jpn. J. Appl. Phys. (2018) in press.

Chapter 2. Development of a new analysis method in 2D RSM

2.1 Introduction

In this chapter, I describe the development of a new analysis method in two-dimensional reciprocal space map to estimate in-plane strain of β-$FeSi_2$ (100) nano-carpet. The general analysis methods of XRD estimate strain and domain size by using peak position and peak broadening [1–6]. This analysis method was known to low accuracy empirically. Recently, the peak shape fitting method have been used to estimate strain and domain size. This method considers peak shape as superposition of many peaks derived from different strain or domain size and can estimate strain or domain size distribution. There are only a few report to estimate strain distribution by peak shape fitting [7–10]. Cervolino reported the distribution of domain size in Au particle by 1D peak shape fitting. Figure 2.1 shows the experimental (black continuous line) and the simulated (gray) intensities in $\theta-2\theta$ measurement. The result of peak shape fitting shows in Fig. 2.2. This figure shows the distribution of domain size, that is this figure shows the mass rate of domain sizes. Durand also reported the peak shape fitting in 2D reciprocal space mapping. In this paper, the strain of sample was calculated from finite element method(FEM) simulation (Fig.2.3(a)). The 2D peak shape of reciprocal lattice spot simulated by using the calculated strain. The author simulated 4000 peak shapes with different strain and compared to experimental peak shape. This analysis method treated 2D peak shape, but only a set of strain can be calculated in this paper. Thus a new analysis method in 2D RSM is required to estimate distribution of in-plane strain. At first, I apply

to general analysis methods in peak center fitting and peak shape fitting. Then I expand a peak shape fitting into two-dimension and consider strain distribution. Finally, I evaluate a new method by comparison with the results of previous method.

In section 2.2, I introduce the principal and geometry of XRD. The conditions of the experiment are described here.

The sample fabrication of β-$FeSi_2$ (100) nano-carpet is shown in section 2.3.

The results of RSM of β041, β042, β082 and Si220 spots are described in section 2.4. The characteristic peak broadening is confirmed in each spot. And the instrumental peak broadening is estimated from the peak broadening of Si220 spot in scanning direction and perpendicular direction. In section 2.5, I use some general analysis method to evaluate in-plane strain and domain size. The accuracy become better and better to review the assumption of fitting. Finally, the superposition of spot with a certain weight is considered to estimate strain distribution.

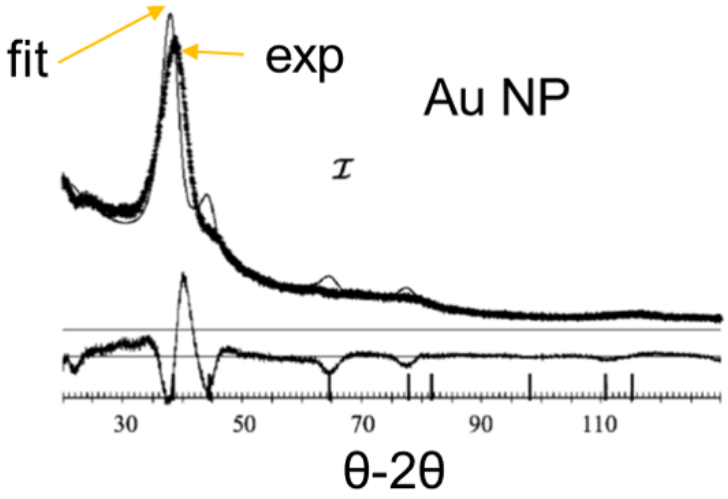

Fig. 2.1. The experimental (black continuous line) and the simulated (gray) intensities. The fitting peak shape is consists of a various of peaks from different domain sizes [7].

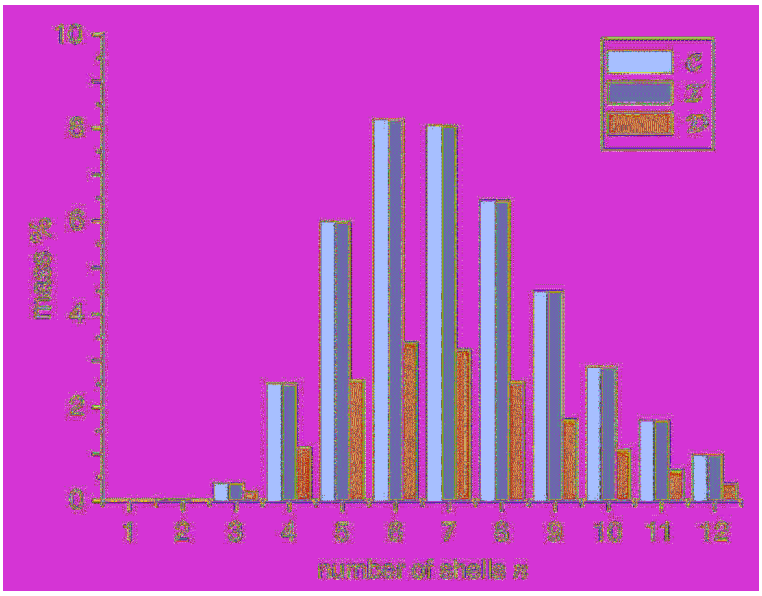

Fig. 2.2. The distribution of domain size calculated by fitting [7].

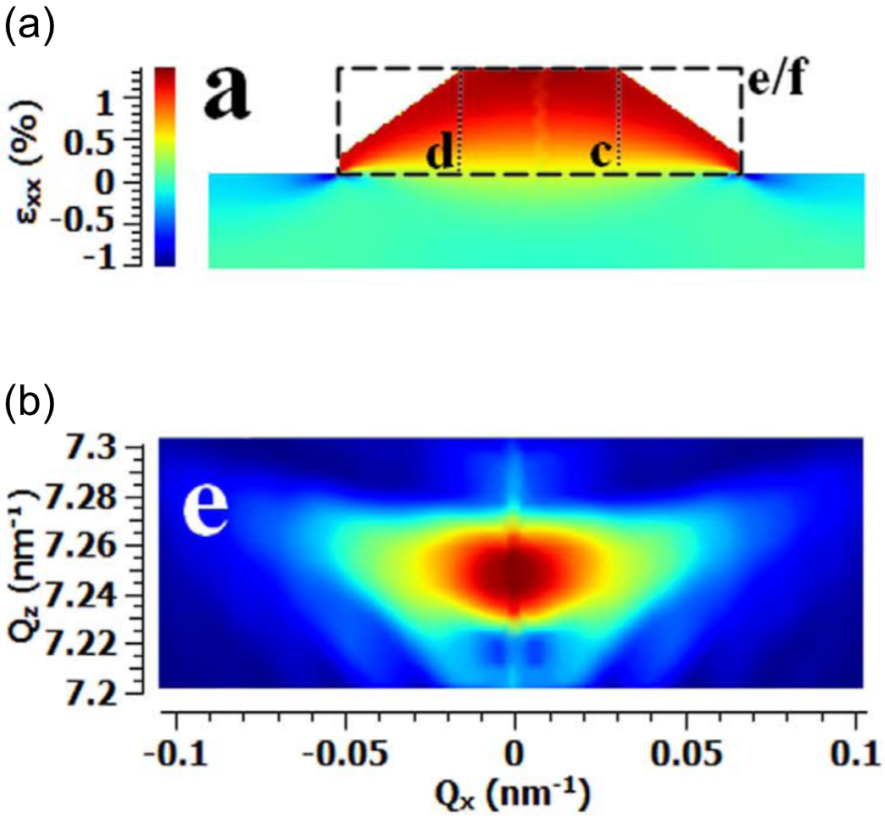

Fig. 2.3. (a) The strain of sample calculated from FEM simulation. (b) 2D peak shape of SiGe004 spot simulated by using the calculated strain [10].

2.2 Method

2.2.1 In-plane XRD

An X-ray diffraction is measurement technique used for a crystal structure evaluation widely. In general, out of plane XRD is used for measuring RSM in perpendicular direction to surface (Fig. 2.4(a)). The reciprocal lattice of single crystal and poly-crystal shows orange spots and blue circle, respectively. When out of plane XRD measurement is expanded into in-plane direction, crystal information in the in-plane direction can be observed (Fig. 2.4(b)). In-plane XRD is the technique in which both the incident and diffracted beams are nearly parallel to the sample surface. With standard diffraction geometries, such as the Bragg-Brentano geometry, lattice planes are measured that are parallel to the sample surface. X-rays penetrate to a certain depth into the sample, where they are diffracted; however, if the sample layer is too thin, X-rays are completely transmitted by the sample and no diffraction is observed. In these circumstances, in-plane diffraction is used. Fig. 2.5 shows the geometry of in-plane XRD measurement. The penetrated X-ray beam propagates almost parallel to the sample surface, because the incident angle of the X-ray beam is extremely small, and also the penetrated X-ray beam is refracted so as to propagate along the sample surface. The penetrated X-ray beam come out from the sample surface by diffraction from the lattice planes almost perpendicular to the sample surface. When the sample is thin-film with quite small thickness and a certain crystalline size, diffraction peak can be obtained from the periodicity of the the lattice planes perpendicular to the sample surface. This measurement method is suitable for the estimation of in-plane strain in the β-$FeSi_2$ nano-carpet.

In this paper, the experimental conditions is as below. The incident angle ω was 0.4°

and the diffraction angle in out-of-plane 2θ was 0.4 °. The relationship of scanning regions in the reciprocal-space map is schematically drawn in Fig. 1.5. Here, reciprocal lattice spots contributed from the double domain of the nano-carpet on substrate surface should be considered in n-plane XRD measurement. The unit cell which has b parallel to Si[110] was define as domain A. The unit cell which has c parallel to Si[110] was also defined as domain B Measured β-$FeSi_2$041 spot consists of the contribution from β041 of domain A and β014 of domain B. Actually, the contribution from β014 of domain B does not need to consider because β-$FeSi_2$014 is extinct. Measured β-$FeSi_2$042 and 082 spot also consists of the contribution from β042 and 082 of domain A and β024 and 028 of domain B, respectively. For β041 spot, the measured in-plane scattering-angle $2\theta\chi/\phi$ was 46.67–49.67° with the step of 0.024° and the scan speed of 0.5°/min. The azimuth angle ϕ was 12.14–15.14° with the step of 0.018° from the Si[110] direction. For β042 spot, the measured in-plane scattering-angle $2\theta\chi/\phi$ was 50.95—53.95° with the step of 0.024° and the scan speed of 0.5°/min. The azimuth angle ϕ was 22.5—25.5° with the step of 0.018° from the Si[110] direction. For β082 spot, the measured in-plane scattering-angle $2\theta\chi/\phi$ was 106.0—112.0° with the step of 0.024° and the scan speed of 1.0°/min. The azimuth angle ϕ was 15.46—18.46° with the step of 0.018° from the Si[110] direction. $2\theta\chi/\phi$ was scanned at each ϕ (18 hours in total scan in each spot). Using the weight-centered wavenumber of Cu K_α = 4.075 $Å^{-1}$, the scattering intensities were mapped in the reciprocal space. The reciprocal-space maps of Si220 and $\bar{2}20$ spots were also measured in order to estimate the scattered beam profile as the contribution of instrumental broadening. The beam divergence from the spot center along $2\theta\chi/\phi$ direction was wider than that along ϕ direction. Indeed, the divergences were fitted with 2D Gaussian functions with $\sigma_{2\theta\chi/\phi} = 0.0085\,\mathring{A}^{-1}$ and $\sigma_\phi = 0.0042\,\mathring{A}^{-1}$.

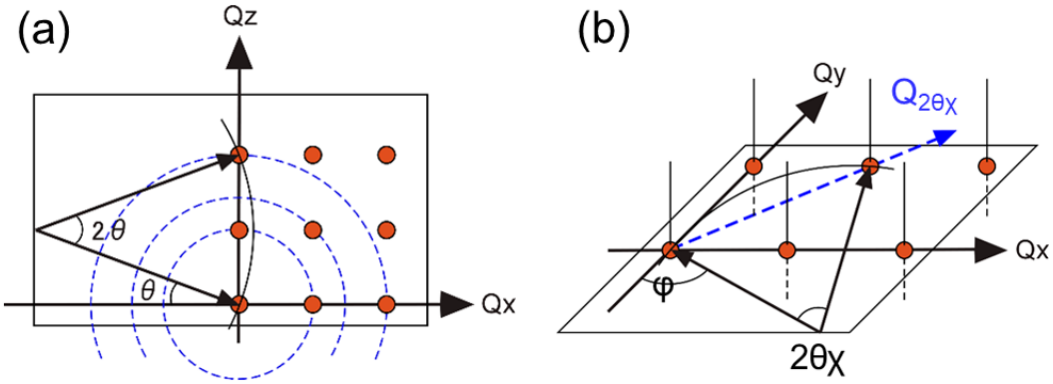

Fig. 2.4. (a) Schematic diagram of out of plane XRD ($\theta - 2\theta$ measurement). (b) Schematic diagram of in-plane XRD ($2\theta\chi/\phi$).

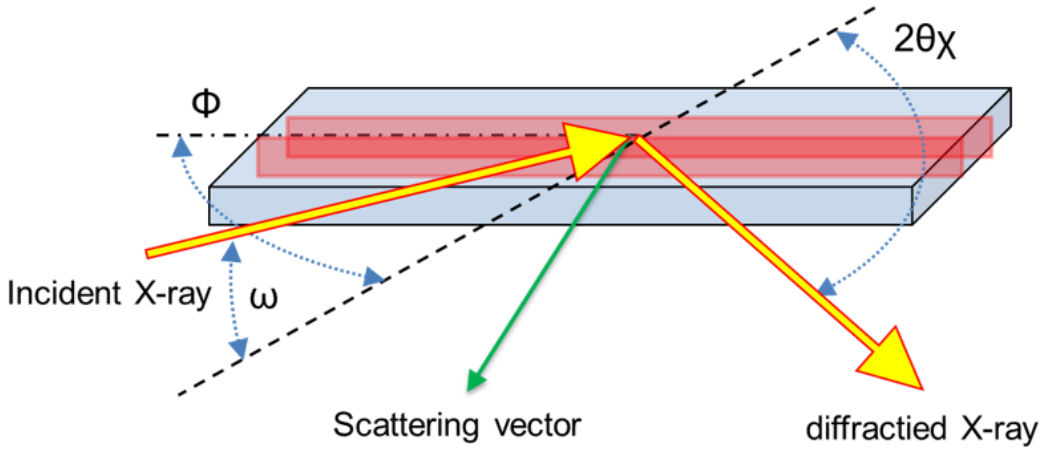

Fig. 2.5. the geometry of in-plane XRD measurement.

2.3 Experiment

2.3.1 Sample fabrication of nano-carpet

A β-$FeSi_2$ nano-carpet on a Si(001) substrate was prepared in an ultra-high vacuum (UHV) system in Fig. 2.6. A mirror polished Si(001) wafer (Sb dope, 0.02 Ωcm, 0.5 mm in thickness) was cut in size of 25 mm (along Si[$\bar{1}$10] direction) × 4 mm, then was transferred to ultra-high vacuum system with a base pressure of less than 1×10^{-8} Pa. The sample was degassed for ∼10 hours and then flashed a few dozen times by direct current heating for ∼1250 °C below 5×10^{-8} Pa to get reconstructed surfaces. Si(001) 1×2 and 2×1 spots were confirmed by RHEED. After confirming reconstructed surfaces, Fe (99.999%) was deposited on the clean Si surface at RT with Θ_{Fe} of 6 monolayers (ML), measured with a thickness monitor, using an alumina-crucible evaporator below 1×10$^-$7 Pa. 1 ML corresponds to 6.78×10^{14} cm^{-2}. The deposited sample was annealed at T_a = 450°C for 10 min, and showed mostly $p(2\times2)$ reconstruction in RHEED at RT, which corresponds to β-$FeSi_2$(100) surface [11]. For the protection against the air exposure, the β-$FeSi_2$ surface was capped with amorphous Si of ∼7 nm thickness, using a Si source on an SiC-wafer heater. A part of the sample of the Si-capped β-$FeSi_2$(100) nano-carpet on the Si(001) substrate was observed by cross-sectional transmission electron microscopy (TEM) with Cs-correction at 200 keV (JEOL, JEM-ARM200F) to confirm the nano-carpet thickness. The region near the sample center was sliced along Si[110] direction. Then the sliced sample was mechanical polished by a dimple grinder, and Ar-ion milled by Precision ion polishing system (GATAN, 691), until the thickness along an electron beam incidence was less than 100 nm. Another part of the Si-capped sample with 10 mm (along Si[$\bar{1}$10]) × 4mm in size was measured by in-plane XRD

with Cu K_α and eight-axis manipulator (RIGAKU, SmartLab,) at RT as shown in Fig. 2.7.

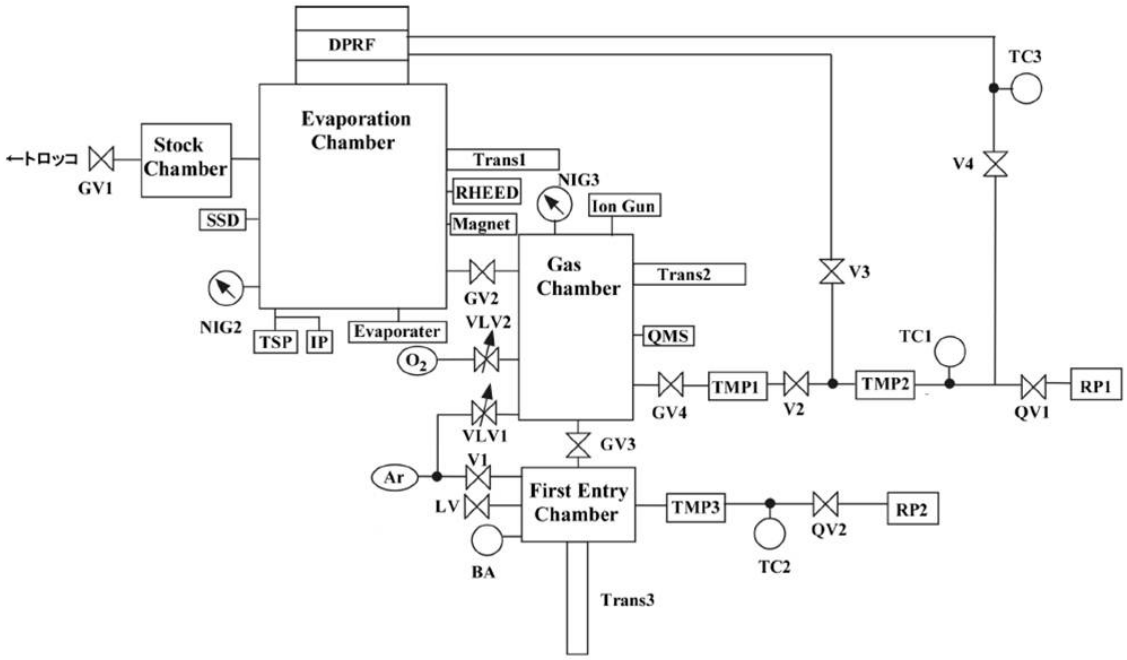

Fig. 2.6. Schematic diagram of UHV system.

Fig. 2.7. The picture of in-plane XRD equipment XRD (RIGAKU, SmartLab).

2.3.2 RHEED observation

In this section, the results of RHEED observation for Si(001) clean surface and β-$FeSi_2$ nano-carpet are described with different incident angle. The results of RHEED observation with [100] and [110] incident are shown in Fig. 2.8 and 2.9, respectively. The schematic diagram below RHEED image represents the top-view of reciprocal lattice rods of the Si(001) reconstructed surface structure. The red and green circle indicate Si(001)1×1 spot and Si(001)2×1 spot, respectively. In both images, the position of measured spots corresponded to that in the schematic diagram. This results show that the Si(001) 1×2 and 2×1 reconstructed surface was obtained after flashing anneal.

Fig. 2.10 and 2.11 represent the results of RHHED observation of Fe/Si(001) sample after deposition of 4ML Fe and post annealing at 450 °C in ten minutes. Incident angle is Si[100] direction (Fig. 2.10) and Si[110] direction (Fig. 2.11). Similarly, the schematic diagram below RHEED image represents the top-view of reciprocal lattice rods of the Si(001) reconstructed surface structure and β-$FeSi_2$ nano-carpet. The red and blue circle indicate Si(001)1×1 spot and p(2×2) spot derived from β-$FeSi_2$ (100), respectively. The streaky spots shown as blue arrow derive from the small periodicity of β-$FeSi_2$ (100) in β[100] direction which corresponds to thickness direction. In both images, the position of measured spots corresponded to that in the schematic diagram. Thus the growth of β-$FeSi_2$ nano-carpet was confirmed by RHEED observation.

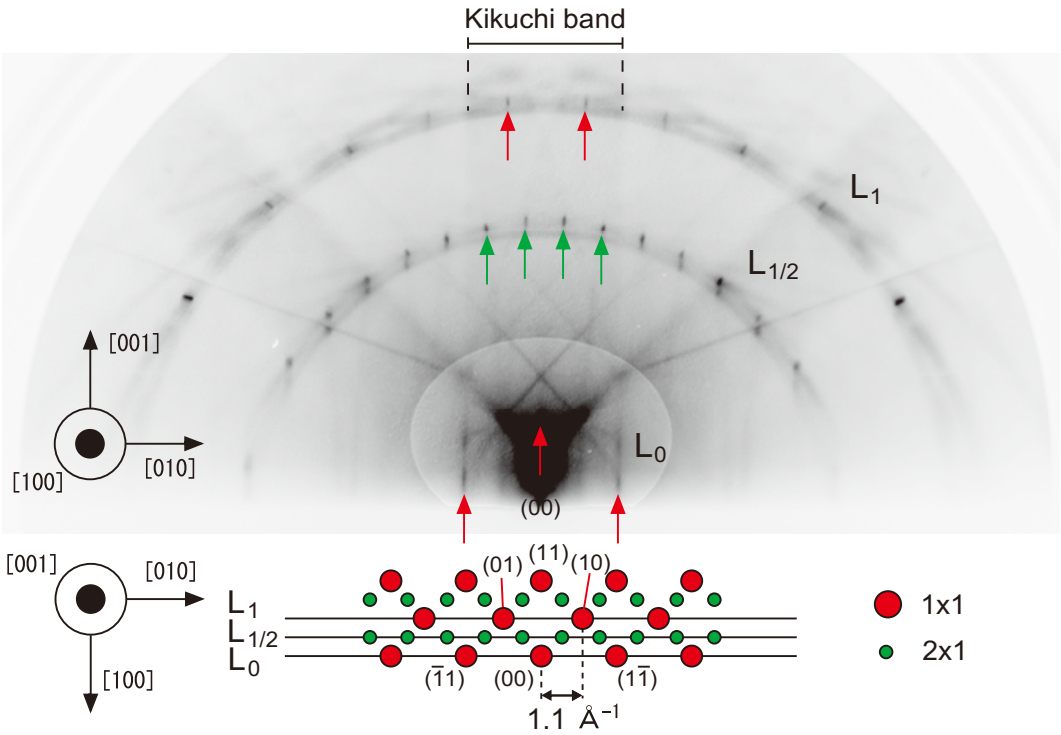

Fig. 2.8. RHEED image of Si(001) 2×1 and 1×2 reconstructed surface, [100] incidence.

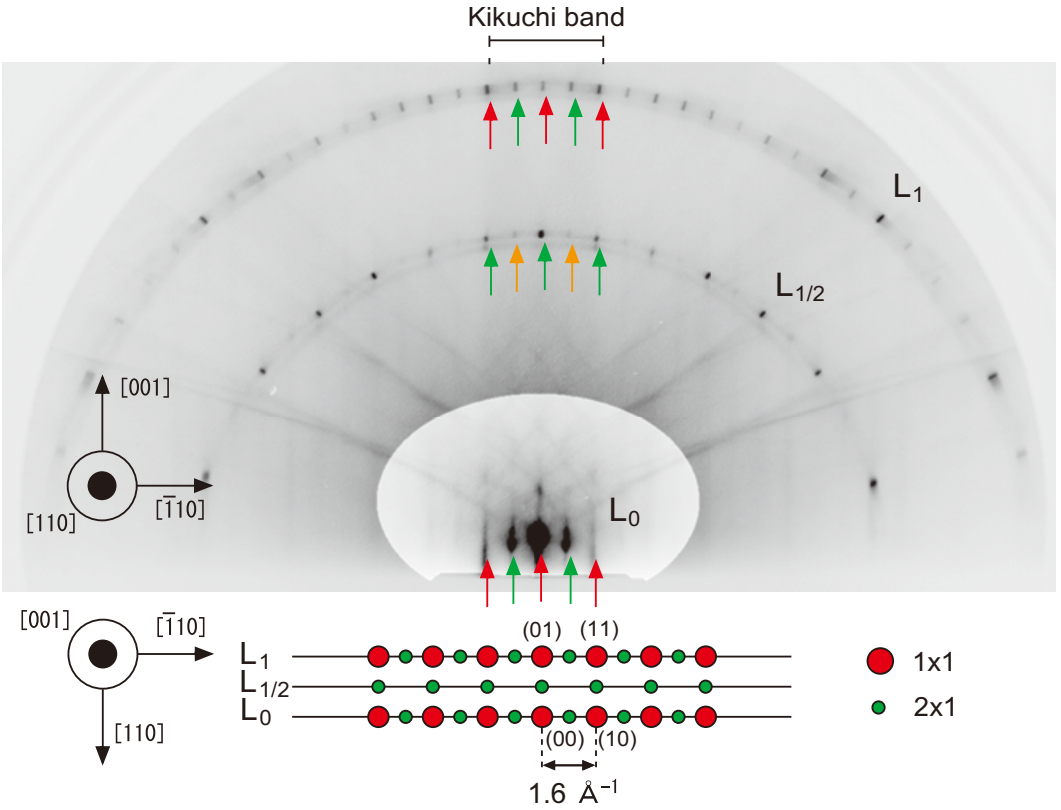

Fig. 2.9. RHEED image of Si(001) 2×1 and 1×2 reconstructed surface, [110] incidence.

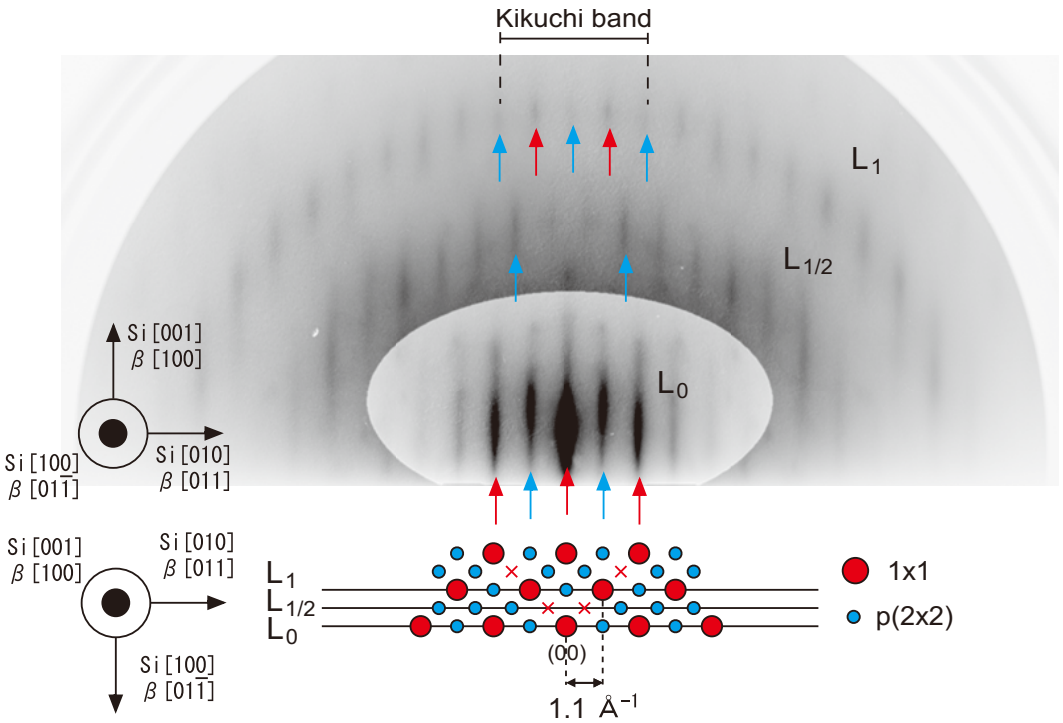

Fig. 2.10. RHEED image of 4 ML Fe/Si(001), [100] incidence.

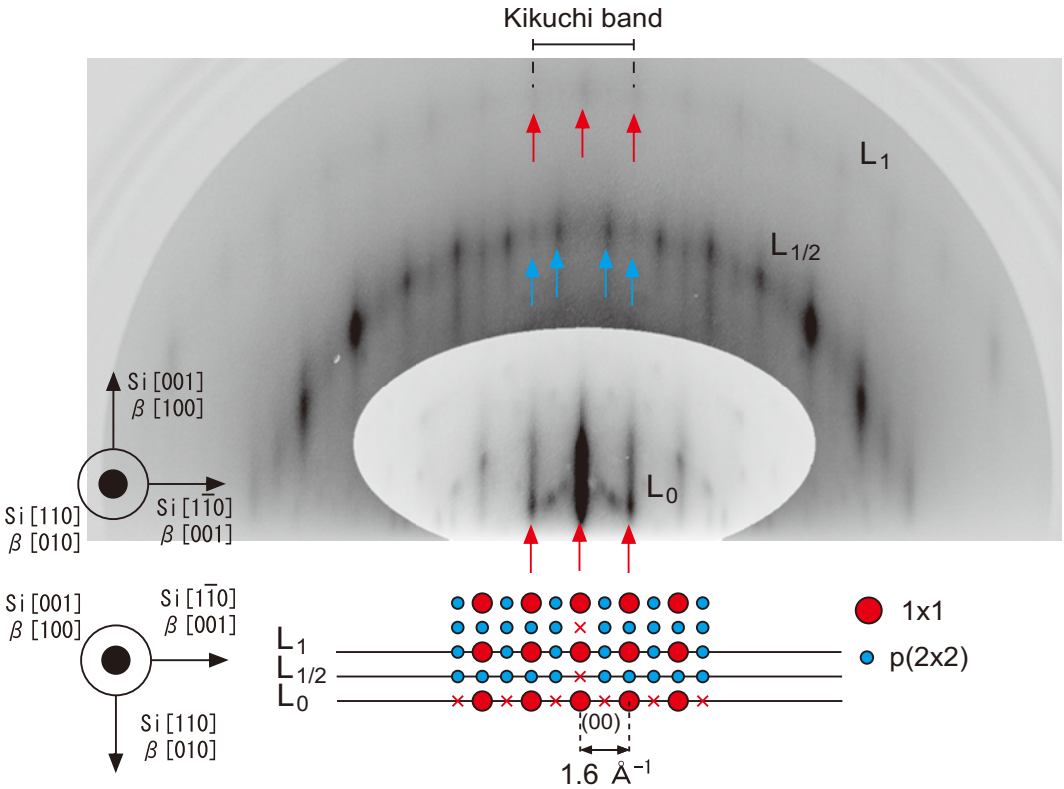

Fig. 2.11. RHEED image of4 ML Fe/Si(001), [110]incidence.

2.4 XRD results

The results of $2\theta\chi/\phi$ measurements of β041, β042/024, β082/028 spots are shown in Fig. 2.12. Blue dots and red lines show experimental results and Gaussian fitting results, respectively. Clear peaks were observed in each spot. Figure 2.13 shows the results of RSM of β041(a), β042/024(b), β082/028(c) and Si220 (d) spots. All peak centers of β-$FeSi_2$ spots is close to the strain-free point and different from the point compressed to the substrate Si lattice. The spots are elongated along the eye-guide line which corresponds to the extended line from origin. The instrumental peak broadening is estimated from the peak broadening of Si220. The line profiles of Si220 spot along kx and ky direction through the peak center are shown in Fig 2.13(e) and (f). The standard deviations of $\sigma_{inst_{kx}}$ $\sim$0.0085 Å^{-1} and $\sigma_{inst_{ky}}$ $\sim$0.0042 Å^{-1} are estimated by Gaussian fitting. The peak broadening of β-$FeSi_2$ spot seem to be wider than that of Si220. So the peak broadening of β-$FeSi_2$ is included from the contribution of strain or domain size of β-$FeSi_2$ nano-carpet. The some analysis are applied to this result of $2\theta\chi/\phi$ measurements and RSM to estimate strain or domain size in next section.

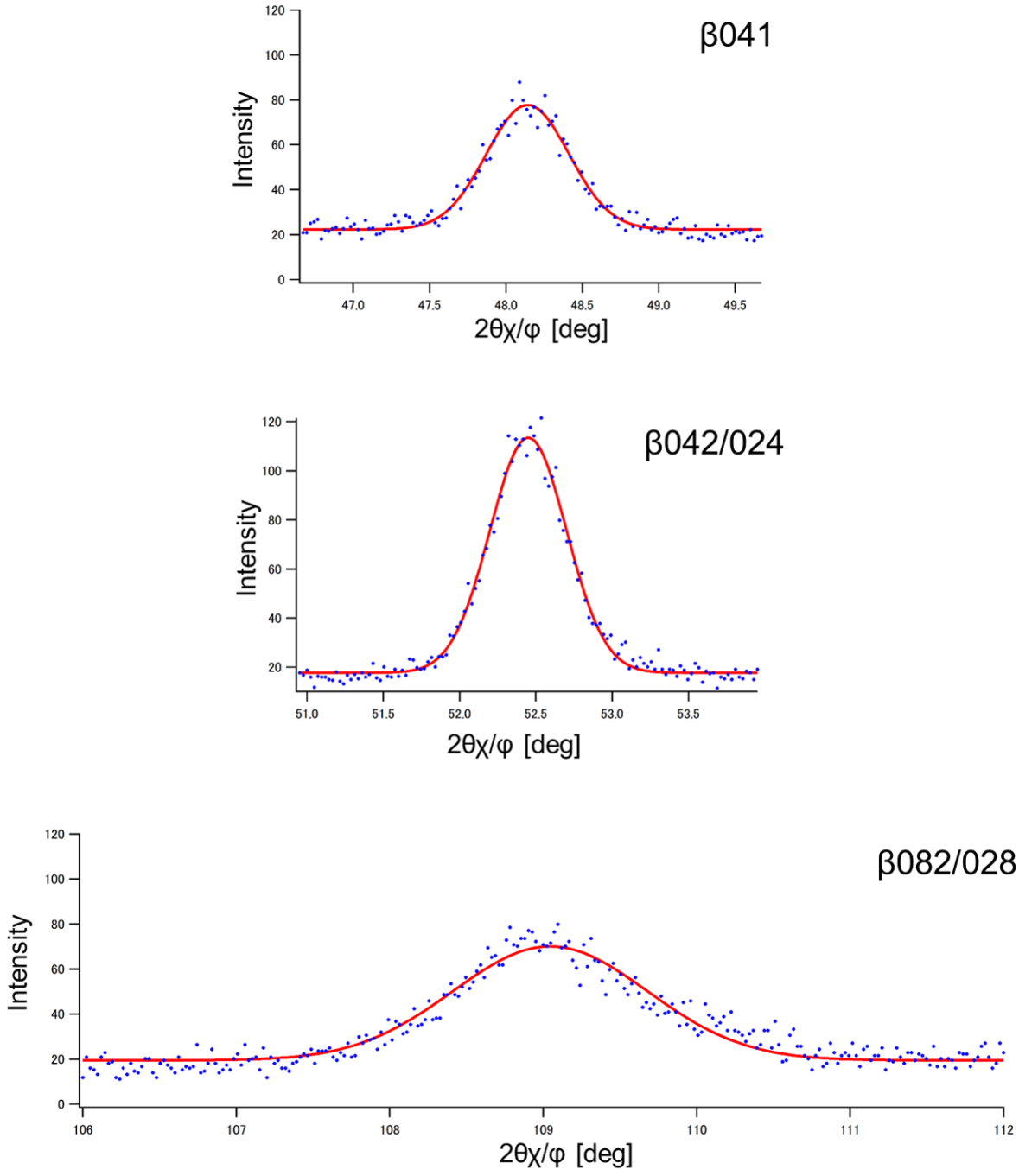

Fig. 2.12. The results of $2\theta\chi/\phi$ measurements of β041, β042/024, β082/028 spots.

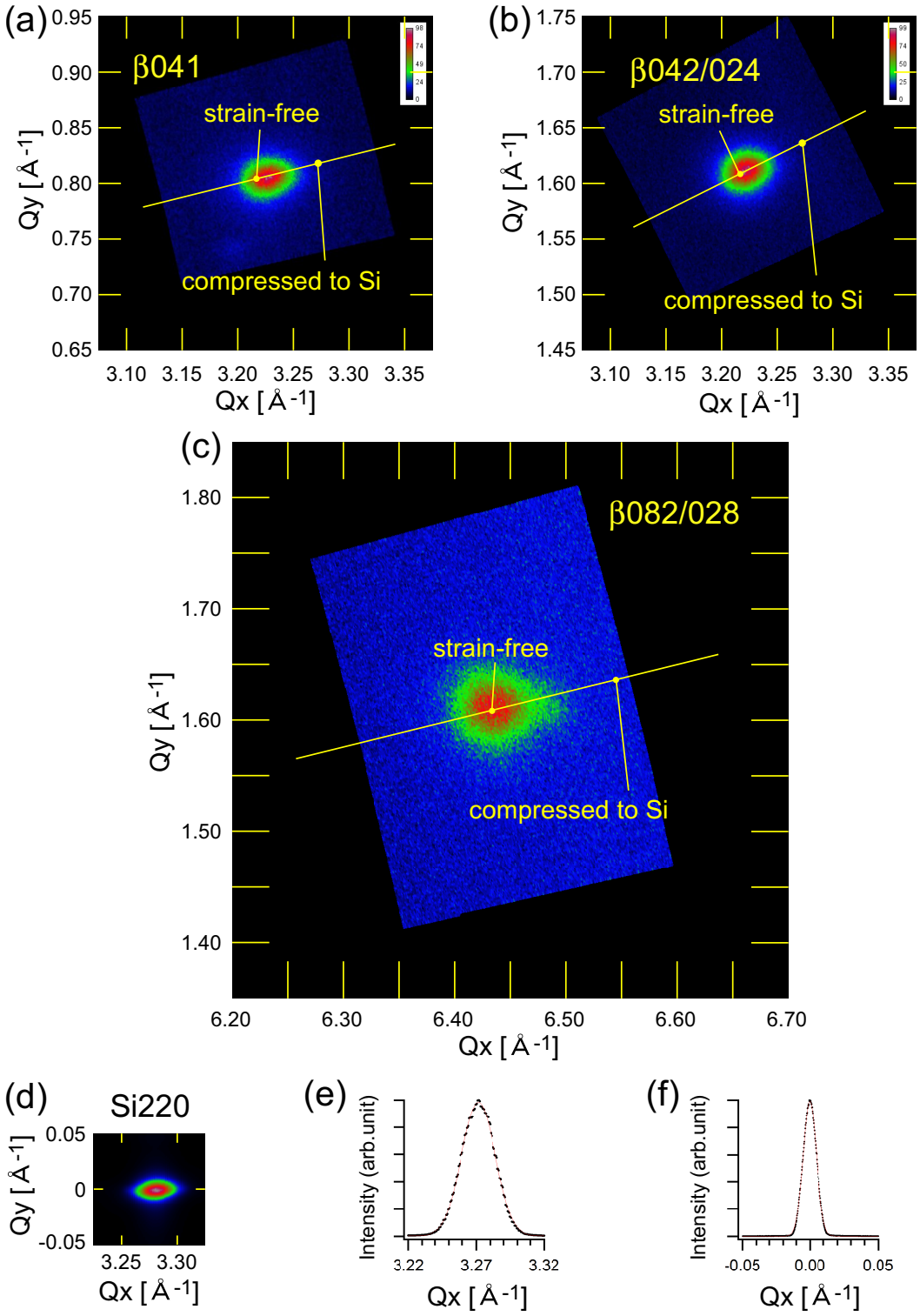

Fig. 2.13. (a, b, c, d) The result of RSM around β041, β042/024, β082/028 and Si220 spots. The guide lines indicate extended line from origin. (e) The line profile of Si220 spot along kx direction through the peak center. (f) The line profile of Si220 spot along ky direction through the peak center.

2.5 XRD analyses in RSM

The analysis method of XRD data is described here. I applied some existing analysis method by using peak center and peak shape fitting. The classical analysis methods by using peak center fitting were applied to check the accuracy firstly. Scherrer method are used for estimating stain and domain size as a most general and easy analysis method. The peak center and peak width reflected strain and domain size, respectively. This method estimates strain and domain size in each spot. Another classical method is Williamson-Hall method. This method estimates strain and domain size distributions by peak broadening of plural spot empirically. As next step, 1D peak shape fitting was applied to estimate in-plane strain. Considering reciprocal lattice vector to show the diffraction peaks, the diffraction intensity was described by using Gaussian function which is generic and analytic. 2D Gaussian fitting is the analysis method to estimate in-plane strain in b and c axes by using 2D peak shape fitting almost same as 1D Gaussian fitting. In 2D anisotropic strain model, the diffraction intensity with anisotropic strain was described by using Laue function. Considering superposition of many peaks derived from different strain, the strain distribution of β-$FeSi_2$ nano-carpet was estimated. The detail of each analysis method is described in each section. Here, two important points of analysis are described as below. One is the correction of the peak broadening. The measurement peak consists of sample component and instrument component. To extract true peak broadening derived from sample, the peak broadening of Si substrate which is non-strain and quite large domain size was treated as instrument component. The peak broadening of Si substrate at each measured angle, ϕ (ϕ = 0, 45, 90 [deg]), were measured by $2\theta\chi/\phi$ measurements as shown in Fig 2.14. The peak broadening in $2\theta\chi/\phi$ direction is

same in each measured angle. The way of correction shows in each analysis method. The other important point of analysis is isotropy and distribution of in-plane strain (Fig 2.15). When a domain introduced same strain in b and c axes, I defined isotropic strain. When all domains introduced same strain in b and c axes, I defined single distribution. The treatment of isotropy and distribution of in-plane strain in each analysis method is shown in Table 1.

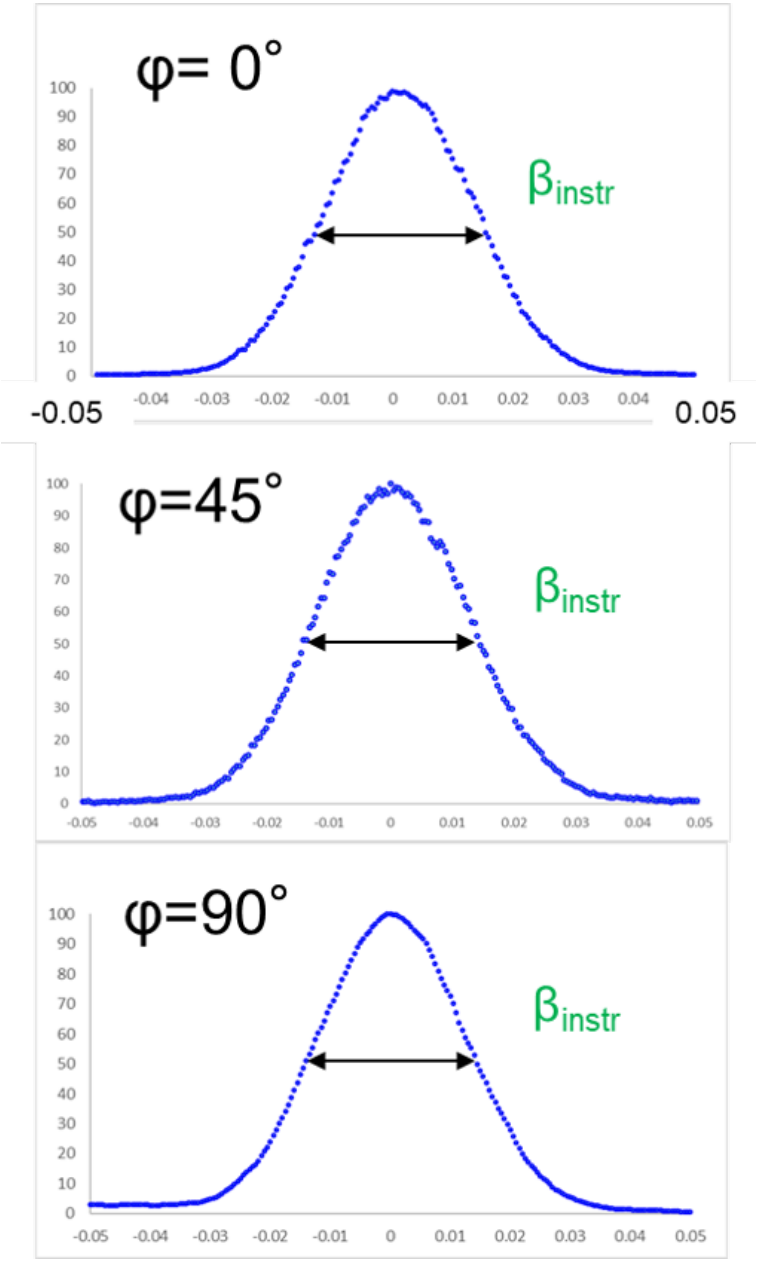

Fig. 2.14. The peak broadening of Si substrate at each measured angle, ϕ (ϕ = 0, 45, 90 [deg].)

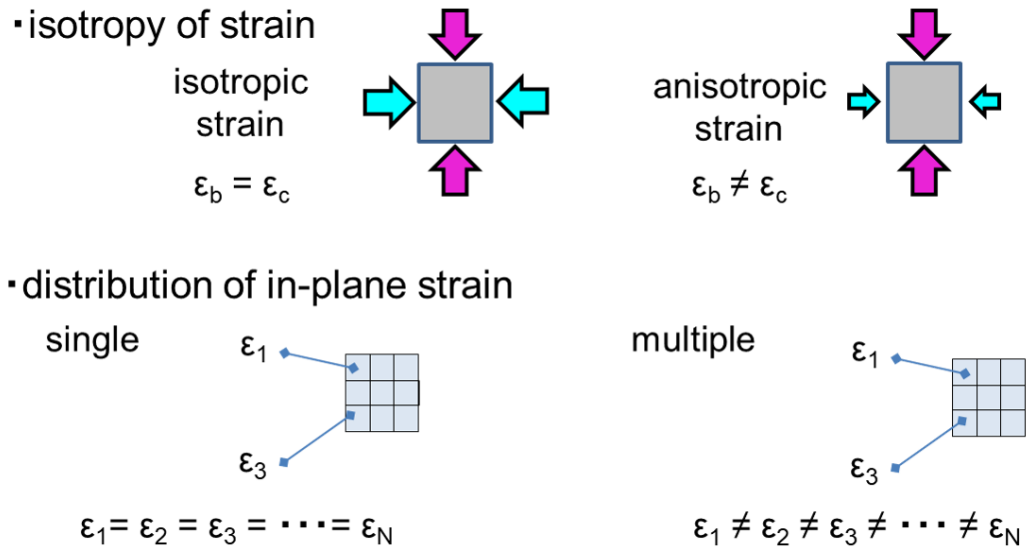

Fig. 2.15. Schematic diagram of the isotropy of strain and distribution of in-plane strain.

Table 1. The treatment of strain in each analysis method

Method	isotropy	distribution
Scherrer	isotropic	single
W-H	isotropic	multi
1DG	isotropic	single
2DG	isotropic	single
2D anisotropic strain	anisotropic	single
Strain distribution	anisotropic	multi

2.5.1 Classical analyses

By using in-plane XRD, an averaged strain of a crystalline film can be simply estimated from $2\theta\chi$ peak-center angles in $2\theta\chi/\phi$ scans at some reflections. A strain, ϵ, at a reflection is described as $\epsilon = (\sin\theta\chi_0/\sin\theta\chi_{meas}) - 1$, where $\theta\chi_0$ and $\theta\chi_{meas}$ correspond to strain-free (reference) and measured peak-center angles, respectively. Table 1 shows $2\theta\chi_0$, $2\theta\chi_{meas}$, and ϵ for β-$FeSi_2$041, β-$FeSi_2$042, and β-$FeSi_2$082 reflections, indicating 0.2% of the averaged strain. Here we should note that in-plane azimuth angles were optimized, in order to cross the reflection peaks of the single crystalline film in the $2\theta\chi/\phi$ scans. Indeed in Table 1, the intensity profiles along lines q_r in Fig. 2.13, which are radial-direction lines from the origin passing through the reflection peaks in 2D-RSM, were analyzed.

Using correct reflection-peak broadening, a lower limit of a crystalline domain size, D_{Sch}, can be estimated by the Scherrer equation. Measured peak broadening, β_{meas}, includes the broadening of instruments, β_{inst}, and the correct peak broadening, β_{cor} is described as $\beta_{cor}^2 = \beta_{meas}^2 - \beta_{inst}^2$ for Gaussian peak shape. In our study, β_{inst} was estimated using a commercial Si(001) wafer. A Si crystal with wider domain-size and lesser strain broadening, such as a Si wafer, leads to $\beta_{cor} \approx 0$, that is, $\beta_{inst} \approx \beta_{meas}$. The instrument broadening in $2\theta\chi/\phi$ scan, $\beta_{inst-2\theta\chi}$ was 0.44° which was full width at half maximum (FWHM) at Si220 reflection. Table 1 also shows β_{meas} in $2\theta\chi$, and D_{Sch} from Scherrer equation:

$$D_{Sch} = (K\lambda)/(\beta_{cor}\cos\theta\chi), \tag{1}$$

where a shape factor K was treated as 0.94. The results implies the β-$FeSi_2$ domain size is larger than 100–230 Å. When a crystal has inhomogeneous strain, a domain size, D_{W-H} and

a strain broadening, $\Delta\epsilon$, are often evaluated by the W-H equation:

$$\beta_{cor}\cos\theta\chi = 4\Delta\epsilon\sin\theta\chi + (K\lambda)/D_{W-H}. \quad (2)$$

Fig. 2.16 shows a plot of $\beta_{cor}\cos\theta\chi$ to $\sin\theta\chi$ for the β-$FeSi_2$ reflections; $\Delta\epsilon \approx 0.48\%$ was evaluated from the slop of the line fitting. The negative intercept ($(K\lambda)/D_{W-H}$) of -0.0013 leading to $D_{W-H} \approx$ -1,100 Å estimation is invalid, because the number of reflections is not enough to decrease an error for the W-H analysis. Thus the usual peak-center and broadening analysis resulting in $\epsilon \approx$ -0.07%, $D_{Sch} \approx$ 100–230 Å, $\Delta\epsilon \approx 0.48\%$, and $D_{W-H} \approx$ -1,100 Å have a little accuracy in our system. This result means that the peak-center and broadening analysis is difficult to estimate in-plane strain of β-$FeSi_2$ nano-carpet.

Table 2. Peak center angle in $2\theta\chi$ of free-strained β-$FeSi_2$ ($2\theta\chi_0$), measured peak-center angle ($2\theta\chi_{meas}$), estimated strain (ϵ), peak broadening (β_{meas}), and estimated lower limit of domain size (D_{Sch}) for 041, 042, and 082 reflections.

β-$FeSi_2$ reflection	$2\theta\chi_0$ [°]	$2\theta\chi_{meas}$ [°]	ϵ	β_{meas} [°]	D_{Sch} [Å]
β041	48.14	48.14	0.00	0.64	200
β042	52.38	52.45	-0.13	0.59	230
β082	108.9	109.04	-0.09	1.49	100

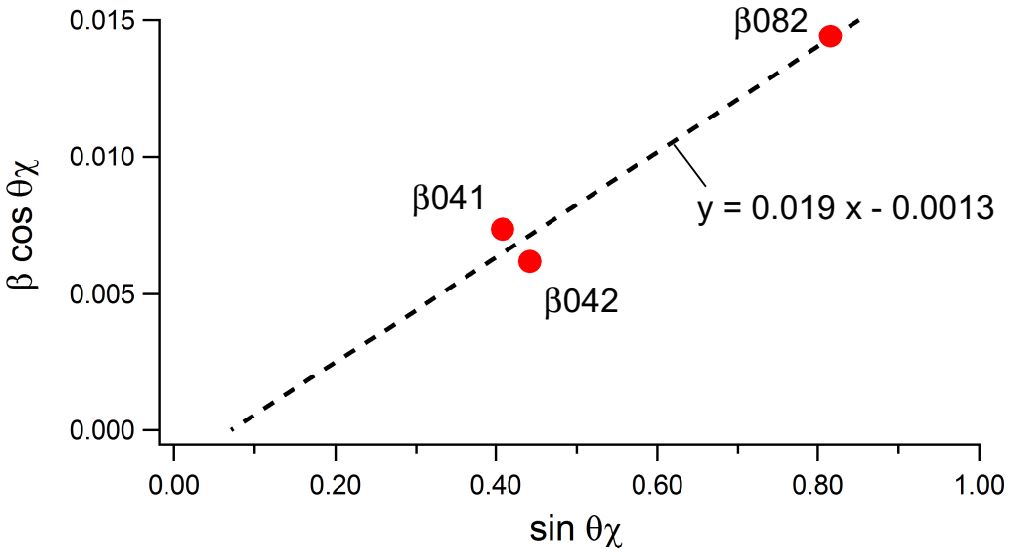

Fig. 2.16. A plot of $\beta_{cor}\cos\theta\chi$ to $\sin\theta\chi$ for β-$FeSi_2$ reflection. The broken straight line indicates approximation line with three spots.

2.5.2 1D-Gaussian fitting analysis

The classical analysis is difficult to estimate in-plane strain of β-$FeSi_2$ nano-carpet. Then 1D peak shape fitting is considered as next analysis method. $2\theta\chi$ was treated to represent diffraction peak, in classical analysis. Here, $2\theta\chi$ is converted to reciprocal lattice vector, $Q_{2\theta\chi}$, by using following equations (Fig. 2.17):

$$Q_0 = 2\pi/\lambda \tag{3}$$

$$Q_{2\theta\chi/\phi} = 2Q_0 \cdot \sin\theta\chi. \tag{4}$$

Considering reciprocal lattice vector, the diffraction intensity can be described by using Gaussian function which is generic and analytic. Since β-$FeSi_2(100)$ in-plane lattice constants b and c are very close, first we assume the averaged in-plane lattice constant $d = (b + c)/2$ and the isotropic strain ϵ_{1DG} and domain size D_{1DG} for b and c directions. Then the intensity of the 1D Gaussian fitting function with a certain of strain and domain size along the radial directions for β-$FeSi_2 0kl$ reflection can be written as

$$I^{0kl}_{1DG-fit}(Q_{2\theta\chi/\phi}; \epsilon_{1DG}, D_{1DG}) = I_{bg} + I_{peak} \cdot \exp\Big[-\frac{\{Q_{2\theta\chi/\phi} - (1+\epsilon_{1DG})^{-1}\sqrt{k^2+l^2}d^*\}^2}{\sigma^2_{inst-2\theta\chi/\phi} + ((2\pi)/(2\sqrt{2\ln 2}\cdot D_{1DG})^2}\Big]. \tag{5}$$

Here, d^* is the averaged reciprocal-lattice unit length: $d^* = (b^* \text{ and } c^*)/2 \sim 0.804$ Å^{-1}, $\sigma_{inst-2\theta\chi/\phi}$ is the standard deviation of the instrument broadening along the reciprocal radial direction corresponding to β_{inst} in the $2\theta\chi/\phi$ scan: $\sigma_{inst-2\theta\chi/\phi} \sim 0.0085$ Å^{-1}, I_{bg} is the background intensity, and I_{peak} is the peak intensity for the $0kl$ reflection. Note that the peak center position is shifted by $\approx -\epsilon_{1DG}\sqrt{k^2+l^2}d^*$ from $\sqrt{k^2+l^2}d^*$ as shown in Fig. 2.18.

To evaluate a possible strain and domain size, we calculated the sum of the squared residuals between the experimental and fitted intensities for each reflection. The squared residual R_{1DG}^{0kl} for reflection $0kl$ is,

$$R_{1DG}^{0kl}(Q_{2\theta\chi/\phi};\epsilon_{1DG,D_{1DG}}) = \frac{\sum_{Q_{2\theta\chi/\phi}}\{I_{1DG-exp}^{0kl}(Q_{2\theta\chi/\phi}) - I_{1DG-fit}^{0kl}(Q_{2\theta\chi/\phi};\epsilon_{1DG},D_{1DG})\}^2}{\sum_{Q_{2\theta\chi/\phi}}\{I_{1DG-exp}^{0kl}(Q_{2\theta\chi/\phi})\}^2}. \quad (6)$$

Then the total squared residual R_{1DG} is,

$$R_{1DG}(\epsilon_{1DG},D_{1DG}) = \sum_{041,042,082} W_{1DG}^{0kl} \cdot R_{1DG}^{0kl}(\epsilon_{1DG},D_{1DG}). \quad (7)$$

Here, W^{0kl} is weight of reflection obtained from the signal-to-noise ratio (W^{041}: W^{042}: W^{082}: = 9: 9: 4).

Fig. 2.19 shows R_{1DG} map with various ϵ_{1DG} (from -1.2 to +0.6%) and D_{1DG} (from 10^1 to 10^3 Å). The smaller residual region is displayed by blue. The minimum of R_{1DG} was $R_{1DG-min}$ = 3.9×10^{-2} at ϵ_{1DG} = -0.2 % and D_{1DG} = 100 Å, however, smaller R_{1DG} region (i.e., 1.1$R_{1DG-min}$) distributes -0.3 to -0.1% in ϵ_{1DG} and 60 to 160 Å in D_{1DG} corresponding to an evaluation error. The R_{1DG} map shows us a much more accurate picture for ϵ_{1DG} and D_{1DG} than the usual Scherrer and W-H analysis, using only three reflections. Such peak shape fittings were reported for nano wire [12] and particles [7, 8]. They calculated domain size distribution by minimalizing square root R_{1DG} defined here for nano particles. Takeuchi et al. estimated strain distribution with a certain domain size by minimalizing residual, $D = \sqrt{R_{1DG}}$. The minimum of D was $\sim$ 0.1, which is a bit smaller than this method ($\sqrt{R_{1DG}} \sim$ 0.2). Although the R_{1DG} map shows a plausible picture for ϵ_{1DG} and D_{1DG}, there were

discrepancies between the experimental and fitted intensities, as shown in blue and red dots, respectively, in Fig. 2.20(a)–2.20(c) for the 041, 042, and 082 reflections. These discrepancies should be caused by the simple assumptions for d, ϵ_{1DG} and D_{1DG}, and by the 1D analysis. Thus 1D Gaussian fitting is not enough accuracy to estimate in-plane strain.

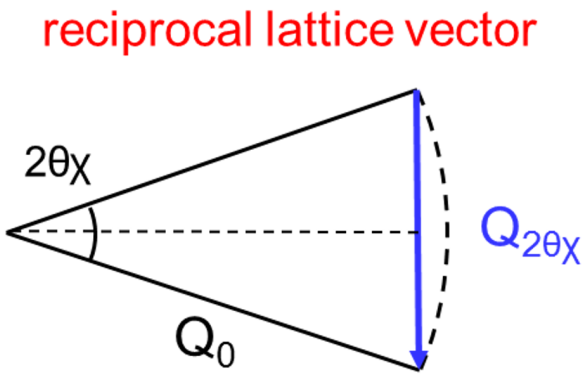

Fig. 2.17. The relationship between diffraction angle, $2\theta\chi/\phi$ and reciprocal lattice vector, $Q_{2\theta\chi/\phi}$.

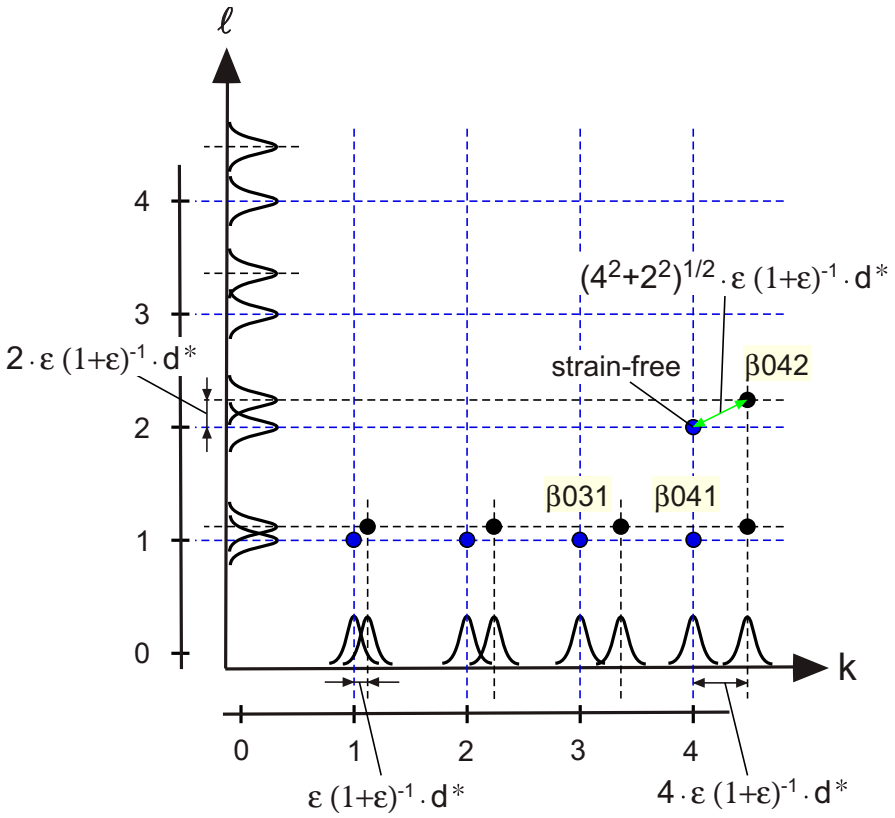

Fig. 2.18. The relationship of strain and the shift of peak center with each k and l in reciprocal space. The blue circles indicate the peak position in free-strain. When β-$FeSi_2$ nano-film has a certain domain in k-direction, the shift amount of peak center become bigger along with k number.

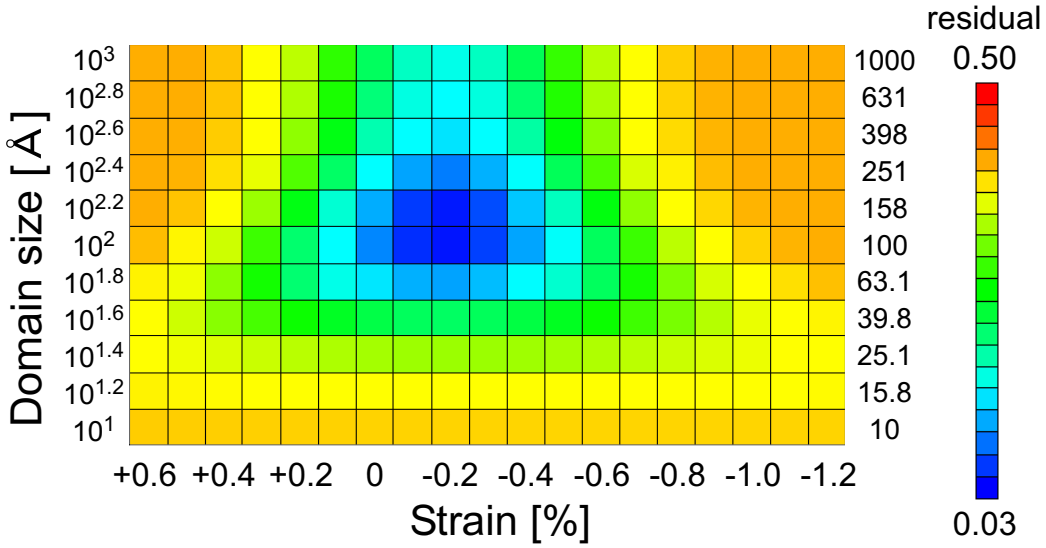

Fig. 2.19. The result of 1D Gaussian fitting with a certain domain size and strain.

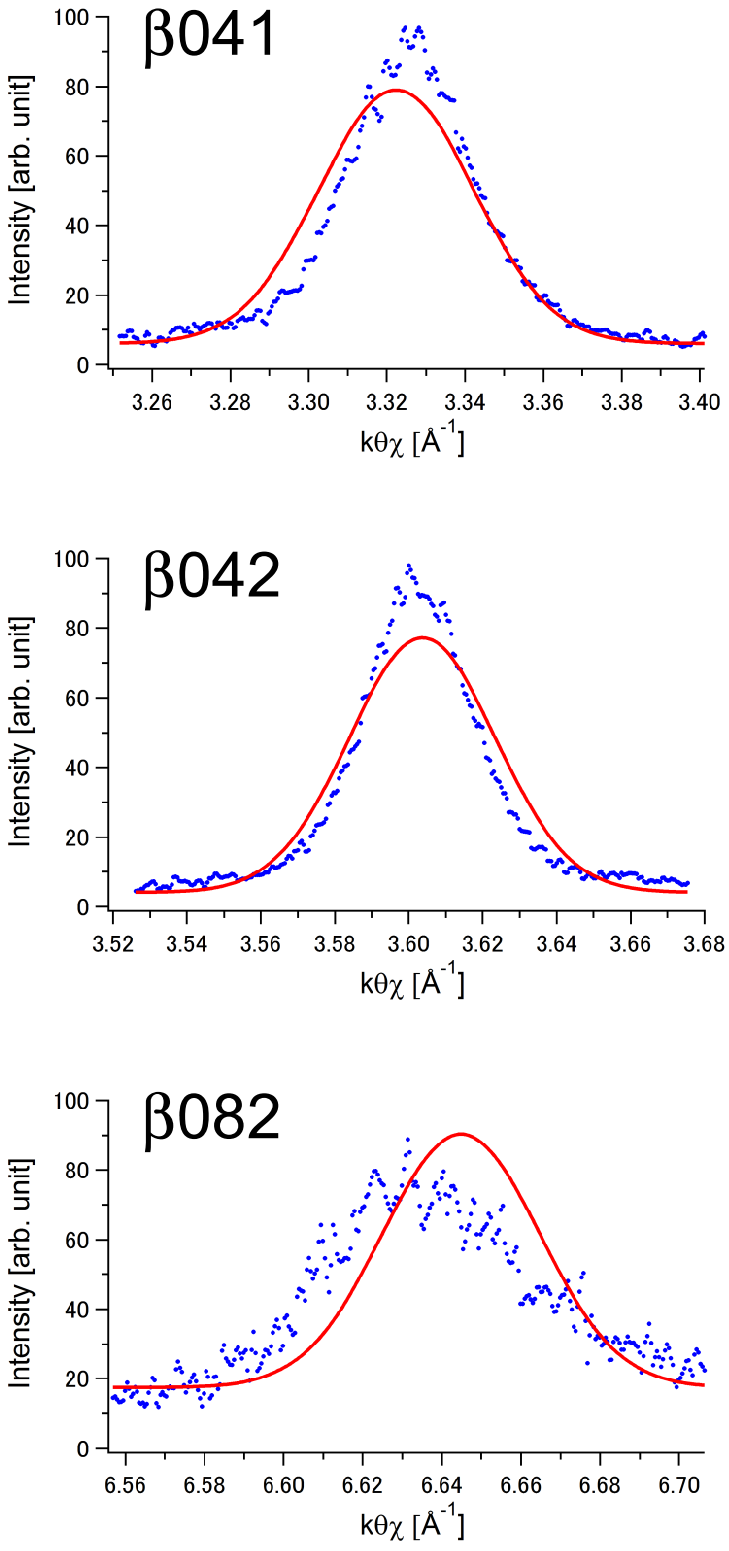

Fig. 2.20. The line profiles calculated from estimated strain (ϵ = -0.2 %) and domain size (D = 100 Å) in $2\theta\chi/\phi$ direction around β041 spot, β042 spot and β082 spot.

2.5.3 2D-Gaussian fitting analysis

In this section, we expand the 1D Gaussian analysis to the 2D Gaussian analysis for β-$FeSi_2$041, 042, and 082 reflections in 2D RSM (Fig. 2.13(a)–(c)). Figure 2.21 shows the 3D view of 2D RSM results. The measured peak shapes have 2D peak broadening and include the instrument component. To correct 2D instrumental broadening, RSMs of Si220 and Si$\bar{2}$20 are measured (Fig. 2.22(a)). The peak broadening of instrument is perfect circle ideally. Actually, the peak broadening of instrument has extended broadening along radial direction. This instrument broadening was fitted to the 2D Gaussian function with the long axis (the standard deviation $\sigma_{inst-2\theta\chi}$ ~0.0085 Å^{-1}) along the radial direction and the short axis (the standard deviation $\sigma_{inst-\phi} \sim 0.0042$ Å^{-1}) perpendicular to the radial direction (Fig. 2.22(a)). The intensity profile along the short axis seems to be the profile in ϕ scan, but it is not the same because the trajectory of the ϕ scan is an arc in 2D-RSM.

Similar to the 1D Gaussian analysis, we assume the averaged in-plane lattice constant d, and the same strain ϵ_{2DG} and domain size D_{2DG} for b and c directions. The intensity of the 2D Gaussian fitting function for β-$FeSi_2$0kl reflection in 2D-RSM (Q_x, Q_y) can be written as,

$$I^{0kl}_{2DG-fit}(Q_x, Q_y; \epsilon_{2DG}, D_{2DG}) = I_{bg} + I_{peak} \cdot$$
$$\exp\Big[-\frac{(\Delta Q_x \cos\phi^{0kl} + \Delta Q_y \sin\phi^{0kl})^2}{\sigma^2_{inst-2\theta\chi} + (\frac{2\pi}{2\sqrt{2\ln 2}D_{2DG}})^2} - \frac{(-\Delta Q_x \sin\phi^{0kl} + \Delta Q_y \cos\phi^{0kl})^2}{\sigma^2_{inst-\phi} + (\frac{2\pi}{2\sqrt{2\ln 2}D_{2DG}})^2}\Big]. \quad (8)$$

Here $(\Delta Q_x, \Delta Q_y)$ are difference of (Q_x, Q_y) from the peak center $(k, l)(1+\epsilon_{1DG})^{-1}d^*$. $phi^{0kl} = \tan^{-1}\frac{l}{k}$ is the azimuth angle of the peak center; $phi^{041} = 14.0°$, $phi^{042} = 26.6°$, and $phi^{082} = 14.0°$. The coefficient of D_{2DG}, $2\sqrt{2\ln 2}$, is the conversion factor from FWHM ($2\pi/D_{2DG}$ in Laue function) to the standard deviation in Gaussian.

Using $I^{0kl}_{2DG-fit}(Q_x, Q_y; \epsilon_{2DG}, D_{2DG})$, the squared residual R^{0kl}_{2DG} is described as,

$$R^{0kl}_{2DG}(Q_x, Q_y; \epsilon_{2DG}, D_{2DG}) = \frac{\sum_{Q_x}\sum_{Q_y}\{I^{0kl}_{2DG-exp}(Q_x, Q_y) - I^{0kl}_{2DG-fit}(Q_x, Q_y; \epsilon_{2DG}, D_{2DG})\}^2}{\sum_{Q_x}\sum_{Q_y}\{I^{0kl}_{2DG-exp}(Q_x, Q_y)\}^2}, \tag{9}$$

and the total squared residual R_{2DG} is,

$$R_{2DG}(\epsilon_{2DG}, D_{2DG}) = \sum_{041,042,082} W^{0kl} \cdot R^{0kl}_{2DG}(\epsilon_{2DG}, D_{2DG}). \tag{10}$$

Fig. 2.23(d) shows R_{2DG} map as a function of ϵ_{2DG} (from -1.2 to +0.6 %) and D_{2DG} (from 10^1 to 10^3 Å). The minimum of R_{2DG} was $R_{2DG-min} = 3.5\times10^{-2}$ at ϵ_{2DG} = -0.2 % and D_{2DG} = 160 Å; the $R_{2DG-min}$ value is ∼10%-smaller than $R_{1DG-min}$. The R_{2DG} map also shows that the error range of the domain size (blue region, $D_{2DG} \approx$ 100–250 Å at ϵ_{2DG} = -0.2 %) became narrower than the R_{1DG} map ($D_{1DG} \approx$ 63–250 Å at ϵ_{1DG} = -0.2 %). These imply the accuracy advantage of the 2D Gaussian fitting compared with the 1D Gaussian fitting. So far, similar approach to find a certain strain by minimalizing the residual between an experimental and simulated 2D RSM has been reported for nano wire by Durand [10]. They estimated the anisotropic strain for x and z direction from. The difference from this method was that they used the FEM simulation to generate the 4000 RSMs with various of strain. And another difference was that they included the wire structure in simulation, so they did not need to consider domain size distribution. On the other hand, our method has advantage of using 3 spots in calculation. The simulated reflection peak profiles at the residual minimum are shown in Figs. 2.24(a)–2.24(c). We notice that the simulated peak shapes are circle-like while the experimental peak ones are oval-like, in addition to the peak position difference in

the 082 reflection. Such still remaining discrepancies would be caused by the assumptions of d, ϵ_{2DG} and D_{2DG}. We expect much more improvement of the reliability when we simulate realistic models instead of the simple Gaussian fittings.

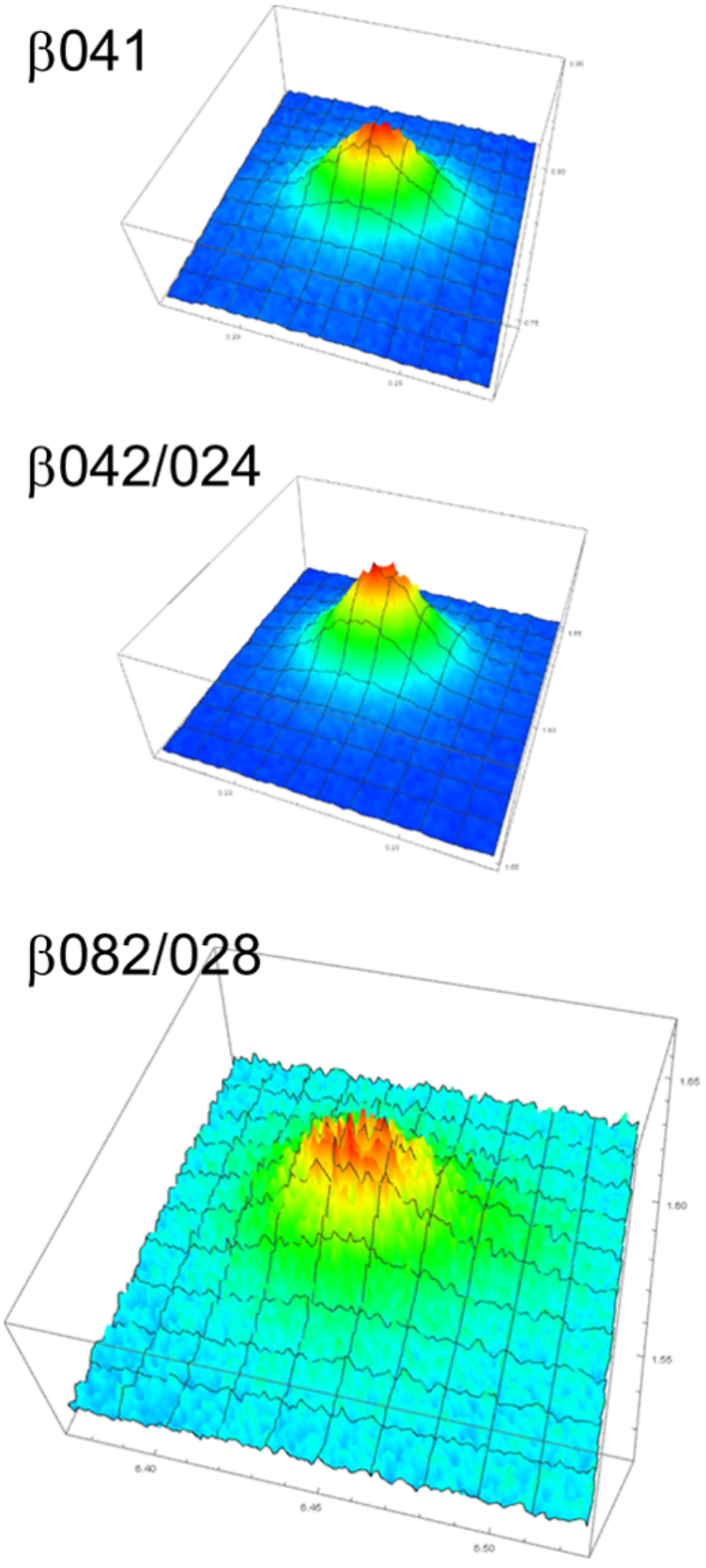

Fig. 2.21. The 3D views of RSM results.

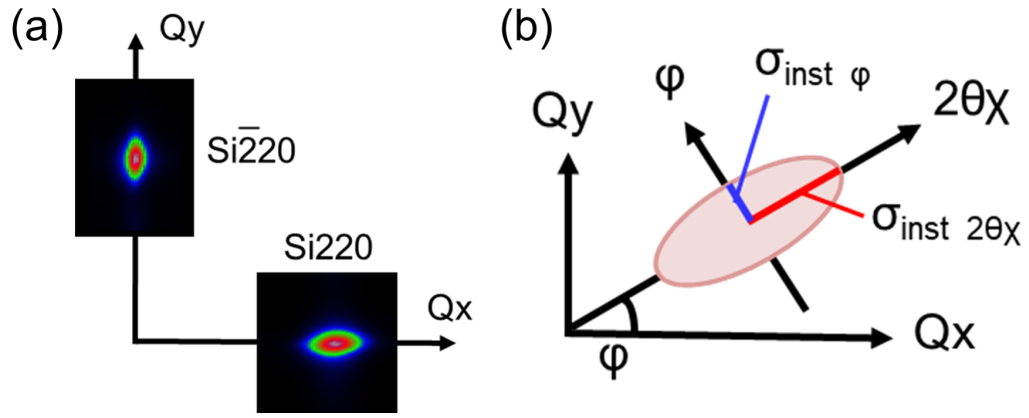

Fig. 2.22. (a) The results of RSM around Si$\bar{2}$20 and Si220 spot. (b) The schematic diagram of peak shapes derived from instrument with different length.

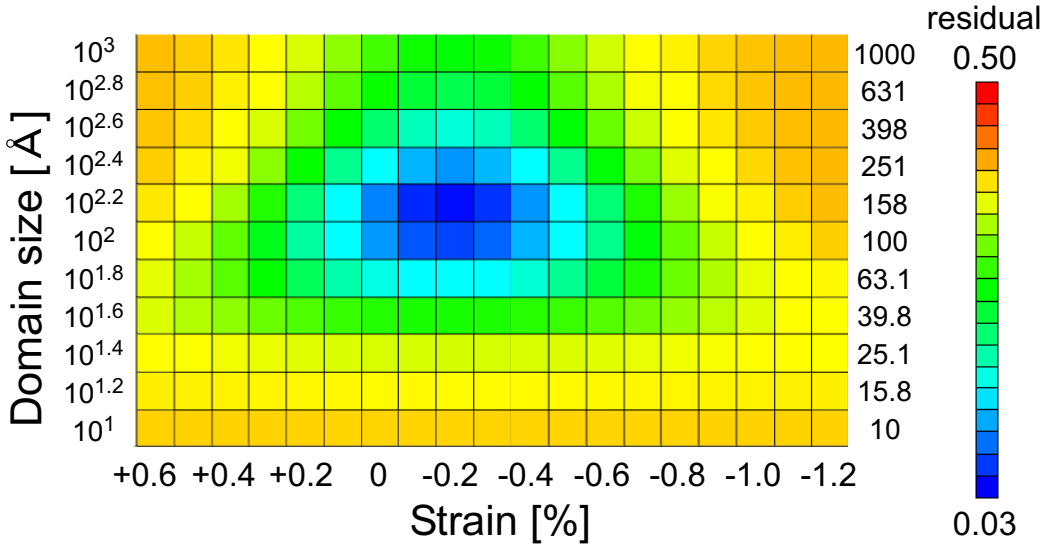

Fig. 2.23. The result of 2D Gaussian fitting with a certain domain size and strain.

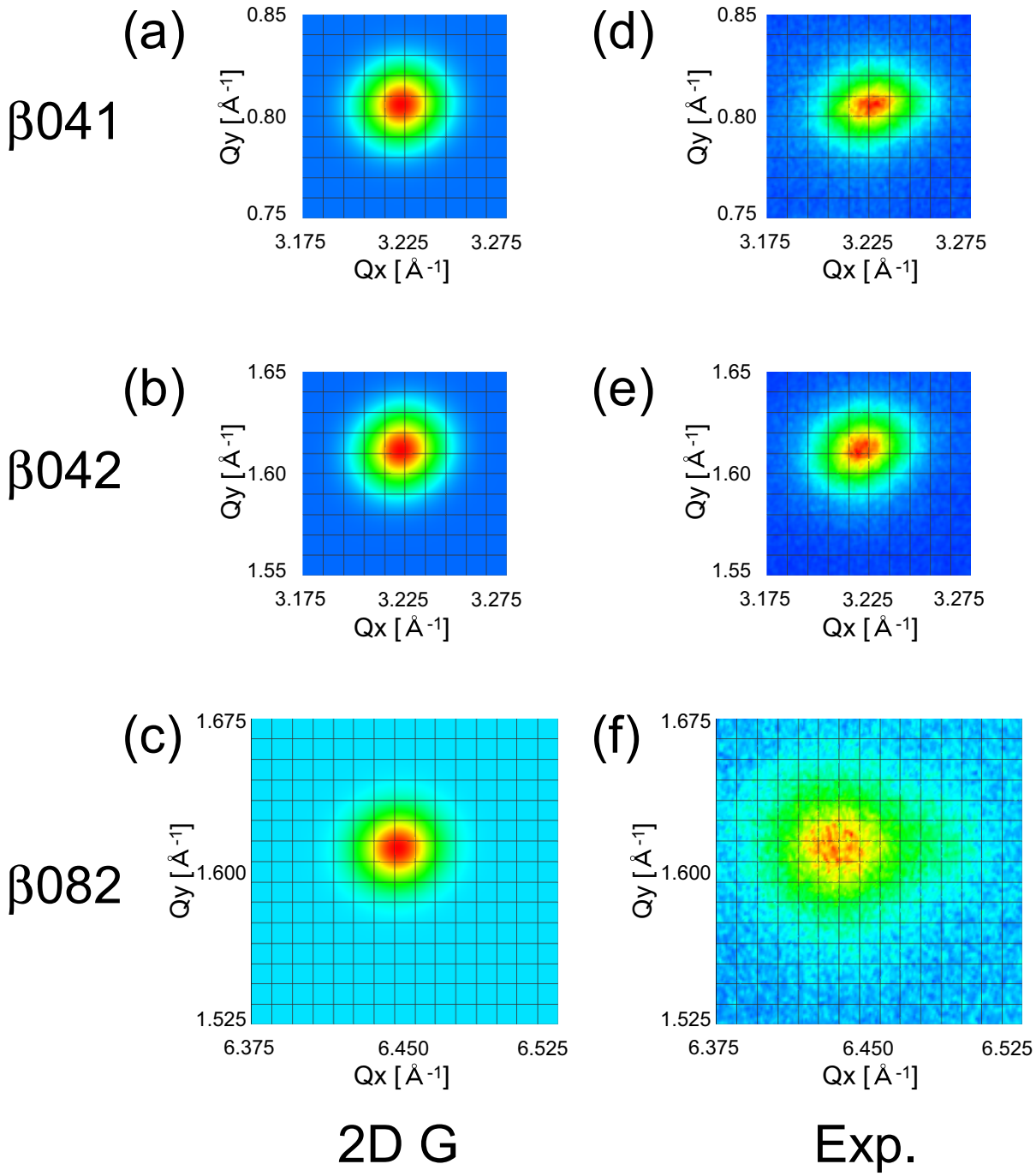

Fig. 2.24. (a)–(c) The calculated spot shapes of β041, β042 and β082 spots with estimated strain (ϵ = -0.2 %) and domain size (D = 125 Å) by 2D Gaussian fitting. (d)–(f) The the result of RSM around β041, β042, β082 spot in same region by in-plane XRD measurement.

2.5.4 2D anisotropic strain analysis

The Gaussian fitting analysis has a certain accuracy because of the simple assumption of isotropic strain. To improve of analysis method, anisotropic strain is considered in this analysis method. β-$FeSi_2$ single-crystalline nano film is epitaxially grown on Si(001) substrate with β-$FeSi_2[010] \parallel Si\langle 110\rangle$ (Romanyuk, 2014). Since Si(001) has a double-domain surface structure, β-$FeSi_2(100)$ stacking is also double domain: domain A with b in x (Si[110]) and c in y (Si[$\bar{1}$10]) directions, and domain B with c in x and b in y directions. The occupation of domains A and B should be the same.

The Laue function determining reflection peak shapes for domain A with anisotropic strain ϵ_b (ϵ_c) and unit number N_b (N_c) in b (c) axis is described as,

$$L_{2DL-A}(Q_x, Q_y : \epsilon_b, \epsilon_c) = \Big| \frac{1}{N_b N_c} \sum_{n_b=1}^{N_b} \sum_{n_c=1}^{N_c} \exp\Big(-i(Q_x n_b(1+\epsilon_b)b + Q_y n_c(1+\epsilon_c)c)\Big)\Big|^2. \quad (11)$$

Here we assume $N_b = N_c = 30 (\sim 230\,\text{Å})$ from the STM results (Fig. 1.3). This value is a close of Gaussian fitting result ($100 \sim 160\,\text{Å}$). (Q_x, Q_y) is 2D reciprocal space position before the instrument broadening of $\sigma_{inst-2\theta\chi}$ along the radial direction and $\sigma_{inst-\phi}$ perpendicular to the radial direction. The convolution of the Laue function with the instrument broadening is written as,

$$LC_{2DL-A-fit}(Q_x, Q_y : \epsilon_b, \epsilon_c) = L_{2DL-A}(k_x, k_y : \epsilon_b, \epsilon_c) * G_{inst}(Q_x - k_x, Q_y - k_y) \quad (12)$$

$$= \int dk_x \int dk_y L_{2DL-A}(Q_x, Q_y : \epsilon_b, \epsilon_c) \exp\Big(-\frac{\Delta Q_2 \theta\chi^2}{\sigma^2_{inst-2\theta\chi}} - \frac{\Delta Q^2_\phi}{\sigma^2_{inst-\phi}}\Big), \quad (13)$$

where

$$\begin{bmatrix} \Delta Q_r \\ \Delta Q_\phi \end{bmatrix} = \begin{bmatrix} \cos\phi & \sin\phi \\ -\sin\phi & \cos\phi \end{bmatrix} \begin{bmatrix} Q_x - Q_x \\ q_y - k_y \end{bmatrix}, \ \phi = \tan^{-1}\frac{k_y}{k_x}. \tag{14}$$

The exchange of b and c in Eqs. 11 and 13 corresponds the Laue function L_{2DL-B} and the Laue convolution $LC_{2DL-B-fit}$, respectively, for domain B.

The double-domain β-$FeSi_2$(100) implies that, for instance, 042 spot in 2D RSM corresponds to two near reflections: 042 reflection of domain A, namely 042-A, and 024 reflection of domain B, namely 024-B. We assumed that the weight of 042-A and 024-B is equal weight and weight of 042 and 041 is also equal weight which was estimated from noise-to-signal ratio of measured peak intensities. The weight of 042-A and 024-B is determined by their reflection intensity from the structural factor: $w^{042-A} = 7.3$ and $w^{024-B} = 12.1$. Similarly $w^{041-A} = 29.9$, and $w^{014-B} = 0$ (extinction). [1] Thus, the squared residual for $0kl$ spot is described as,

$$\begin{aligned} R^{0kl}_{2DLC}(\epsilon_b, \epsilon_c) = \frac{W^{0kl}_{S/N}}{\sum_{Q_x}\sum_{Q_y}\{I^{0kl}_{2D-exp}(Q_x, Q_y)\}^2} \cdot \sum_{Q_x}\sum_{Q_y}\Big\{ & I^{0kl}_{2D-exp}(Q_x, Q_y) \\ -I^{0kl}_{bg} - I^{0kl}_{peak}\frac{w^{0kl-A}}{(w^{0kl-A} + w^{0lk-B})} & LC^{0kl}_{2DL-A-fit}(Q_x, Q_y; \epsilon_b, \epsilon_c) \\ -I^{0kl}_{peak}\frac{w^{0kl-B}}{(w^{0kl-A} + w^{0lk-B})} & LC^{0lk}_{2DL-B-fit}(Q_x, Q_y; \epsilon_b, \epsilon_c)\Big\}^2, \end{aligned} \tag{15}$$

and the total squared residual is,

$$R_{2DLC}(\epsilon_b, \epsilon_c) = \sum_{041,042} R^{0kl}_{2DLC}(\epsilon_b, \epsilon_c). \tag{16}$$

[1] Note that 041 spot only corresponds to 041-A reflection.

Fig. 2.25(a) shows R_{2DLC} map as a function of ϵ_b and ϵ_c (from -1.2 to +0.6%). The minimum of R_{2DLC} was $R_{2DLC-min} = 1.1\times10^{-2}$ at $\epsilon_b \approx 0.0\%$ and $\epsilon_c \approx$ -0.3%. The $R_{2DLC-min}$ value is smaller than that of $R_{2DG-min}$ (3.5×10^{-2}) in the 2D Gaussian fitting, implying that the evaluation of considerably accurate strains was achieved. Indeed, the simulated peak shapes with estimated strain ($\epsilon_b = 0.0\%$, $\epsilon_c = -0.3\%$) became mostly identical to the oval-like experimental shapes, in contrast to circle-like shapes in the 2D Gaussian simulation (Fig. 2.25(b)–(c)).

The result of 2D anisotropic strain model shows that the possible ϵ_b and ϵ_c values can be easily recognized as the blue region in the R_{2DLC} map (Fig. 2.25(a)); the residual valley elongates to the upper left from (ϵ_b, ϵ_c) = (0.0%, -0.2%) to (+0.1%, -0.1%) in the map with $\pm0.1\%$ at $1.1/, R_{2DLC-min}$ surrounded by solid lines. [2] The valley elongation implies the conservation of surface unit area $(1+\epsilon_b)(1+\epsilon_c)/, b/, c$ with an anisotropic strain. According to show the elongated peak shape calculated by the estimated strain, the accuracy of analysis is improved. Then strain distribution is considered as final step of analysis.

[2]Note that the line width of the Cu K_α wavelength corresponding to 0.2% in error could contribute to the ϵ_b and ϵ_c errors.

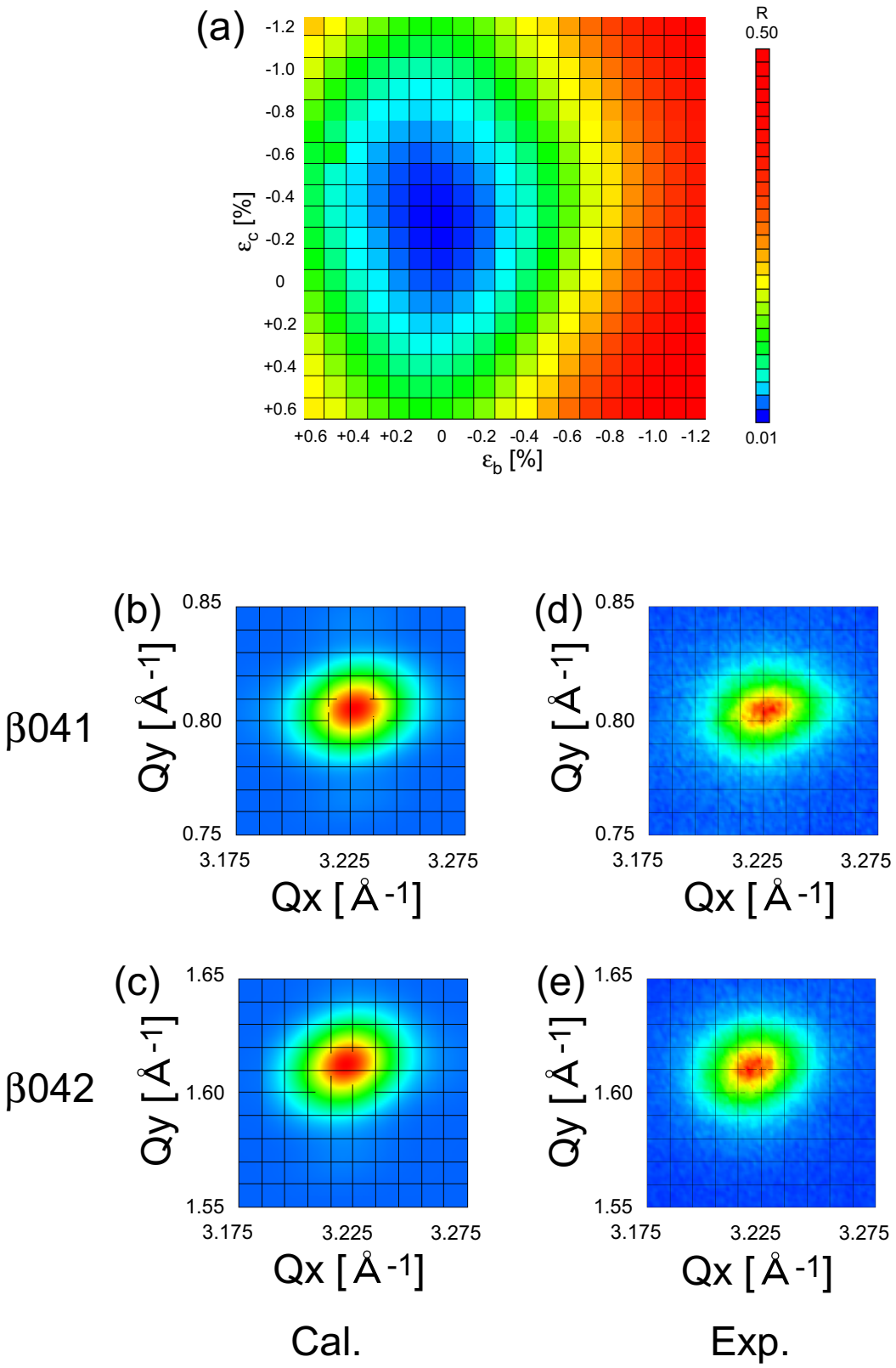

Fig. 2.25. (a) R_{2DLC} map as a function of ϵ_b and ϵ_c (from -1.2 to +0.6%). (b)–(c) The calculated spot shapes of $\beta 041$ and $\beta 042$ spots with estimated strain ($\epsilon_b = 0.0\%$, $\epsilon_c = -0.2\%$). (d)–(e) The the result of RSM around $\beta 041$ and $\beta 042$, spot in same region by in-plane XRD measurement

2.5.5 2D strain distribution analysis

The residual R_{2DLC} map (Fig. 2.25) displays the reliability for the restricted case where all domains have a homogenous strain. In this section, we analyze inhomogeneous strain distribution where different domains have different strains, though the W-H analysis using the same reflection spots had a little accuracy in strain broadening (0.48%). The concept of strain distribution analysis is shown in Fig. 2.26. The peak shape of in-plane XRD reflects average information in irradiation region of X-ray. It is difficult to estimate strain distribution from the experimental result. Here, irradiation region of X-ray was separated into many domains and each domain has a certain strain in b and c axes. The diffraction intensity can be represented by the superposition in multi-domains. Then in-plane strain distribution is estimated by the comparison between experimental and simulated peak shapes. When coherent region is smaller than homogenous domain size, the fitting by the superposition of differently-strained reflection profiles is possible as described in introduction part. The spatial (transverse) coherence length ∼6 nm from 0.5 deg, time (longitudinal) coherence length ∼50 nm from $\lambda^2/\Delta\lambda$ where $\lambda = (2 * 1.5406 + 1 * 1.5444)/3 = 1.5418$ Å, $\Delta\lambda = 1.5444 - 1.5406 = 0.004$ Å calculated from the equipment specification. If the spatial coherent length is 6 nm, the instrumental peak broadening should become wider. And If time coherence length is also 50 nm, interference of two domains in excessive meddling region should be considered because the each domain of nano-carpet is very close. Here, I assumed the coherent length ∼220 Åestimated the from instrumental peak broadening σ_{inst} ∼0.017 Å. Then the strain distribution, that is, the weight of a certain strain $\omega(\epsilon_b, \epsilon_c)$ can be found when ω distribution minimizes the

following R_{2DLCD}.

$$R_{2DLCD} = \sum_{041,042} R^{0kl}_{2DLCD}(\epsilon_b, \epsilon_c), \tag{17}$$

where

$$R^{0kl}_{2DLCD}(\epsilon_b, \epsilon_c) = \frac{W^{0kl}_{S/N}}{\sum_{Q_x}\sum_{Q_y}\{I^{0kl}_{2D-exp}(Q_x, Q_y)\}^2} \cdot \sum_{Q_x}\sum_{Q_y}\Big\{ I^{0kl}_{2D-exp}(Q_x, Q_y) - I^{0kl}_{bg} - I^{0kl}_{peak}\sum_{\epsilon_b}\sum_{\epsilon_c}\omega(\epsilon_b, \epsilon_c) LC^{0kl}_{2DL-A\&B-fit}(Q_x, Q_y; \epsilon_b, \epsilon_c)\Big\}^2, \tag{18}$$

and

$$LC^{0kl}_{2DL-A\&B-fit}(Q_x, Q_y; \epsilon_b, \epsilon_c) = w^{0kl-A}/(w^{0kl-A} + w^{0lk-B}) LC^{0kl}_{2DL-A-fit}(Q_x, Q_y; \epsilon_b, \epsilon_c) + w^{0lk-B}/(w^{0kl-A} + w^{0lk-B}) LC^{0lk}_{2DL-B-fit}(Q_x, Q_y; \epsilon_b, \epsilon_c). \tag{19}$$

Fig. 2.27(a) shows inhomogeneous strain distribution of (ϵ_b, ϵ_c) in the range of -1.2$\sim$+ 0.6 % with 0.1 % step when minimalizing R_{2DLCD} to 8.4×10^{-3}. ($\sqrt{R_{2DLCDmin}} = 2.9 \times 10^{-2}$) The minimum R_{2DLCD} is slightly better than $R_{2DLC-min}$ (1.1×10^{-2}) of the homogeneous domain with $\epsilon_b \approx$ 0.0 % and $\epsilon_c \approx$ -0.3 %. Highly weight part in Fig. 2.27 is displayed by red color; the highest (second and third highest) weight was 47.3 % (18.0 and 11.5 %) of the total at ϵ_b = 0.0 % (+0.1 and +0.5 %) and ϵ_c= -0.3 % (-0.3 and -0.6 %). These closest (ϵ_b, ϵ_c) pairs occupies 65 % (Indeed, the simulated peak shapes in Fig. 2.27(b)–(c) resemble to the experiment ones as those of 2DLC-min in Fig. 2.25(b)–(c). I considered the result of strain distribution. The majority strain is ϵ_b = 0.0 % and ϵ_c = -0.3 %, which is quite smaller than the lattice mismatch between β-$FeSi_2$ and Si substrate (-1.4 % in b axis and -2.0 % in c axis).

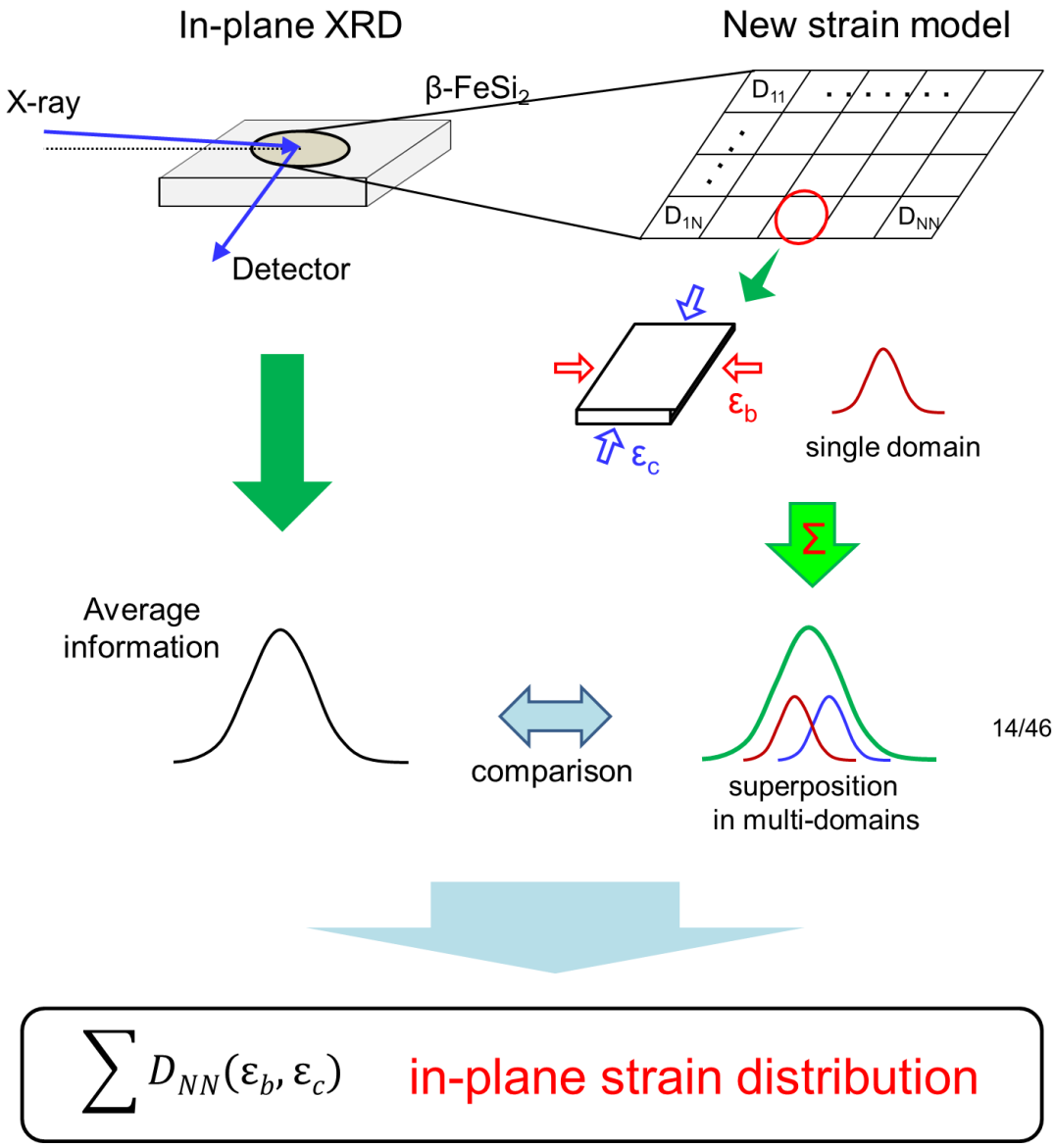

Fig. 2.26. The concept of strain distribution analysis.

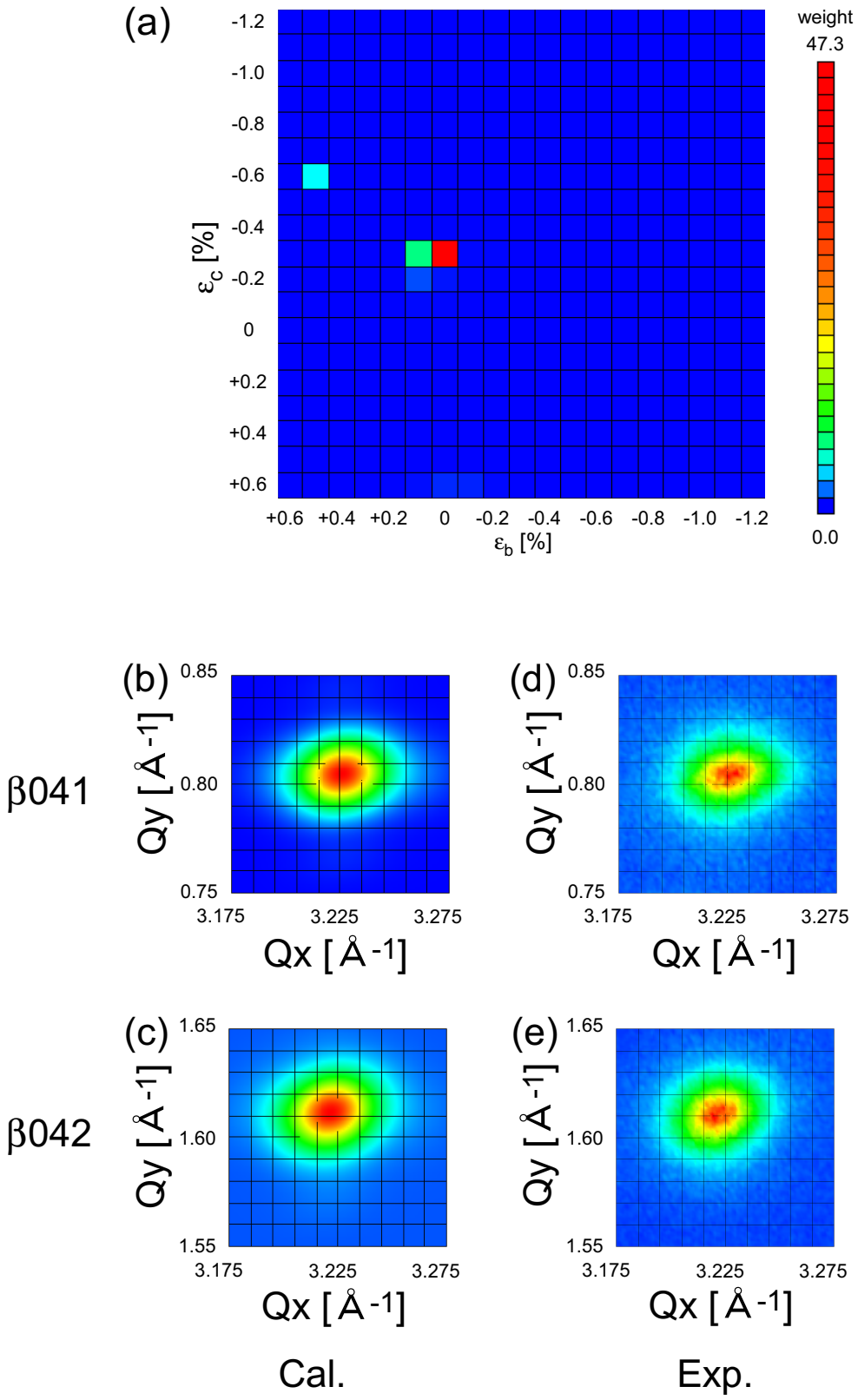

Fig. 2.27. (a) strain distribution (weight) map as a function of ϵ_b and ϵ_c (from -1.2 to +0.6%). (b)–(c) The calculated spot shapes of $\beta 041$ and $\beta 042$ spots with estimated strain and weight. (d)–(e) The the result of RSM around $\beta 041$ and $\beta 042$ spot in same region by in-plane XRD measurement

2.6 Discussion

I summarized the result of each analysis method in this section. In the classical methods (Scherrer method and Williamson-Hall method), the usual peak-center and broadening analysis resulting in $\epsilon \approx$ -0.07%, $D_{Sch} \approx$ 100–230 Å, $\Delta\epsilon \approx 0.48\%$, and $D_{W-H} \approx$ -1,100 Å had a little accuracy in our system. The estimated strain and domain size in 1D Gaussian fitting was described that ϵ_{1DG} and D_{1DG} were -0.3 $\sim$ -0.1% and 60 $\sim$ 160 Å, respectively. There were discrepancies between the experimental and fitted intensities. The minimum of R_{1DG} was $R_{1DG-min} = 3.9\times10^{-2}$. In 2D Gaussian fitting, the estimated strain (ϵ_{2DG}) and domain size (D_{2DG}) are -0.3 $\sim$ -0.1% and 100 $\sim$ 250 Å. The minimum of R_{2DG} was $R_{2DG-min} = 3.5\times10^{-2}$ The error range became narrower than 1D Gaussian fitting. These imply the accuracy advantage of the 2D Gaussian fitting compared with the 1D Gaussian fitting. However, the simulated peak shapes are circle-like while the experimental peak ones are oval-like, in addition to the peak position difference in the 082 reflection. This is a limit of Gaussian fitting with simple assumption of isotropic strain. The possible ϵ_b and ϵ_c values can be easily recognized as the blue region in the R_{2DLC} map (Fig. 2.25(a)); the residual valley elongates to the upper left from (ϵ_b, ϵ_c) = (0.0%, -0.2%) to (+0.1%, -0.1%) in the map with $\pm$0.1% at $1.1/, R_{2DLC-min}$. The minimum of R_{2DLC} was $R_{2DLC-min} = 1.1\times10^{-2}$ According to show the elongated peak shape calculated by the estimated strain, the accuracy of analysis is improved. In the strain distribution method, the minimum R_{2DLCD} (8.4×10^{-3}) is slightly better than $R_{2DLC-min}$ (1.1×10^{-2}) of the homogeneous domain with $\epsilon_b \approx 0.0\,\%$ and $\epsilon_c \approx$ -0.3 %. Highly weight part in Fig. 2.27 is displayed by red color; the highest (second and third highest) weight was 47.3 % (18.0 and 11.5 %) of the total at $\epsilon_b = 0.0\,\%(+0.0 and +0.5\,\%)$

and $\epsilon_c = -0.3\,\%(-0.3 and -0.6\,\%)$. Indeed, the simulated peak shapes in Fig. 2.27(b)–(c) resemble to the experiment ones as those of 2DLC-min in Fig. 2.25(b)–(c).

Figure 2.28 and 2.29 shows the line-profile of calculated spots in k$\theta\chi$ and kϕ direction in each analysis. Blue dots show the result of XRD measurement. The simulated results of the estimated strain are described as red line. It was found that the simulated line-profiles have good reproducibility as the improvement of residual.

The estimated strain is quite smaller than the lattice mismatch between β-$FeSi_2$ and Si substrate (-1.4 % in b axis and -2.0 % in c axis). The strain distribution is also very narrow. These results mean the combination of β-$FeSi_2$ nano-carpet with Si substrate is weak, that is, β-$FeSi_2$ nano-carpet is state of floating on Si substrate. Another consideration is about anisotropic strain (ϵ_b = +0.1 %, ϵ_c = -0.3 %) estimated by strain distribution analysis. The error of strain(absolute value) is $\sim$ 0.26 % calculated from the equipment specification (without Ge monochromator). However, the anisotropy of strain(relative value) is not changed. The lattice constant of bulk β-$FeSi_2$ is b = 7.791 Å and c = 7.833 Å. Considering the estimated anisotropic strain, the lattice constant of β-$FeSi_2$ nano-carpet is calculated to b = 7.80 Å and c = 7.81 Å. Thus the in-plane unit cell of β-$FeSi_2$ is deformed to approximate square lattice. This tendency corresponds to the result of DFT calculation in Tanimoto's master thesis [13].

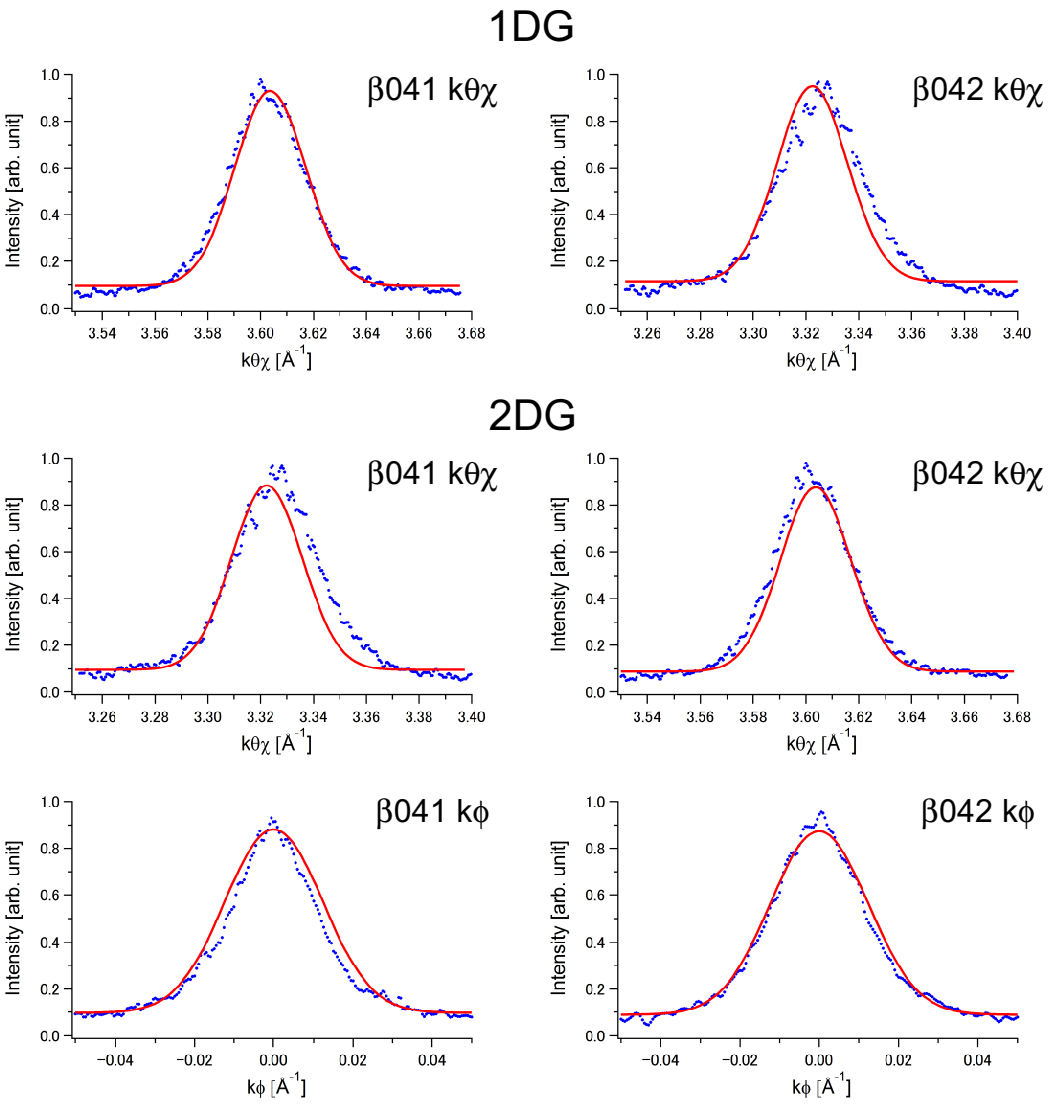

Fig. 2.28. The line-profile of calculated spots in k$\theta\chi$ and kϕ direction in 1DG and 2DG analyses.

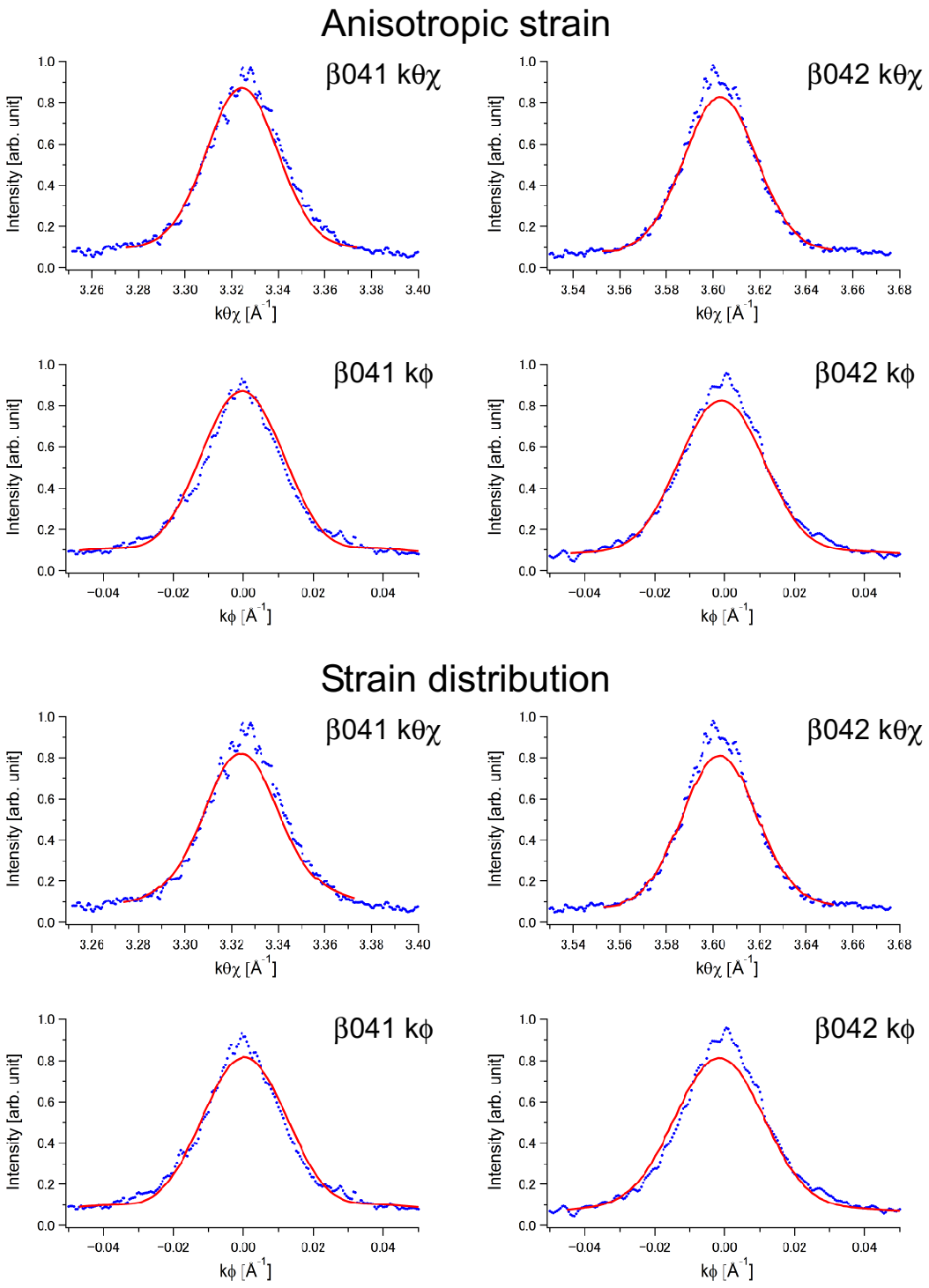

Fig. 2.29. The line-profile of calculated spots in k$\theta\chi$ and kϕ direction in 2D anisotropic strain and 2D strain distribution analyses.

2.7 Conclusion

The estimation in-plane strain for β-$FeSi_2$(100) nano-film by applying various of general analysis method, which is W-H method, 1D Gaussian fitting and 2D Gaussian fitting was performed. I found that W-H method is a little accuracy to estimate strain because of the less number of reflections. In Gaussian fitting methods a certain region of strain and domain size were estimated. The spot shapes calculated from estimated strain and domain size in Gaussian fitting were not reproduced as oval shape of experiment due to the assumption of isotropic strain and domain size. In a new analysis method, the fitting by the superposition of differently-strained reflection profiles using a probe beam with reduced coherent lengths when coherent region is smaller than homogenous domain size can be obtained the narrow distribution of strain than W-H method and anisotropic strain of highest weight. The strain distribution of β-$FeSi_2$(100) nano-film was estimated using a new analysis method with quite smaller residual sum of squares. This paper is the firstly analysis to estimate the strain distribution calculated from the spot shape of 2D-RSM in XRD measurement. As future development, the distribution of domain size will be considered. There is a limit of domain size distribution because of the relationship to the coherent length.

References

[1] G. K. Williamson and R. E. Smallman, Philos. Mag. **1**, 34 (1955).

[2] G. B. Mitra, Acta Cryst. **17**, 765 (1964).

[3] R. C. Garvie, J. Phys. Chem., **69**, 1238 (1965).

[4] R. Yogamalar, R. Srinivasan, A. Vinu, K. Ariga, and A. C. Bose, Sol. State Commun **149**, 1919 (2009).

[5] A. K, Zak, W. H. A. Majid, M. E. Abrishami, and R. Yousefi, Sol. State Commun **13**, 251 (2011).

[6] A. Monshi, M. R. Foroughi, and M. R. Monshi, World J. Nano Sci. Eng. 2 **2**, 154 (2012).

[7] A. Cervolino, C. Giannini, and A. Guagliardi, J. Appl. Cryst. **36**, 1148 (2003).

[8] A. S. Masadeh, E. S. Božin, C. L. Farrow, G. Paglia and S. J. L. Billinge, Phys. Rev. B **76**, 115413 (2007).

[9] T. Takeuchi, K. Tatsumura, T. Shimura, and I. Ohdomari, Thin Solid Films **612**, 116 (2016).

[10] A. Durand, M. Kaufling, D. Le-Cunff, D. Rouchoin, and P. Gergaund, Mater. Sci. Semicond. Process. **70**, 99 (2017).

[11] O. Romanyuk, M. Someta, K. hattori, and H. Daimon, Phys. Rev. B **90**, 155305 (2014).

[12] T. Takeuchi, K. Tatsumura, T. Shimura, and I. Ohdomari, J.Appl. Phys. **106**, 073506 (2009)

[13] K. Tanimoto, Master Thesis, NAIST (2018).

Chapter 3. Evaluation of surface atomic arrangement in 3D nano-fabricated materials

3.1 Introduction

Three-dimensional (3D) integrated circuits, which contain multiple layers of active devices, have the potential to dramatically enhance chip performance, functionality, and device packing density. 3D stacking techniques are inevitable for the continuous progress of scaling-down in Si device developments3.1. Recent 3D-structured field-effect transistors (FETs) have surfaces with different orientations; for instance, a fin-type tri-gate structure has one top-surface and two side-surfaces [1–3]. The electric connection between metal wires on these surfaces—that is, the wiring interconnects at sharp edges of top- and side-surfaces—is one of the issues for developing 3D devices. In other words, 3D angular-shape interconnects of wires at nanoscale with high performance is one of the important elements for the circuit-wiring techniques. The technique should be improved based on the knowledge of designing topologies and estimating performances for interconnects of metal wires on differently oriented 3D-surfaces depending on surface roughness, impurity, crystalline grain boundary, etc.

So far, metal films grown on two-dimensional (2D) planar-surfaces have been widely studied [4–6], and factors such as the roughness contributing to the conductivity degradation in the films have been revealed [7–10]. The first-step study for the conductivity performance in the 3D integrated circuits focused on the mobility on 2D side-surfaces perpendicular to the planner substrate-surfaces in 3D fabricated structures [11–20]. Mao *et al.* have reported the mobility degradation by the process-induced roughness on the side-surface of a Si nanowire,

and concluded that the improvement of side-surface quality is mandatory [11]. Similar phenomena were seen in GaAs-nanowire FET [12]. The mobility degradation due to the roughness has been demonstrated in simulations [13–20]. Though the conductivity in metal wires on isolated 2D planner- or side-surfaces has been well discussed, there are no reports for the metal conductivity interconnected between 3D surfaces with different orientations, probably owing to the difficulty of measuring the intrinsic conductivity in 3D angular-interconnects, which is mainly caused by the diffuse scattering at a rough surface [7–20]. Toward the next-step study for 3D stacked devices, metal electrodes grown on atomically-flat surfaces in 3D-structured substrates are required for the evaluation of the 3D interconnect resistivity by eliminating the extra factors, such as roughness.

Thus the roughness of side-surface influence the electric property of 3D structure. So far, there are no measurement method to observed side-surface directly. The roughness of side-surface was measured from top-surface as the projection (Fig. 3.2, 3.3). However, it is hard to evaluate the roughness of side-surface by indirect measurement. Recently 3D Si structures with arbitrarily-orientated side-surfaces and their atomically well-ordered surfaces have been successfully produced [21–23]. To our knowledge, they are the first reports for the creation of the 3D Si structure with atomically-ordered surfaces. Scanning tunneling microscopy (STM) have proven the atomically-ordered vertical side-surfaces in 3D space in addition to general 2D planar surfaces. However, STM can measure only a local surface structure. In this paper, to evaluate the atomically-ordered side-surfaces in widely region directly, I performed RHEED of a variety of 3D Si structures sample. Finally as next step, the resistance of Au wire on 3D atomically-ordered facet surface sample is measured to measure the intrinsic conductivity in 3D angular-interconnects (Fig. 3.4).

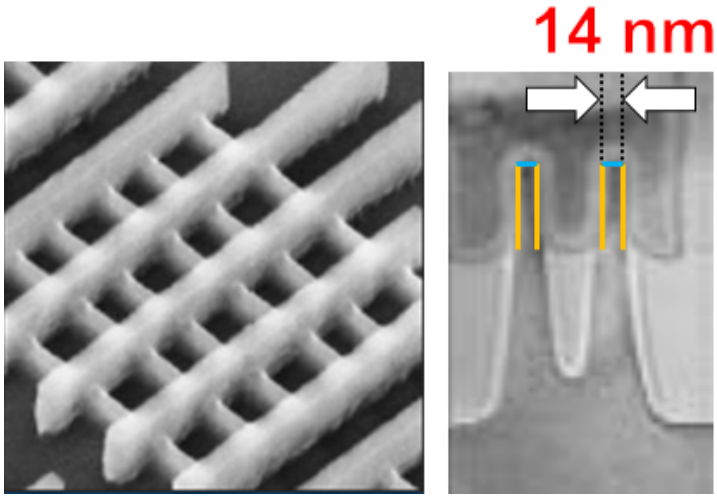

Fig. 3.1. The images of 3D-Fin-FET [24, 25].

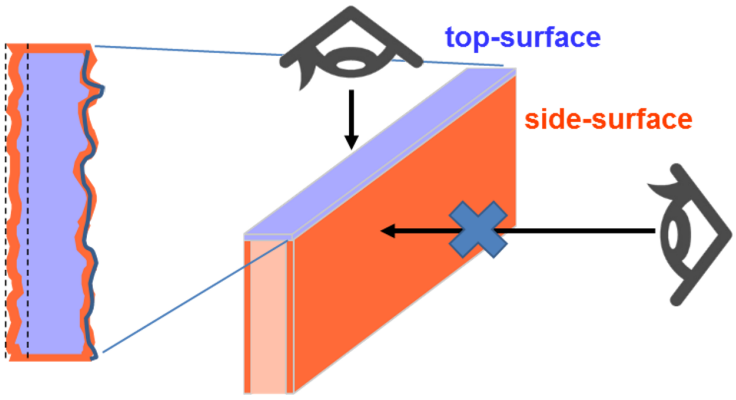

Fig. 3.2. The schematic diagram of a general evaluation method of side surface roughness.

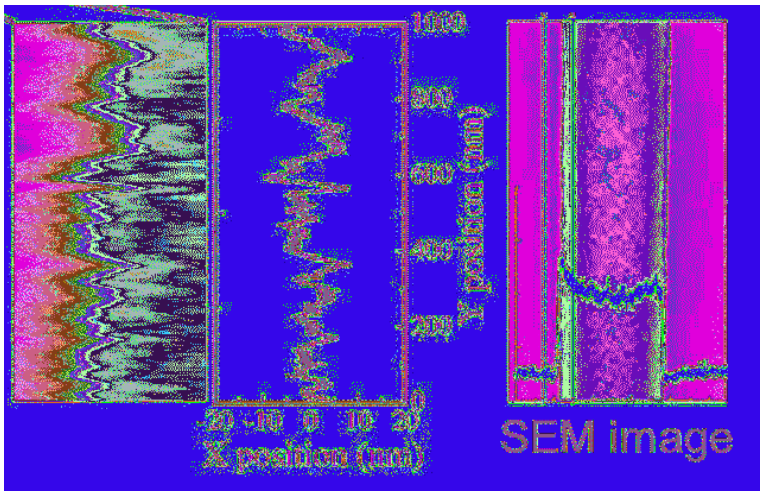

Fig. 3.3. SEM image of side-surface measured from top-surface direction and the roughness of side-surface evaluated from SEM image [26].

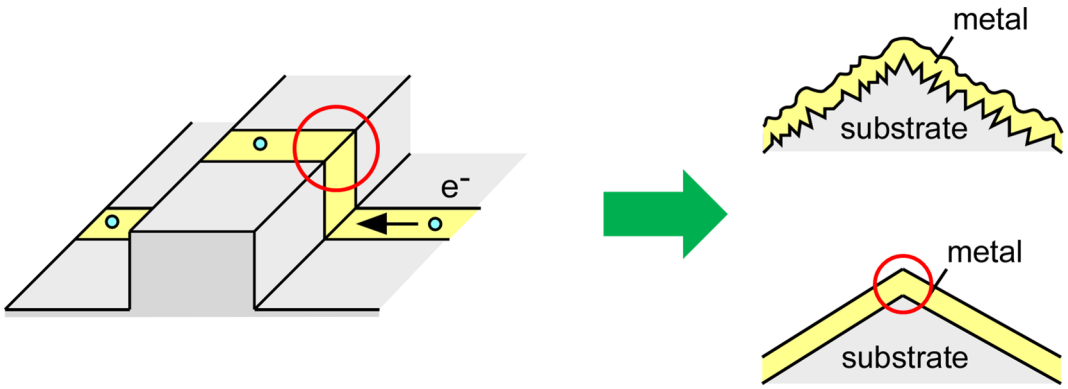

Fig. 3.4. Schematic diagram of electrode on 3D structure and the evaluation of connection at edge part.

3.2 Method and experiment

3.2.1 RHEED

In this section, the fundamental principles behind reflection high energy electron diffraction will be explained. The explanations are based mostly on the books Solid Surfaces and Reflection high energy electron diffraction by Ichimiya and Cohen [27], unless otherwise specified. RHEED is the most widely used experiments in structure determination of the surface. In RHEED, electrons with energies of 8-20 keV are used. The grazing incidence and detection angles used in the experiment means that the long mean-free path is associated with a penetration depth of only a few atomic layers normal to the surface. The high energies used in RHEED makes visualization of the diffraction patterns easier, where a simple fluorescent screen can be used. The fundamental principal of RHHED was described as follows. For an incident plane wave with wavelength, λ, interference will occur due to the path difference of waves scattered from different atoms. Constructive interference occurs when the path difference is an integer value of the wavelength. For a simple one-dimensional row of scatterers (3.5) with spacing a, the diffraction condition can be given as,

$$a\cos\theta_{out} - a\cos\theta_{in} = n\lambda. \tag{20}$$

Using the expression, $\frac{2\pi}{\lambda} = k$ and setting reciprocal lattice vector, $|\vec{G}| = \frac{2\pi n}{a}$, we rewrite eq. (20),

$$\begin{aligned} k\cos\theta_{out} - k\cos\theta_{in} &= n|\vec{G}| \\ (\vec{k_{out}} - \vec{k_{in}}) \cdot \vec{e_x} &= n\vec{G} \cdot \vec{e_x} \end{aligned} \tag{21}$$

This equation says that the parallel components of the incident and final wave vectors differ by an integral multiple of $2\pi/a$ of the reciprocal of the lattice spacing to satisfy the diffraction condition. Here, Ewald construction is often used for interpreting RHEED. In this approach, energy and momentum conservation are combined to describe the diffraction. The energy and momentum conservation require that

$$|\vec{k_{out}}| = |\vec{k_{in}}| \tag{22}$$

$$\vec{k_{out}} - \vec{k_{in}} = \vec{G_m} \tag{23}$$

The energy conservation in eq. (23) requires that the magnitude of the final wave vector $\vec{k_{out}}$ is constant equal to the incident wave vector $\vec{k_{out}}$. This will result in final wave vectors that can be described by a sphere, the Ewald sphere. In the required momentum conservation in eq. (23), the difference in the final and initial wave vectors should be equal to the 3D reciprocal lattice vector $\vec{G_m}$; the subscript m refers to the mth diffracted beam. The intersection of the Ewald sphere with reciprocal lattice points determine allowed diffraction conditions in Fig 3.6. The reciprocal lattice vector can be described as $\vec{G} = h\vec{a^*}$ considering to one-dimensional lattice. This equation says that reciprocal lattice indicates the planes with the spacing of $|\vec{a^*}|$

in kx direction as shown in Fig. 3.7 (a). Similarly, the reciprocal lattice from two-dimensional lattice can be described as $\vec{G} = h\vec{a^*} + k\vec{b^*}$, which indicates the rods with the spacing of $|\vec{a^*}|$ in kx direction and $|\vec{b^*}|$ in ky direction as shown in Fig. 3.7 (b). Figure 3.7 (c) shows the reciprocal lattice points from the three dimensional lattice. Graphically, one constructs a set of parallel rods normal to the surface, on points that correspond to the 2D reciprocal lattice points. The intersection of these rods with the Ewald sphere will correspond to allowed diffraction conditions, as shown in Fig. 3.8. The radius of Ewald sphere is calculated from the equation of energy of electron

$$E = \frac{\hbar^2 k^2}{2m}. \tag{24}$$

Here, $\hbar$ and m are Dirac's constant and the mass of electron, respectively. In this paper, the radius of Ewald sphere was calculated as follows when acceleration voltage set 15.00 kV.

$$\begin{aligned} k &= \frac{\sqrt{2mE}}{\hbar} \\ &= \frac{\sqrt{2 \times 9.110 \times 10^{-31}\,[kg] \times 15.00 \times 10^{3}\,[eV] \times (1.602 \times 10^{-19}\,[\frac{J}{eV}])}}{1.05459 \times 10^{-34}\,[J \cdot s]} \\ &= 62.74\,[\text{Å}^{-1}] \end{aligned} \tag{25}$$

In this paper, I try to observe RHEED pattern from side-surface by using 3D property of RHEED observation. Relationship between reciprocal lattice rods and Ewald's sphere diffracted from top- and side-surfaces is shown in Fig.3.9. In principal, It is possible to observe RHEED pattern from top- and side-surfaces simultaneously. Fig.3.10 shows the schematic diagram of simultaneous RHEED observation of top- and side-surfaces. For that purpose, the 3D structure sample such as in Fig.3.10 was prepared.

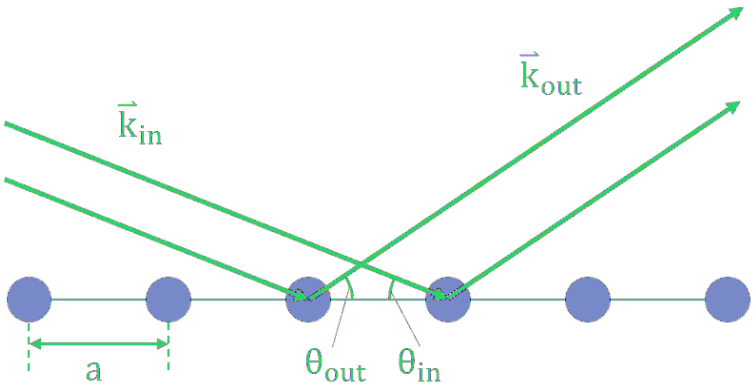

Fig. 3.5. a schematic drawing of the path difference due to scattering by two atoms in a one-dimensional row.

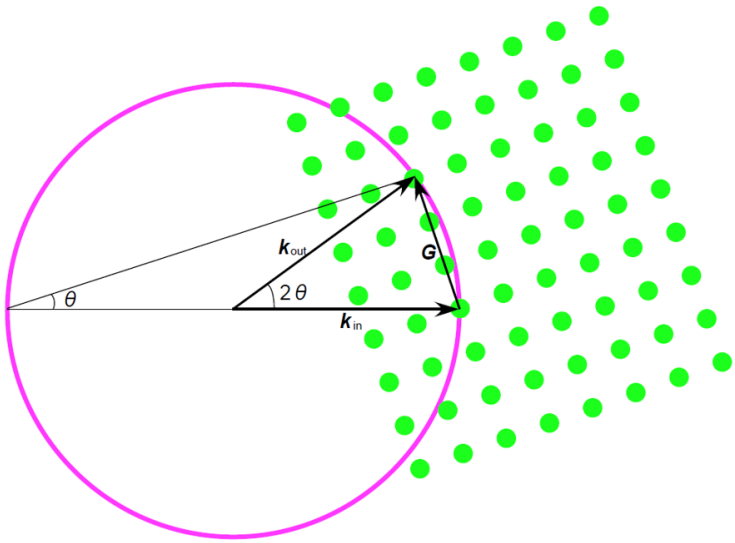

Fig. 3.6. Illustration of the diffraction condition, which was well known to Eward sphere.

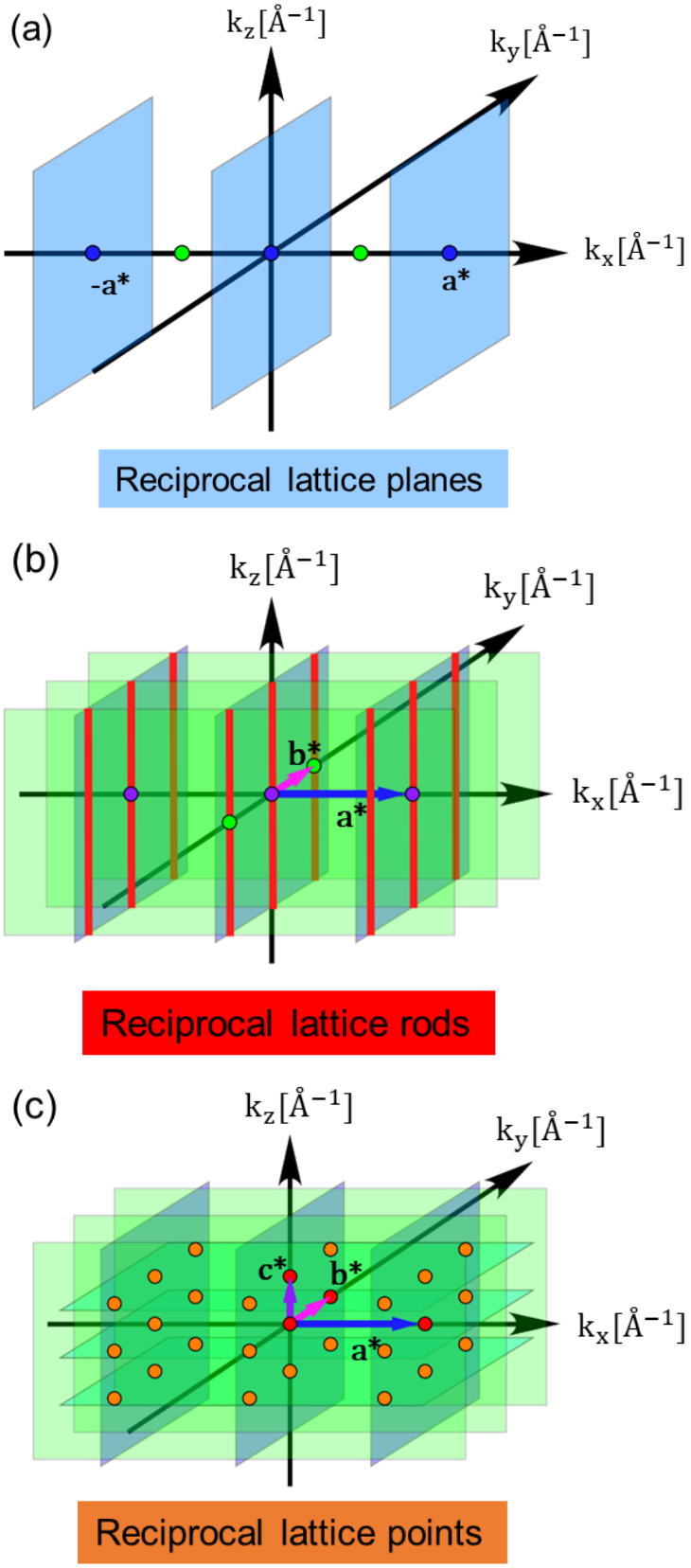

Fig. 3.7. Schematic drawing of reciprocal lattice scattered from one-dimensional lattice (a), from two-dimensional lattice (b), from three dimensional lattice (c).

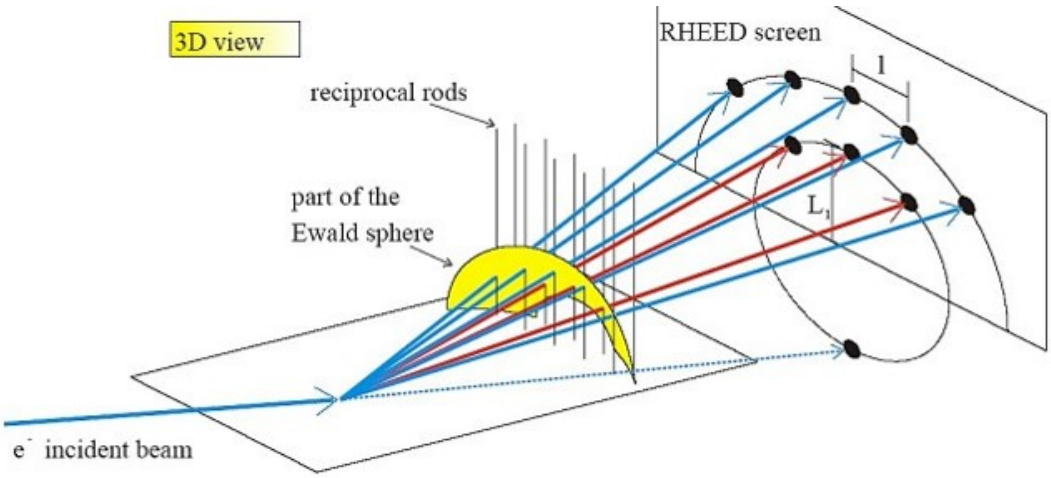

Fig. 3.8. Schematic drawing of RHEED pattern from the intersection between Ewald sphere and reciprocal lattice rods [28].

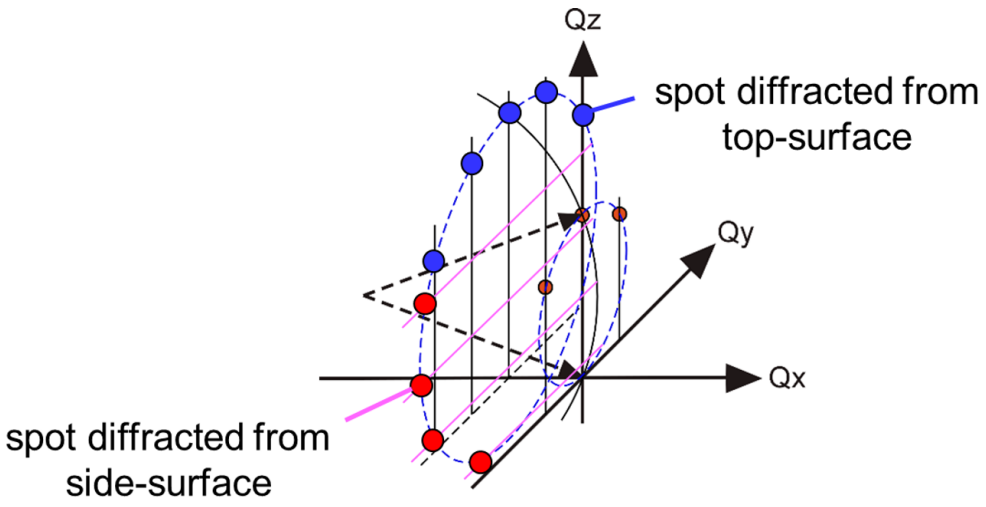

Fig. 3.9. Relationship between reciprocal lattice rods and Ewald's sphere diffracted from top- and side-surfaces.

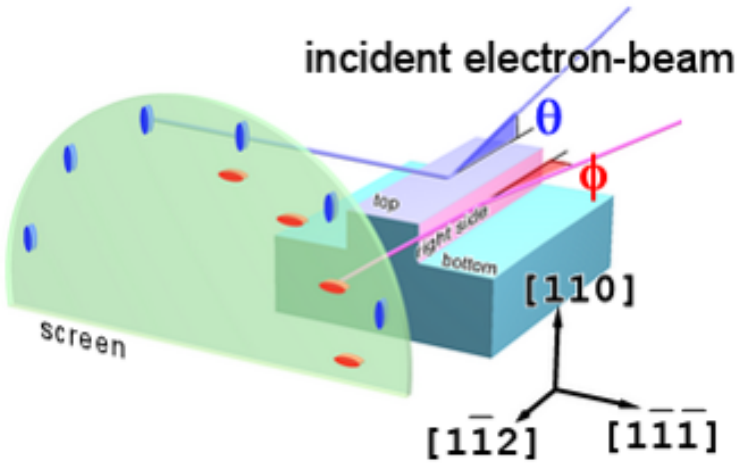

Fig. 3.10. Schematic diagram of simultaneous RHEED observation of top- and side-surfaces.

3.2.2 3D nano-fabricated sample

I prepared for two types of 3D nano-fabricated Si samples. In this paper, the detail of fabrication of 3D Si fabricated samples is not described because it was already reported in these papers [21, 29]. First type of 3D Si sample consists of top (110) surface and vertical {111} side-samples, as shown in Fig. 3.11 [21]. This sample is prepared for measuring atomically-flat side-surfaces. Second types of 3D Si sample consists of top (110) surface and facet {111} side-surface. The fabrication of 3D {111} facet samples, as shown in Fig. 3.12(a), were described simply as follows. These samples produced by dry-etching and wet-etching procedures. Fig. 3.12(b) shows a typical SEM image after 60 min-RIE. It has been reported that anisotropic wet-etching of Si(100) substrate leads to either vertical {100} side-surfaces, sloping {110} facet-surfaces, or sloping {111} facet-surfaces selected by a suitable etching solution, mask orientation and pattern [30–32]. Our subsequent wet-etching enlarged the {111} facet-surface region, as reported for the {111} side-surface region [21]. We should note that the atomically-ordered facet surfaces, as described latter, were produced under the restricted dry-etching and wet-etching conditions. Subsequently, the samples were dipped in a sulfuric peroxide mixture solution for 10 min, and dipped in HF for 1 min for the removal of surface impurities and the formation of a hydrogen termination [33–36]. After each wet-process, the samples were rinsed with pure water.

As shown in Figs. 3.12(c) and 3.12(d), the {111} facet sample produced under optimized conditions consists of (110) bottom-, (111) facet-, and $(11\bar{1})$ facet-surfaces, and two-type boundaries, namely top and bottom facet-edges. The top facet-edge is an edge-line boundary between (111) and $(11\bar{1})$ surfaces, and the bottom-facet edge is a line boundary between {111}

and (110) surfaces. Mostly straight top and bottom facet-edges and uniform (110), (111), and $(11\bar{1})$ surfaces can been seen. The {111} and (110) plane-widths projected to $[00\bar{1}]$ direction were 3.5 µm and 3.7 µm, respectively. These areas can be tuned by designing the initial mask pattern within the permissible range of Wulff's theorem [37].

In the experiment, several {111} facet samples were prepared. A sample was used for RHEED observations to confirm clean and atomically-ordered surfaces. The sample was introduced into a UHV chamber with a base pressure of less than 1×10^{-8} Pa, then was degassed and flashed by direct-current heating at 1523 K below 2×10^{-8} Pa. RHEED patterns after the flashing were observed at RT using an electron beam at 15 keV in energy with ∼0.5 mm in beam diameter, changing the incident direction of the glancing angle θ_g from the (110) bottom surface and the azimuthal angle ϕ from the in-plane $[1\bar{1}0]$ direction. The RHEED patterns were filtered by an image software to emphasize the spot features against the background.

Other samples were used as substrates for the production of Au interconnected wires. Hydrogenation of Si(111) and Si(110) planar-surfaces by HF wet-chemical cleaning processes yields high-quality non-reconstructed 1×1 surfaces without flashing in UHV [35, 36]. The hydrogen-terminated {111} facet sample was prepared by the HF wet-cleaning process, and subsequently 10 nm-thick Au was deposited by electron beam evaporation using a photoresist mask at RT. The Au thickness was monitored by a thickness monitor and measured by an atomic force microscope. Au wire-patterns with 2–50 µm in width and 100 µm in length were drawn in both parallel and perpendicular configurations; that is, the patterned long-lines were along-to and cross-over the facet edges, respectively3.13. Fig. 3.14 shows typical cross-sectional and top-view SEM images, respectively, for a 10-nm-Au deposited facet sample.

The Au film was homogeneously formed on the facet sample with a clear heterointerface. No significant defects were observed at the facet edges. Two-probe electrical measurements were performed at 100 K.

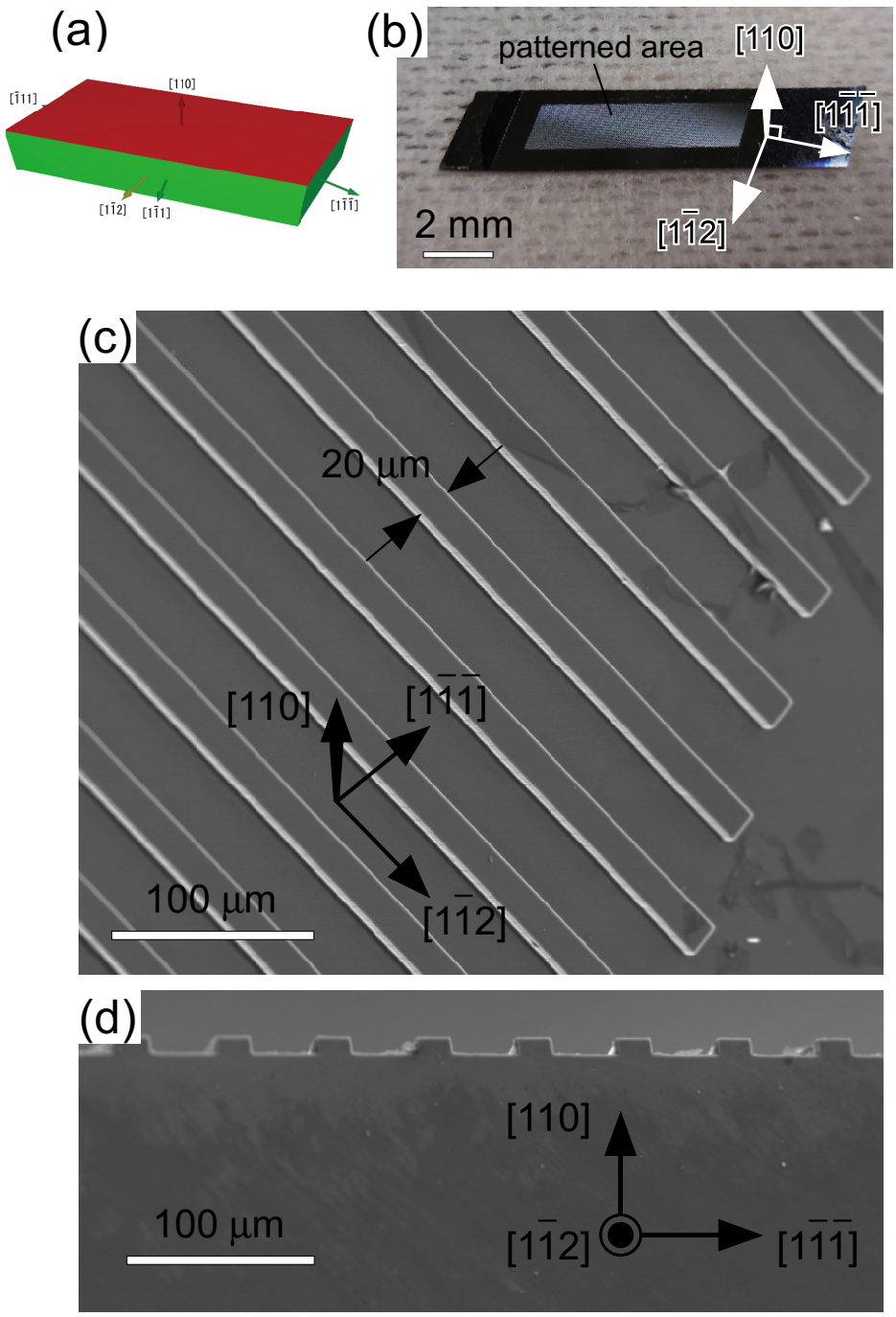

Fig. 3.11. (a) Crystal shape of Si. The 3D Si sample was designed to consist of a top (110) surface and vertical {111} side-surfaces. (b) Photograph of a 3D-patterned Si(110) substrate. (c) Bird's-eye-view and (d) cross-sectional SEM images of a patterned area of the 3D Si. [21]

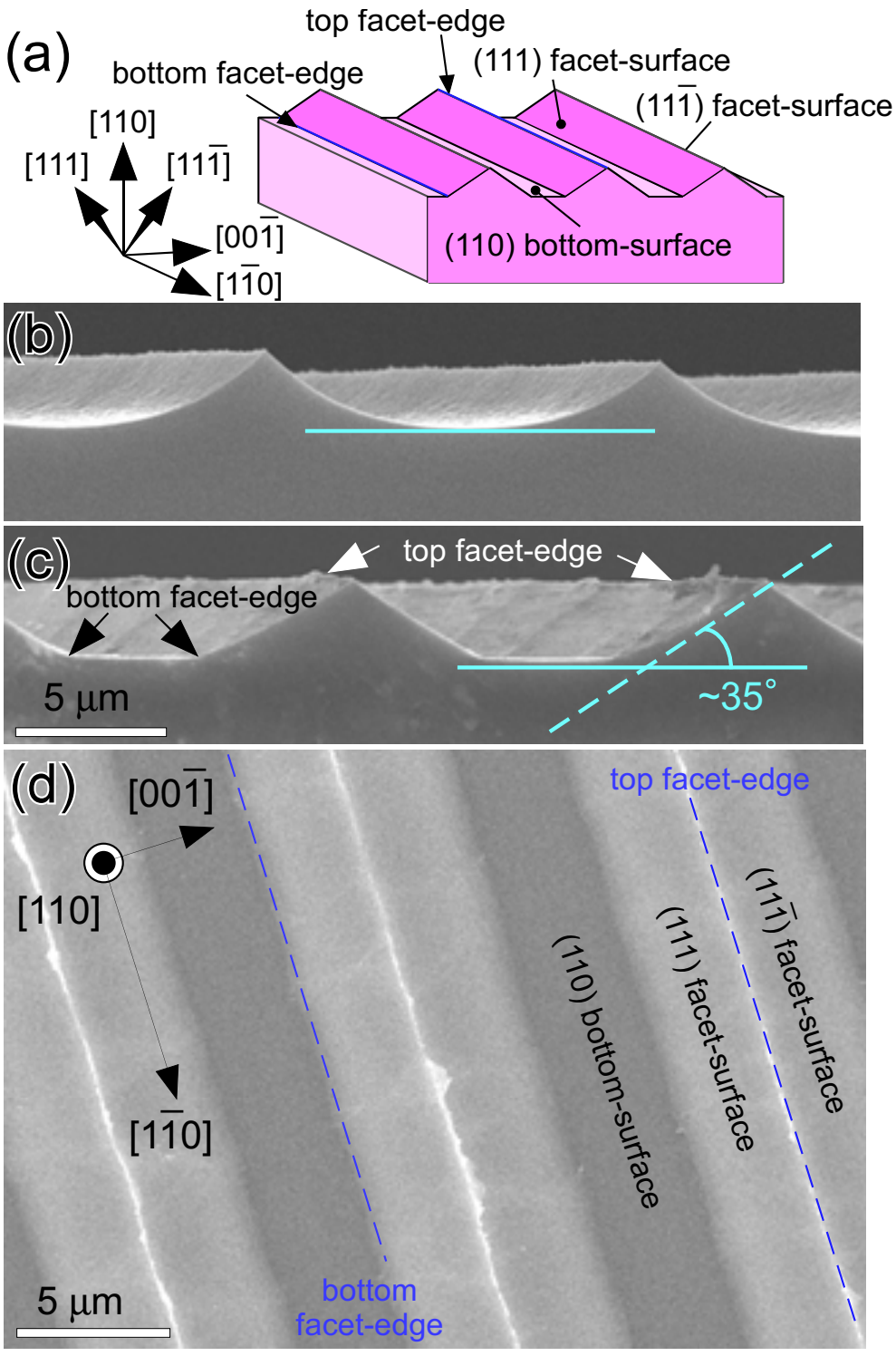

Fig. 3.12. (a) A schematic of a {111} faceted sample: {111} facet-surfaces and (110) bottom-surfaces with top and bottom facet-edges on a Si(110) substrate. (b) and (c) Typical cross-sectional SEM images after the dry etching, and followed by the wet etching, respectively, for a {111} facet sample. (d) A top-view SEM image of the sample in (c). Terrace width of {111} facets was about 4.3 μm. The (111) and (11$\bar{1}$) planes were $\sim 35°$ tilted from the (110) plane surface.

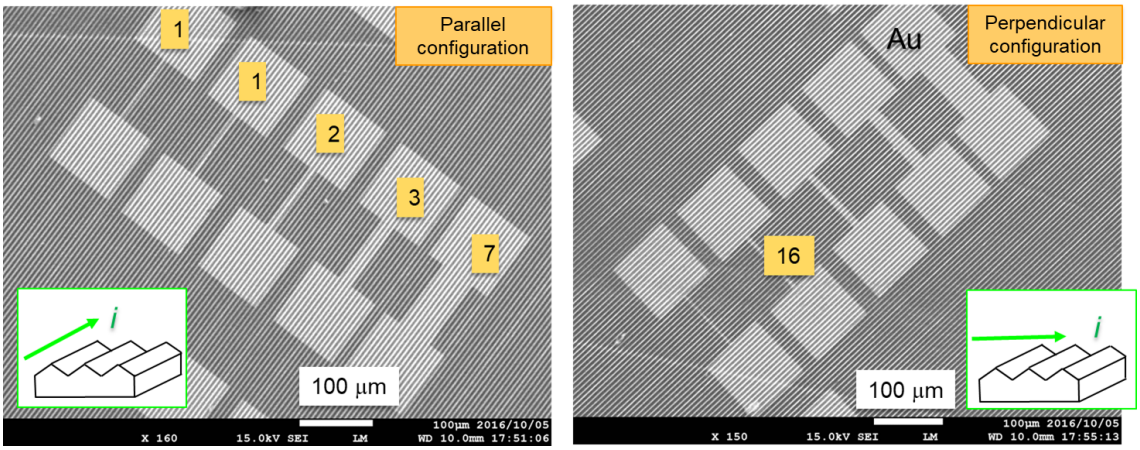

Fig. 3.13. Typical sample images of 10-nm-Au deposited facet samples. Wiring sizes are 2, 5, 10, 20 and $50\times100\,\mu m^2$. The inset number shows the number of the facet edges in wiring region.

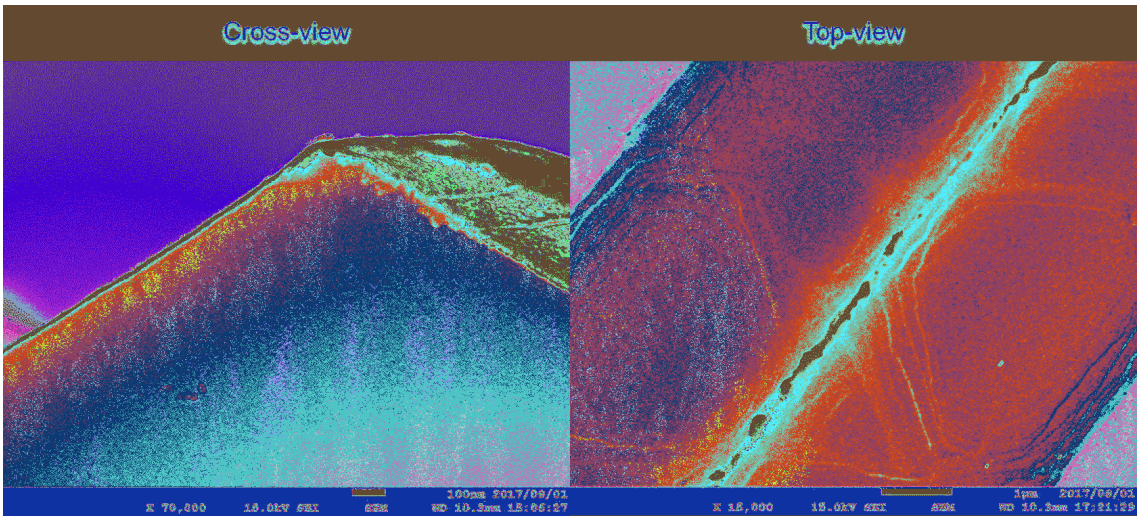

Fig. 3.14. Typical cross-sectional and top-view SEM images, respectively, for a 10-nm-Au deposited facet sample. The Au film was homogeneously formed on the facet sample with a clear heterointerface. No significant defects were observed at the facet edges. [29]

3.3 Results and discussion

3.3.1 RHEED observation of Si{111} vertical side-surface on Si(110) sample

This results was reported in this paper [21]. Fig. 3.11(a) and (b) shows a schematic image and picture of the sample, respectively. Fig. 3.11(c) and (d) indicate Bird ' s-eye-view and cross-sectional SEM images of a patterned area of the 3D Si, respectively. RHEED patterns from the 3D-patterned Si substrate observed at (a) $\theta = +0.3\,^\circ$ and $\phi = -1.6\,^\circ$, (b) $\theta = +0.3\,^\circ$ and $\phi = +1.1\,^\circ$, and (c) and $\theta = 0.0\,^\circ$ and $\phi = +1.9\,^\circ$ are shown in Fig 3.15. The diffraction pattern from side surface changes along changing of ϕ. It is important that the changing of ϕ for side-surface corresponds to changing θ for surface of substrate, that is, the glancing angle. Fig. 3.16(a) and (b) shows the reciprocal lattice rods of Si(110) and Si($1\overline{1}\overline{1}$) plane. The relationship of lattice plane and 3D structure is described in Fig. 3.16(c). Fig. 3.17(a) shows a typical RHEED pattern for 3D-patterned Si substrate observed at $\theta_g = 1.1^\circ$ and $\phi = 0.2^\circ$. A simulated RHEED pattern from ($1\bar{1}\bar{1}$) side-surface and (110) top-surface reflecting their geometric relationship is shown in Fig. 3.17(b). The pattern consists of a sharp ($1\bar{1}\bar{1}$)7×7 pattern tilted at 90° in clockwise direction (marked by pink circles) and a (110)16×2 pattern (marked by blue circles) The simulation of RHEED pattern corresponds to experimental result, which indicate that the RHEED pattern of super-reconstructions from side surface can be confirmed. this is the first report of the RHEED patterns of super-reconstructions from such well-defined side-surfaces.

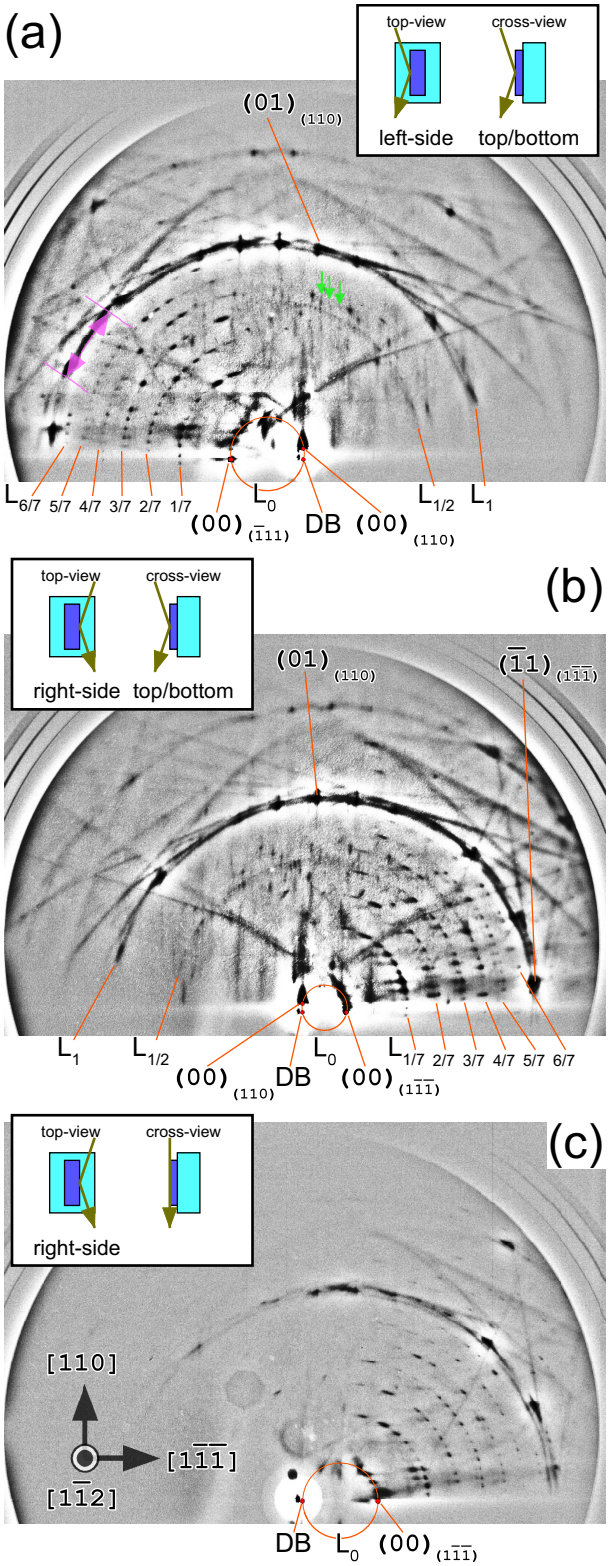

Fig. 3.15. RHEED patterns from the 3D-patterned Si substrate observed at (a) $\theta = +0.3^\circ$ and $\phi = -1.6^\circ$, (b) $\theta = +0.3^\circ$ and $\phi = +1.1^\circ$, and (c) and $\theta = 0.0^\circ$ and $\phi = +1.9^\circ$. The intensity of the direct beam (DB) was reduced by a beam stopper. The insets schematically show the relationship between the incident electron beam and the 3D-Si, indicating the observable surfaces. [21]

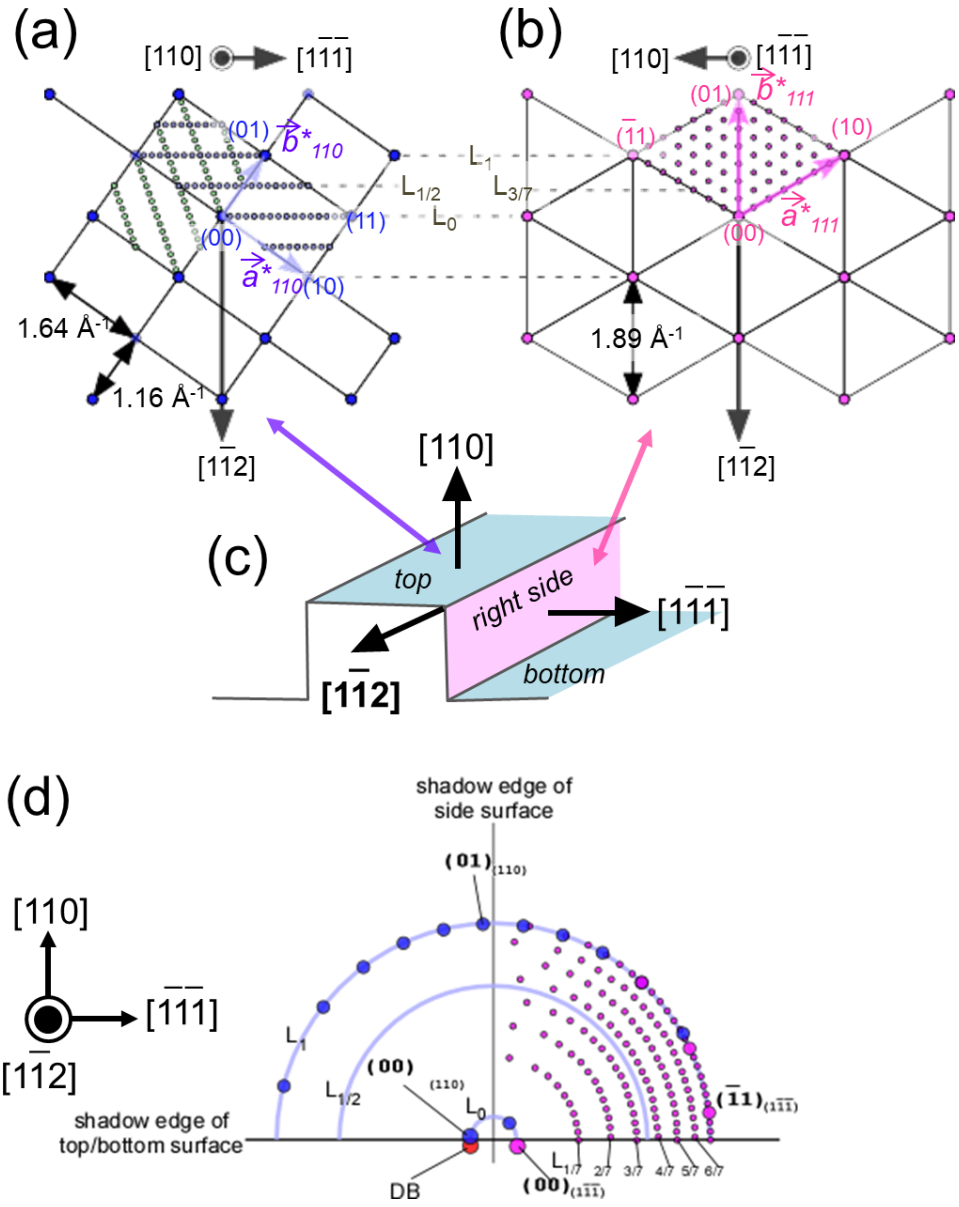

Fig. 3.16. Schematics of the 2D reciprocal lattices on (a) Si(110)2×16 and (b) Si(1$\bar{1}\bar{1}$)7×7 and$\sqrt{3}\times\sqrt{3}$, corresponding to the top/bottom and right-side surfaces, respectively on (c) the 3Dpatterned Si. (d) Simulated RHEED pattern from the (110) top/bottom and (1$\bar{1}\bar{1}$) right-side surfaces at $\theta = +0.3\,^\circ$ and $\phi = +1.1\,^\circ$. The diffraction spots from Si(110)2×16 domain A and Si(1$\bar{1}\bar{1}$) 7×7 are represented in purple and pink, respectively. The reciprocal-lattice unit-length is defined as 2π divided by a real-lattice unit length here. [21]

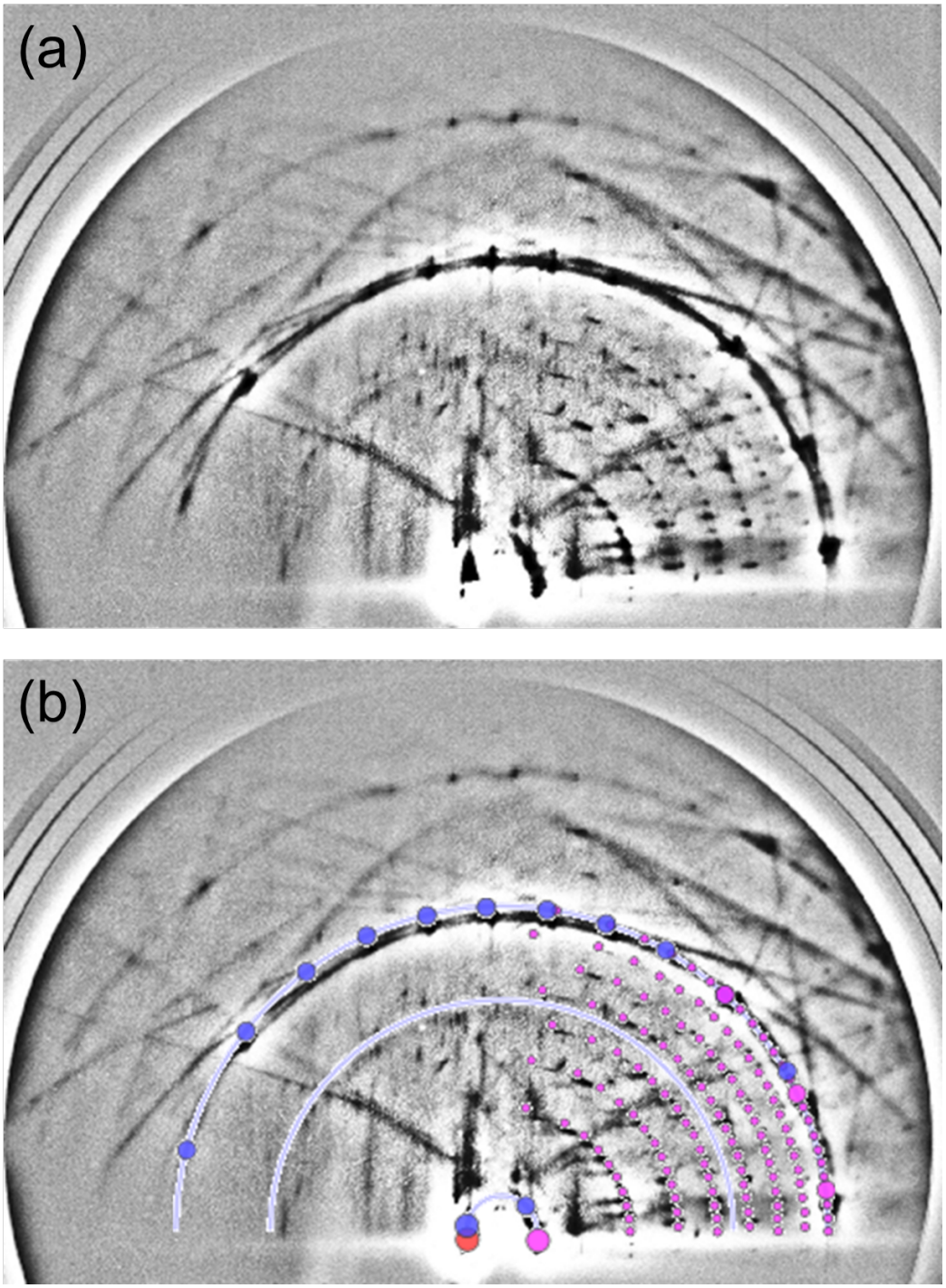

Fig. 3.17. (a) A typical RHEED pattern for 3D-patterned Si substrate observed at $\theta_g = 1.1°$ and $\phi = 0.2°$. (b) A simulated RHEED pattern from $(1\bar{1}\bar{1})$ side-surface and (110) top-surface reflecting their geometric relationship. The pattern consists of a sharp $(1\bar{1}\bar{1})7\times7$ pattern tilted at 90° in clockwise direction (marked by pink circles) and a $(110)16\times2$ pattern (marked by blue circles) [21].

3.3.2 RHEED observation of Si{111} facet surface on Si(110) sample

Figure 3.18(a) shows a typical filtered-RHEED pattern obtained from the {111} facet sample at $\theta_g = 0.7°$ and $\phi = 2.7°$ after the flashing in UHV. The RHEED patterns showed notable characteristics, consisting of tilted 7×7 spots (some are marked by yellow circles, and the 1/7-order Laue-zones, $L_{1/7}$–$L_{6/7}$, are well recognized) and faint horizontal 16×2 spots (cyan circles). The 7×7 pattern was tilted in a counterclockwise direction around a direct beam (DB), and the tilt angle was $\sim 36°$, which is consistent with θ_F. Figure 3.18(b) shows a simulated RHEED pattern from the (111) facet-surface, corresponding to Ewald-sphere cross-sections of two-dimensional 7×7 reciprocal-lattice rods of the tilted Si(111). Excellent agreement between Figs. 3.18(a) and 3.18(b) indicates the creation of an atomically-ordered Si(111)7×7 facet surface. Based on the fabricated 3D structure, the relative glancing- and azimuth-angles to tilted Si(111) facet surface are 2.1° and 1.8°, respectively, in this condition. These RHEED patterns clearly show the existence of three different atomically-ordered surfaces on the {111} facet sample, that is, the (110) bottom, (111) facet, and $(11\bar{1})$ facet surfaces.

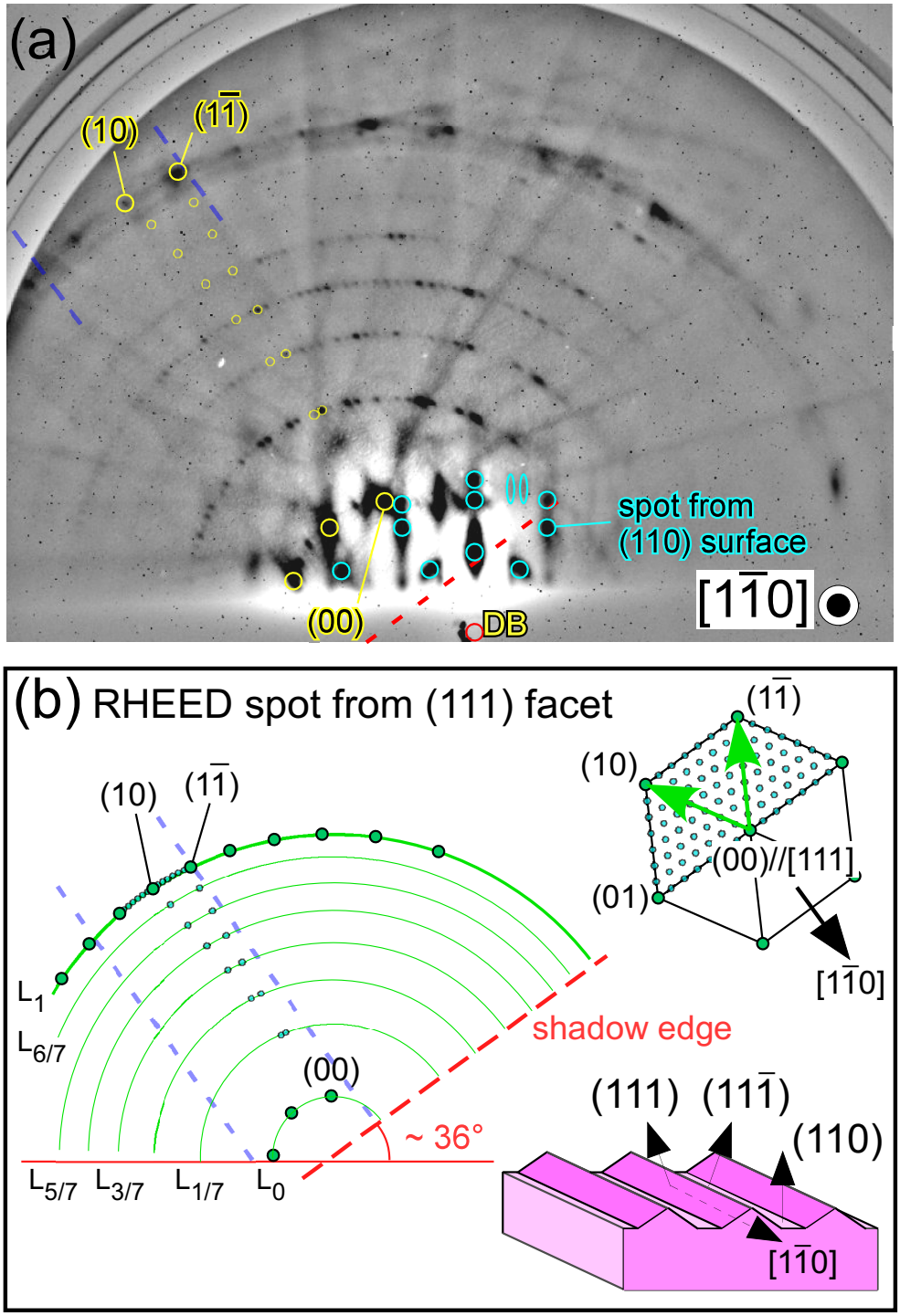

Fig. 3.18. (a) A typical RHEED pattern for the {111} facet sample observed at $\theta_g = 0.7°$ and $\phi = 2.7°$. The pattern consists of a sharp $(11\bar{1})7\times7$ pattern tilted at $\sim 36°$ in counter-clockwise direction (marked by yellow circles) and very faint $(110)16\times2$ pattern (marked by cyan circles). (b) A simulated RHEED pattern from (111) plane reflecting their geometric relationship. The upper inset represents the corresponding two-dimensional reciprocal lattice normal to the facet direction.

3.3.3 Electric transport properties of facet sample

The atomically-ordered surface on the {111} facet plane was confirmed by RHEED. To examine the geometric effect on the conductive property, 3D angularly-interconnected Au-wires were produced on the {111} facet sample as next step. Figures 3.14 show typical cross-sectional and top-view SEM images, respectively, for the 10 nm-Au deposited {111} facet sample. Both SEM images indicates that Au was uniformly grown on the Si facet surfaces with smooth interfaces without any depressions or protrusions. In top-view SEM image (Fig. 3.14), the continuous Au layer crossing-over top and bottom facet-edges is seen. Neither break nor discontinuity of the Au wires was observed in SEM images, even on the top facet-edges.

Figure 3.19 shows current-voltage properties at 100 K for the 3D angularly-interconnected Au-wires with 2 μm width (circles) and 5 μm width (squares) in the parallel (red) and perpendicular (blue) configurations (insets). Both perpendicular wires indicate about one-order larger resistance (smaller current) than the parallel wires in each width. For the other wire widths, the resistance in the perpendicular configuration was also larger than that in the parallel configuration. The simplified resistance ratio, defined as the inverse of current ratio at a fixed voltage, was 3–10 in the measured wire-widths, where slight nonlinearity in current-voltage due to Schottky barrier contacts [38, 39] was seen. We should note that the dimension (cross section and length) and crystallinity of the Au film were mostly the same in the parallel and perpendicular configurations. Thus, the significant anisotropic resistance in these configurations is ascribed to the property of the geometric shapes of the Au wires, that is, 3D angular-interconnects. Indeed, the perpendicular wire has more facet edges than

the parallel wires; the perpendicular channel crossed over 11 top facet-edges and 23 bottom facet-edges while the parallel channel included 1 top facet-edge and 2 bottom facet-edges in the 5 μm width.

To evaluate the electric path due to the structural geometry of the 3D facet sample, the configuration dependent resistance for the Au wire was estimated as following. On the 3D facet structure, Au wires can be separated into four regions: flat bottom-surface, flat facet-surface, convex top facet-edge, and concave bottom facet-edge regions with lengths of ℓ_B ($\simeq$ 3.7 μm), ℓ_F ($\simeq$ 4.3 μm), $2\ell_{TE}$ and ℓ_{BE}, respectively, as shown in Fig. 3(d). The effective film thickness, t, in each region depends on the tilt angle, θ, to the (110) plane as $t(\theta) = t_d \cos\theta$. Here, t_d is the deposition thickness ($\simeq$ 10 nm); that is, t is t_d at the bottom-surface and $t_d \cos\theta_F$ at the facet-surface regions. In the edge regions, $t(\theta)$ depends on the local curvature ($0 \leq \theta \leq \theta_F$). The resistance in parallel configuration, $R_\parallel$, can be described as a parallel resistance of each region.

$$\frac{1}{R_\parallel} = N_\parallel \cdot \frac{1}{\rho L} \cdot (\ell_B t_d + 2\ell_F t_d \cdot \cos\theta_F + 4\ell_E \langle t(\theta)\rangle) \tag{26}$$

Here, $N_\parallel = W/(\ell_B + 2\ell_F \cos\theta_F)$ is the number of top facet-edges in the channel width, W (= 2–50 μm). L is the channel length ($\simeq$ 100 μm). ρ is an electrical resistivity of Au. $\langle t(\theta)\rangle$ represents the average thickness at the edge regions, assuming equivalent bottom and top edges ($\ell_{TE} = \ell_{BE} = \ell_E$). Similarly, the resistance in perpendicular configuration, $R_\perp$, can be described as a series resistance of each regions.

$$R_\perp \simeq N_\perp \cdot \frac{\rho}{W} \cdot (\frac{\ell_B}{t_d} + \frac{2\ell_F}{t_d \cdot \cos\theta_F} + \frac{4\ell_E}{\langle t(\theta)\rangle}\alpha) \tag{27}$$

Here, $N_{\perp} \simeq L/(\ell_B + 2\ell_F \cos\theta_F)$ is the number of top facet-edges. α is an enhancement factor in resistivity when the electric current flows crossing the edges. The electron inelastic mean free paths in Au is 400 Å [41]. It is straight forward to consider that α has the contribution of the electron scattering across the 3D angular-interconnects of the Au wire (TE and BE regions in Fig. 3.20). The geometries of crystal grain boundaries in the polycrystalline Au wire may influence the electrical resistance enhancement [42]. The aggregation of crystal grain boundaries at the interconnect region, leading to the reduction of the effective cross-sectional area, could attribute to the high resistance.

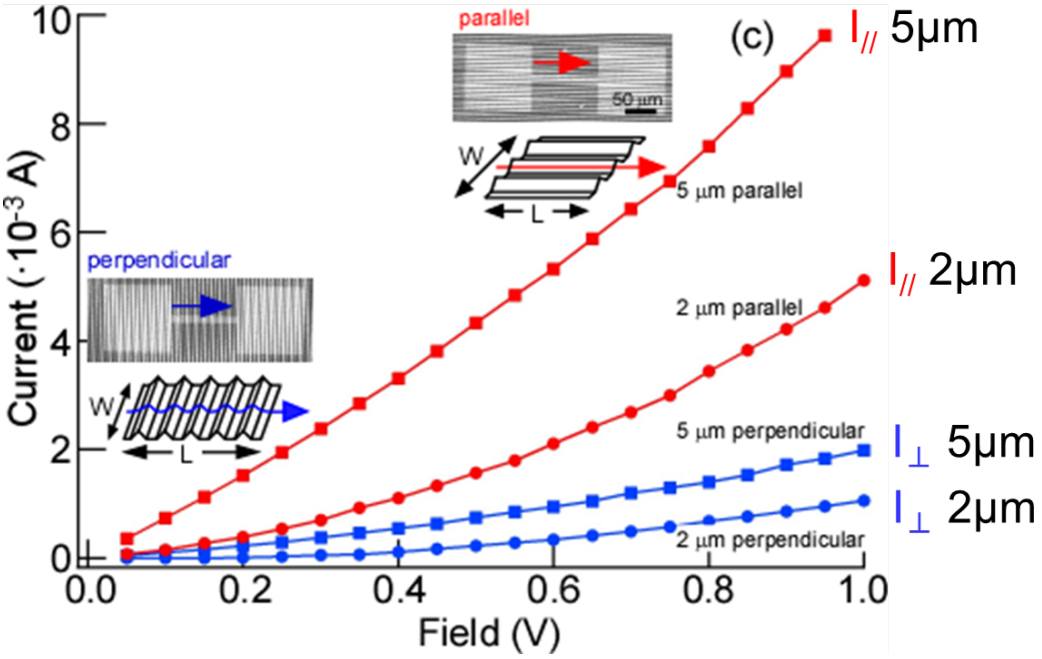

Fig. 3.19. Current vs voltage curves of Au wires with the channel area $W \times L$ values of 2×100 μm^2 (circles) and 5×100 μm^2 (squares) at 100 K in the parallel (red) and perpendicular (blue) configurations (insets). The inset current–voltage curves are in a semilog plot [29].

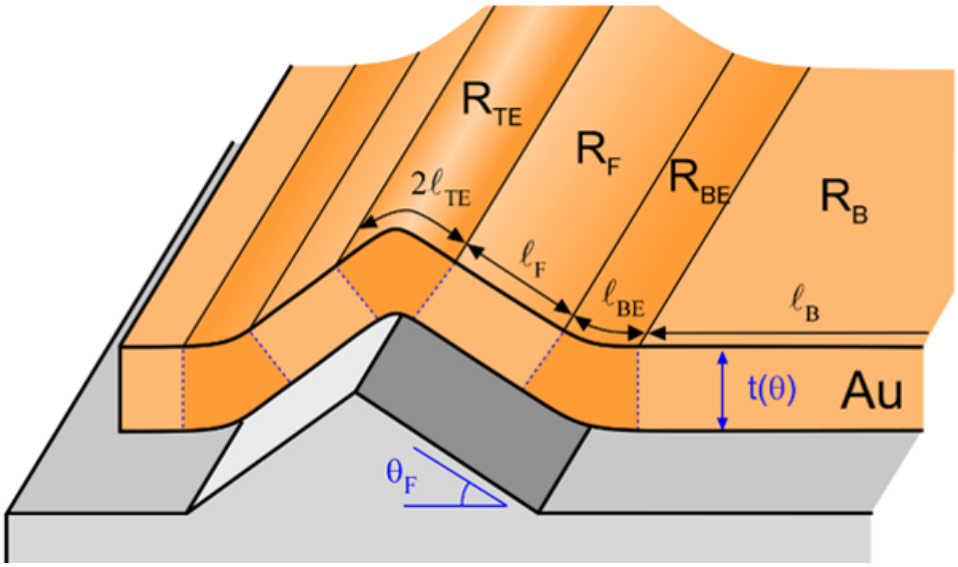

Fig. 3.20. Schematic illustration of the Au film on the Si{111} facet sample. The Au film is assumed to consist of bottom-surface (B), facet-surface (F), top facet-edge (TE), and bottom facet-edge (BE) regions. Symbols R and l represent resistance and length in each region, respectively. θ_F is the facet angle (35.3°). $t(\theta)$ is the effective thickness of the Au film depending on the local curvature angle [29].

3.4 Conclusion

RHEED observation of a various of three-dimensionally nano-fabricated materials prepared by Hattori were performed. The clearly diffraction patterns obtained from the Si{111} vertical side-surface on Si(110)and Si{100}, {110} and {111} vertical on Si(100) sample [22]. For the first time, the flatness of the atomically-ordered {111}7×7 facet surfaces on the 3D patterned Si(110) substrate was confirmed by RHEED. I found that the conductivity passing through the interconnects is sensitive to the alignment of the facet edges in electric path, and the perpendicular resistance of Au-wire to facet edges showed 3–10 times larger resistance than that the parallel resistance. This work pioneers to fundamental understanding and impact of the 3D angular-interconnects of the metal wire in electric transport. I believe that the progress in the comprehensive investigation for the intrinsic interconnect transport properties on 3D structures will subsequently produce critical benefits in the semiconductor industry. And RHEED will become standard method to evaluate the side- and facet-surface of 3D nano-fabricated materials. As future work, the allowance of roughness confirmed by RHEED observation will be considered. For example, how will change the roughness and RHEED pattern when 3D Si sample is not flashed. Then the resistance change of metal wiring should be studied.

References

[1] D. Hisamoto, W.-C. Lee, J. Kedzierski, H. Takeuchi, K. Asano, C. Kuo, E. Anderson, T.-J. King, J. Bokor, and C. Hu, IEEE Trans. Electron Devices **47**, 2320 (2000).

[2] J.-P. Colinge, Solid-State Electron. **48**, 897 (2004).

[3] C. Auth, C. Allen, A. Blattner, D. Bergstrom, M. Brazier, M. Bost, M. Buehler, V. Chikarmane, T. Ghani, T. Glassman, R. Grover, W. Han, D. Hanken, M. Hattendorf, P. Hentges, R. Heussner, J. Hicks, D. Ingerly, P. Jain, S. Jaloviar, R. James, D. Jones, J. Jopling, S. Joshi, C. Kenyon, H. Liu, R. McFadden, B. Mcintyre, J. Neirynck, C. Parker, L. Pipes, I. Post, S. Pradhan, M. Prince, S. Ramey, T. Reynolds, J. Roesler, J. Sandford, J. Seiple, P. Smith, C. Thomas, D. Towner, T. Troeger, C. Weber, P. Yashar, K. Zawadzki, and K. Mistry, VLSI Symp. Tech Dig., 2012, p. 131.

[4] B. Feldman, R. Deng, and S. T. Dunham, J. Appl. Phys. **103**, 113715 (2008).

[5] E. Buitrago, M. F.-Bolaños, S. Rigante, C. F. Zilch, N. S. Schröter, A. M. Nightingale, and A. M. Ionescu, Sens. Actuators B **193**, 400 (2014).

[6] N. A. Lanzillo, O. D. Restrepo, P. S. Bhosale, E. C. Silva, C.-C. Yang, B. Y. Kim, T. Spooner, T. Standaert, C. Child, G. Bonilla, and K. V. R. M. Murali, Appl. Phys. Lett. **112**, 163107 (2018).

[7] K. C. Elsom and J. R. Sambles, J. Phys. F **11**, 647 (1981).

[8] E. Z. Luo, S. Heun, M. Kennedy, J. Wollschläger, and M. Henzler, Phys. Rev. B **49**, 4858 (1994).

[9] E. T. Krastev, L. D. Voice, and R. G. Tobin, J. Appl. Phys. **79**, 6865 (1996).

[10] J. S. Chawla, F. Gstrein, K. P. O'Brien, J. S. Clarke, and D. Gall, Phys. Rev. B **84**, 235423 (2011).

[11] K. Mao, T. Saraya, and T. Hiramoto, Jpn. J. Appl. Phys. **52**, 04CC11 (2013).

[12] S. C. Lee, A. Neumann, Y.-B. Jiang, K. Artyushkova, and S. R. J. Brueck, Nanotechnology **27**, 375707 (2016).

[13] S. M. Goodnick, D. K. Ferry, X. W. Wilmsen, Z. Liliental, D. Fathy, and O. L. Krivanek, Phys. Rev. B **32**, 8171 (1985).

[14] C.-Y. Mou and T.-M. Hong, Phys. Rev. B **61**, 12612 (2000).

[15] J. Wang, E. Polizzi, A. Ghosh, S. Datta, and M. Lundstrom, Appl. Phys. Lett. **87**, 043101 (2005).

[16] C. Buran, M. G. Pala, M. Bescond, M. Dubois, and M. Mouis, IEEE Trans. Electron Devices **56**, 2186 (2009).

[17] S. G. Kim, M. Luisier, A. Paul, T. B. Boykin, and G. Klimeck, IEEE Trans. Electron Devices **58**, 1371 (2011).

[18] H.-E. Jung and M. Shin, IEEE Trans. Electron Devices **60**, 1861 (2013).

[19] S. L. Tripathi and R. A. Mishra, J. Electron Devices **86**, 1537 (2013).

[20] H. Ryu, Nanoscale Res. Lett. **11**, 36 (2016).

[21] A. N. Hattori, K. Hattori, S. Takemoto, H. Daimon, and H. Tanaka, Surf. Sci. **644**, 86 (2016).

[22] A. N. Hattori, S. Takemoto, K. Hattori, H. Daimon, and H. Tanaka, Appl. Phys. Express **9**, 085501 (2016).

[23] H. Yang, A. N. Hattori, A. Ohata, S. Takemoto, K. Hattori, H. Daimon, and H. Tanaka, Jpn. J. Appl. Phys. **56**, 111301 (2017).

[24] M. Bhole, A. Kurude, and S. Pawar International Journal of Engineering **2**, 2670 (2013).

[25] M. Bohr, Intel Development Forum, (2014) intel.com.tw.

[26] T. Yamaguchi, K. Yamazaki, M. Nagase, and H. Namatsu, Jpn. J. Appl. Phys. **42**, 3755 (2003).

[27] A. Ichimiya and O. I. Cohen (2004) Reflection high energy electron diffraction, Cambridge university press.

[28] J. Klein, PhD Thesis, University of Cologne (2001).

[29] S. Takemoto, A.N. Hattori, K. Hattori, H. Tanaka, and H. Daimon, Jpn. J. Appl. Phys. (2018) in press.

[30] D. L. Kendall, Annu. Rev. Mater. Sci. **9**, 373 (1979).

[31] O. Powell and H. B. Harrison, J. Micromech. Microeng. **11**, 217 (2001).

[32] A. Brockmeier, F. J. S. Rodriguez, and M Harrison, J. Micromech. Microeng. **22**, 125012 (2012).

[33] T. Takahagi, I. Nagai, A. Ishitani, and H. Kuroda, J. Appl. Phys. **64**, 3516 (1988).

[34] S. Watanabe, N. Nakayama, and T. Ito, Appl. Phys. Lett. **59**, 1458 (1991).

[35] K. Kaji, S. -L. Yau, and K. Itaya, J. Appl. Phys. **78**, 5727 (1995).

[36] S. Y. Matsushita, E. Kawamoto, K. Haga, T. Yamada, and S. Suto, Surf. Sci. **632**, 135 (2015).

[37] G. Wulff, Z. Kristallogr. **34**, 449 (1909) [in German].

[38] D. Hyman and M. Mehregany, IEEE Trans. Compon. Packag. Technol. **22**, 357 (1998).

[39] S. Zaima and Y. Yasuda, Oyo Buturi **63**, 1093 (1994) [in Japanese].

[40] S. Tanuma, C.J. Powell, and D.R. Penn, Surf. Int. An. **11**, 577 (1988).

[41] N. W. Ashcroft and N. D. Mermin (1976) Solid State Physics, Saunders College, Philadelphia, 116, 217.

[42] H.-Y. Lee, S.-M. Yi, J.-H. Lee, H.-S. Lee, S. Hyun, and Y.-C. Joo, Met. Mater. Int. **16**, 947 (2010).

Chapter 4. Conclusion remark

The purpose is development of a new analysis method in 2D RSM and evaluation of surface arrangement in 3D nano-fabricated materials using diffraction. I indicate how to improve diffraction method in the fundamental and applied part. The development of the analysis method corresponds to fundamental approach to estimate in-plane strain from the spot shape broadening. I applied the general method which was reported to estimate strain and domain size so far. The new method can be evaluated from the comparison with the result of applying general methods. As practical approach of diffraction method, I perfomed observe RHEED of 3D nano-fabricated materials. The results obtained in the present study are summarized in following.

The estimation in-plane strain for β-$FeSi_2$(100) nano-film by applying various of general analysis method, which is W-H method, 1D Gaussian fitting and 2D Gaussian fitting was performed. I found that W-H method is a little accuracy to estimate strain because of the less number of reflections. In Gaussian fitting methods a certain region of strain and domain size were estimated. The spot shapes calculated from estimated strain and domain size in Gaussian fitting were not reproduced as oval shape of experiment due to the assumption of isotropic strain and domain size. In a new analysis method, the fitting by the superposition of differently-strained reflection profiles using a probe beam with reduced coherent lengths when coherent region is smaller than homogenous domain size can be obtained the narrow distribution of strain than W-H method and anisotropic strain of highest weight. The strain distribution of β-$FeSi_2$(100) nano-film was estimated using a new analysis method with quite smaller residual sum of squares. This paper is the firstly analysis to estimate the strain

distribution calculated from the spot shape of 2D-RSM in XRD measurement.

To evaluate surface atomic arrangement in 3D nano-fabricated materials, RHEED observation of a various of 3D Si sample was performed. The clearly diffraction patterns obtained from the Si{111} vertical side-surface on Si(110) sample. For the first time, the flatness of the atomically-ordered {111}7×7 facet surfaces on the 3D patterned Si(110) substrate was confirmed by RHEED. I also found that the conductivity passing through the interconnects is sensitive to the alignment of the facet edges in electric path, and the perpendicular resistance of Au-wire to facet edges showed 3–10 times larger resistance than that the parallel resistance. This work pioneers to fundamental understanding and impact of the 3D angular-interconnects of the metal wire in electric transport.

Acknowledgements

I would like to express the deepest appreciation to Prof. Hiroshi Daimon for his support and encouragement in my five years study life. I also want to thank Prof. Yukiharu Uraoka and Assoc. Prof. Nobuyoshi Hosoito for the advise and discussion of research from the different point of view as the supervisor. I deeply appreciate Assoc. Prof. Ken Hattori for his advice, continuous encouragement and support in every respect. He taught me the research methods which are analysis methods of experimental data and using method of equipments directly. His guidance helps me a lot in my study life. I also thank Prof. Hidekazu Tanaka and Asst. Prof. Azusa N. Hattori of the Institute of Scientific and Industrial Research, Osaka Univ for the collaborating in the experiment. I would like to thank all the members in Surface and Materials Science Laboratory. I bring my gratitude to Asst. Prof. Sakura N. Takeda, Specially Appointed Asst. Prof. Hiroyuki Matsuda and Munetaka Taguchi for the help in my research. I want to special thank Dr. Nozomu Hirota for his advise of research life and thank seniors and juniors. Finally, My deepest appreciation goes to my parents for help, understanding and encouragement in my study and life